UNIVERSITY OF OKLAHOMA

GRADUATE COLLEGE

TOWARDS PRACTICAL APPLICATIONS OF TWO MODE SQUEEZED STATES

A DISSERTATION

SUBMITTED TO THE GRADUATE FACULTY

in partial fulfillment of the requirements for the

Degree of

DOCTOR OF PHILOSOPHY

By

UMANG JAIN
Norman, Oklahoma
2026

Downloaded from SHAREOK. Persistent Handle URL: https://hdl.handle.net/11244/342527

TOWARDS PRACTICAL APPLICATIONS OF TWO MODE SQUEEZED STATES

A DISSERTATION APPROVED FOR THE
HOMER L. DODGE DEPARTMENT OF PHYSICS AND ASTRONOMY

BY THE COMMITTEE CONSISTING OF

Dr. Alberto Marino Valle, Chair

Dr. Arne Schwettmann

Dr. Grant Biedermann

Dr. Michael Santos

Dr. Hjalti Sigmarsson

Chapter 5 © Copyright The Optical Society, 2025
Used by permission
All other content:
© Copyright UMANG JAIN 2026
All Rights Reserved.

Acknowledgements

I would first like to express my deepest gratitude to my advisor, Dr. Alberto M. Marino, for his guidance, support, and encouragement throughout my Ph.D. His mentorship has profoundly shaped the way I approach research and problem-solving. I am especially grateful for the intellectual freedom he gave me to explore new ideas and directions, while always providing the insight, perspective, and rigor needed to bring projects to completion. His constant enthusiasm for science and commitment to high standards have been a lasting source of inspiration.

I would also like to thank the members of my dissertation committee: Dr. Arne Schwettmann, Dr. Grant Biedermann, Dr. Mike Santos, and Dr. Hjalti Sigmarsson, for their valuable time, thoughtful feedback, and constructive discussions. Their diverse perspectives and careful reviews have significantly strengthened this work.

I am deeply indebted to my colleagues in the Quantum Optics group, past and present, for their collaboration, friendship, and many stimulating discussions. In particular, I wish to acknowledge Mohammadjavad Dowran, Saesun Kim, Gaurav Nirala, and Tim Woodworth for their help with experiments, coding, and for generously sharing their experience, which made my own research journey much smoother. I am also grateful to Kit and Daida for the many insightful discussions we shared—not only about research, but also across several courses, especially during the early stages of my Ph.D., when those conversations were particularly formative.

I would like to thank Chad, Alex, and Barry for their invaluable guidance in

electronics, instrumentation, and hardware development. Their willingness to teach and help with the design and fabrication of custom experimental hardware played an essential role in the successful execution of this research. I am also thankful to all my instructors at the University of Oklahoma for the rigorous training and foundational lessons that shaped me as both a student and a researcher, as well as to the broader department for fostering a supportive and intellectually stimulating environment.

This work would not have been possible without financial support. I gratefully acknowledge the National Aeronautics and Space Administration (Grant No. 80NSSC21C0359) and the U.S. Department of Energy under Contract No. DE-AC05-00OR22725 for supporting this research.

Finally, I would like to thank my family for their unconditional love, patience, and encouragement throughout my academic journey. My parents have always been a constant source of strength and motivation. Above all, I am profoundly grateful to my wife, Mayuri, for her unwavering support, understanding, and love. Her presence has been my greatest source of encouragement and motivation during this long and challenging process.

Table of Contents

List of Figures **xiii**

Abstract **xiv**

Publications and Conference Presentations **xvii**

List of Acronyms **xix**

1 Introduction **1**
1.1 Quantum Revolution 2
1.2 Second Quantum Revolution and Quantum Sensing 4
1.3 Thesis Outline 6

2 Quantum Light: Squeezed States of Light **9**
2.1 Quantum Mechanical Description of Light 10
2.2 Coherent States of Light 13
2.3 Single-Mode Squeezed States 15
2.4 Two-Mode Squeezed States 17
2.5 Nonlinear Processes to Generate Quantum States of Light 20

3 Twin-Beam Generation via Four-Wave Mixing in Hot Rubidium Vapor **25**
3.1 Generation of Twin Beams 25
3.2 Noise Measurements 28
3.3 Effect of losses on squeezing 31
3.4 Shot-Noise Limit Calibration 34
3.5 Spatial and Momentum Correlations in Twin Beams 36
3.5.1 Near-Field and Far-Field Correlations 38
3.5.2 Multi-Spatial-Mode Properties of Twin Beams 40

4 Quantum Sensing with Squeezed States of Light **42**
4.1 Measurement Sensitivity 44
4.2 Quantum-Enhanced Sensing using Twin Beams 46
4.3 Quantum Fisher Information and Fundamental Sensitivity Limits 48

5 Compact Fiber-Coupled Twin-Beam Source **51**
5.1 Introduction and Motivation 51
5.2 Design Goals and Low-SWaP Considerations 53
5.3 Fiber Coupled Squeezing Optimization 56
5.4 Experimental Setup 60
5.5 Results and Conclusions 63

6 Quantum-Enhanced Fiber Sensing **67**
6.1 Introduction and Motivation 67
6.2 FBG Working Principle 70
6.3 FBG Characterization 73

6.4 Experimental Scheme and Detection 78
6.5 Signal Analysis and Data Processing 85
6.5.1 Part I: Single-Frequency Measurements with Squeezed Light 86
6.5.2 Part II: Broadband Analysis with FFT Processing 92

7 Quantum-Enhanced Plasmonic Sensing **104**
7.1 Introduction and Motivation 104
7.2 Plasmonic Sensors and Sensitivity Calculation 105
7.3 QFI for Plasmonic Sensors 112
7.4 Modelling Nanohole Structures 115
7.5 Experimental Implementation 120
7.5.1 Characterization of the Sensor with Broad Band White Light 121
7.5.2 Experimental Setup 124
7.6 Results and Discussion 129

8 Conclusions and Future Work **139**
8.1 Summary 139
8.2 Broader Implications 141
8.3 Future Directions 141

References **144**

List of Figures

2.1 Phase-space representation of an electric field: The electric field (left) can be described in phase-space representation (right) by its in and out of phase components $\hat{X}$ and $\hat{Y}$ that are equivalent to the real and imaginary parts of the complex electric field respectively. 12
2.2 Phase-space distribution and corresponding electric field behavior for (a) a coherent state, (b) an amplitude-squeezed state, (c) and a phase-squeezed state. 16

3.1 (a) FWM in a double-Λ configuration in Rb atoms: two pump photons (at frequency $\omega_{\rm p}$) and one seed photon at the probe frequency (ω_{pr}) result in pair photon emission at the probe and the conjugate (ω_c) frequencies. The frequency of the probe photons is red-detuned from the pump by $\sim$ 3 GHz, which is the energy separation between the two hyperfine structure (F=2 and F=3) ground states of the 5 $^2S_{1/2}$ energy level. (b) Simplified experimental setup for the FWM process. Orthogonally polarized probe and pump interact at the center of a Rb vapor cell and as a result a conjugate beam is generated. Intensities of probe and conjugate are measured with photodetectors and the difference photocurrent between the generated photocurrents is sent to a spectrum analyser to measure the intensity difference noise. 27
3.2 Intensity-difference squeezing spectrum: Normalized noise trace for the intensity difference from twin beams for a cell temperature of 99 °C, pump beam with 135 mW of power (0.6 mm diameter) interacting at an angle of 0.4° with the probe beam (0.6 mm diameter). Red trace represents the normalized squeezing and the blue trace represents the shot noise. A maximum of 7.2 dB of squeezing is observed for the 500 kHz to 1MHz frequency region. 32
3.3 Sample data for calibrating the SNL: A linear behavior of the noise power vs. total optical power indicates that the measurement is shot-noise limited. . . . 35
3.4 Phase-matching condition in FWM setup in a dispersive medium. Probe wave-vector (red) is at an angle to the pump wave-vector (maroon). Conjugate wave-vector is represented by yellow arrow. 37
3.5 Distribution of correlated regions in (a) far field and (b) near field. The circled region on the left side (probe beam cross section) is correlated with the circled region on the right side (conjugate beam cross section). 39

4.1 Components of a quantum enhanced sensing configuration: a source of quantum states, a sensing device, and a detection system. Enhancement in detection is possible when sensing device and detection scheme are already operating at their ultimate classical limit. 43

5.1 Schematic of compact experimental setup for generating fiber-coupled twin beams through a FWM process in a hot ^{85}Rb vapor cell. The pump and seed probe beams are delivered via polarization-maintaining fibers and overlap at the center of the vapor cell to establish the phase-matching geometry. The nonlinear interaction amplifies the probe and simultaneously generates the conjugate beam on the opposite side of the pump. After the cell, the probe and conjugate are coupled back to polarization maintaining fibers using f–to-f optical systems. Flip mirrors allow switching between direct free-space detection and fiber-coupled detection, enabling comparison of squeezing performance before and after fiber delivery. Reprinted with permission from [48]. 55
5.2 Illustration of momentum correlations imposed by the phase-matching condition in four-wave mixing. (a) For an idealized pump with infinite transverse extent, the $\vec{k}$-vectors of the probe and conjugate are correlated one-to-one in momentum space. (b) For a finite pump size, the spread of $\vec{k}$-vectors of the pump leads to correlations between probe $\vec{k}$-vectors and multiple conjugate $\vec{k}$-vectors, producing multiple coherence areas in the far field. Reprinted with permission from [48]. 59
5.3 Photograph of the compact experimental setup for generating fiber-coupled twin beams via four-wave mixing in a hot ^{85}Rb vapor cell. The pump and probe beams are delivered through polarization-maintaining fibers, collimated and overlapped at the center of the vapor cell housed in a temperature-controlled oven. After the nonlinear interaction, the amplified probe and conjugate are collected with f–to-f imaging systems (focal lengths 100 mm probe arm, 125 mm conjugate arm) and coupled back into PM fibers with $> 90\%$ efficiency. Reprinted with permission from [48]. 62
5.4 Intensity–difference noise normalized to the SNL (blue, 0 dB): squeezing before the output fibers (yellow, ≈ -7.2 dB), squeezing at the *output* of the fibers (red, -4.4 dB at 1 MHz), and the *expected* squeezing for a simple 10% pure-loss model (green, ≈ -6.3 dB at 1 MHz). Experimental conditions: pump power 135 mW, pump–probe crossing angle 0.4°, 12 mm ^{85}Rb cell. Reprinted with permission from [48]. 64

6.1 Schematic of an FBG: An FBG consists of a short section of optical fiber with a periodic refractive-index variation in its core effectively acting as a diffraction grating. This grating makes certain wavelengths reflect back and others transmit depending on the grating separation. Here blue arrow represents reflected light and the yellow arrow represents transmitted light. 71
6.2 Reflection response of an FBG sensor. The central wavelength is called Bragg wavelength. 71
6.3 Operational principle of FBG sensor: Wavelength shift in FBG response due to a strain or temperature variation: Any perturbations in the temperature or strain causes a shift in effective Bragg wavelength. If the perturbation is periodic, the whole reflection spectrum shifts back and forth periodically. . . 72

6.4 Measured reflection spectra of the 795 nm fiber Bragg grating for three different temperatures: 20°C (red), 40°C (blue), and 60°C (gray). The Bragg wavelength shifts to longer wavelengths as the temperature increases due to the combined thermo-optic and thermal expansion effects. 75
6.5 Measured reflection spectra of the 795 nm fiber Bragg grating for two orthogonal input polarization states: The blue trace corresponds to the reference polarization at 40 °C, while the orange trace represents the orthogonal polarization. The latter shows a slight shift toward shorter wavelength due to the lower effective refractive index experienced by the fast-axis polarization of the PM fiber. 77
6.6 Experimental layout for quantum enhanced FBG sensing: Twin-beams are coupled to FBG1 and FBG2 in separate arms, reflected back probe and conjugate beams are collected on two photo detectors for intensity difference noise measurement. Mechanical vibration signals in the FBGs are emulated from two piezo attached mechanically to the FBGs and modulated separately with common background noise (B) and a signal (S) on one of the FBGs. All mechanical vibrations couple to the intensity modulation signal in the FBGs that is measured on spectrum analyzer. 80
6.7 Mechanical excitation scheme for generating dynamic strain in the fiber Bragg gratings: The FBG fiber is clamped between two rigid posts, with a piezoelectric actuator attached to one post. Voltage signals applied to the piezo induce controlled vibrations and strain in the grating, producing time-dependent shifts in the Bragg wavelength that are converted into optical intensity modulations. A TEC is also put in contact with the FBG to have additional control over the response of the FBG, and therefore reflection, by varying the temperature slightly. 83
6.8 Spectral characterization of the twin-beam after interfacing with the FBG sensors with only one of them with an applied 400 kHz modulation: The blue trace is the shot-noise reference, the yellow trace shows the reduced squeezing level after fiber coupling and reflection from the FBG, and the red trace shows the initial squeezing directly after the Rb cell. The modulation peak at 400 kHz is clearly visible above the squeezed-noise floor, demonstrating successful transduction of the strain signal onto the intensity-difference measurement. 87
6.9 Modulaiton configuration used for two-tone coherent-light test. FBG2 is driven with a background modulation at 200 kHz (Mod B) and a signal at 400 kHz (Mod S), while FBG1 remains unmodulated. This arrangement allows the background and signal components to appear distinctly in the intensity-difference spectrum, enabling characterization of the sensor response prior to common-mode cancellation. 89
6.10 Measured spectral response for the configuration shown in Fig. 6.9. The blue trace represents the shot-noise reference, while the orange trace shows the detected spectrum when the two-tone modulation is applied to FBG2 only. Two prominent peaks appear at 200 kHz and 400 kHz, corresponding to the background component and the signal, respectively. This measurement establishes the baseline response before applying common-mode cancellation techniques. 90

6.11 Configuration for demonstrating common-mode cancellation using a dual FBG configuration with coherent light. Both FBG1 and FBG2 are driven with an identical 200 kHz background modulation (Mod B), while FBG2 also senses the 400 kHz signal (Mod S). By adjusting the phase and amplitude of the 200 kHz drive for FBG1, the background components can be made to interfere destructively in the intensity-difference measurement. 91
6.12 Measured spectral response for the dual-modulation configuration shown in Fig. 6.11. The blue trace is the shot-noise reference, while the yellow trace shows the detected spectrum when both FBGs are driven with a 200 kHz background modulation and FBG2 with the additional 400 kHz signal. By tuning the amplitude and phase of the background drive on FBG1, the 200 kHz background peak is completely canceled, leaving only the 400 kHz signal peak. This result demonstrates active common-mode suppression in the dual-FBG system. 92
6.13 Oscilloscope traces showing multiple segments of 15 msec each. V1 and V2 are photodiode measured voltages from FBG1 and FBG2, Ref is the input signal to the FBG1 PZT from the function generator and Trigger trace is from the function generator, used to define the start of each acquisition window. 97
6.14 Comparison of the averaged post-processed differential spectrum and the shot-noise (SN) reference. The black trace shows the cross-weighted differential spectrum of FBG1 and FBG2, obtained by applying the transfer function of each arm to the opposite channel prior to subtraction. The pink trace shows the corresponding shot-noise spectrum extracted from the no-drive dataset using the same analysis procedure. The red and blue traces show individual cross-weighted spectrum of FBG1 and FBG2. 101

7.1 Schematic of plasmonic sensor:(a) Plasmonic sensor with circular nanohole structures in a silver metal film over a glass substrate. (b) Photon-plasmon-photon conversion process resulting in transmission for a particular resonance wavelength. 107
7.2 Extraordinary Transmission: Transmission spectrum of a plasmonic sensor with the resonance wavelength at the center shown with a vertical line. 108
7.3 Shifted EOT spectrum for dual probing scheme: Transmission spectra of a plasmonic sensor corresponding to two orthogonally polarized probing beams. 110
7.4 Normalized transmission spectra from plasmonic sensor for two orthogonally polarized twin beams. T_p and T_c are the transmission value at 795 nm for prob beam (red trace) and conjugate beam (blue trace), respectively. 111
7.5 Unit cell used for COMSOL simulation of the plasmonic structure consisting of circular nanoholes in a silver metal layer over a glass substrate. (a) Silver nanohole structure with glass substrate at the bottom and air at the top. (b) Zoomed in image of unit cell made out of a silver film with a circular nanohole. The lengths along x and y axes of the unit cell defines the periodicities of the nano-hole structure in x and y directions, respectively. 117

7.6 Transmission spectra simulation obtained through COMSOL for optimal parameters of the nanohole arrays. The red trace corresponds to the probe, polarized along the larger periodicity, and the blue trace corresponds to the conjugate, polarized perpendicular to the probe. 118
7.7 Quantum Fisher information as the level of squeezing increases from 0 to 10 dB as a function of wavelength for: (a) blue trace (conjugate) and (b) red trace (probe) in Fig. 7.6 119
7.8 Plasmoic sensor specifications: dimensions and periodicities of the nanohole structures as optimized with COMSOL simulations to get the maximum QFI for two orthogonal linearly polarized light beams at 795 nm for a 0 degree (left sensor), 2 degree (middle sensor), and 4 degree (right sensor) angle of incidence. 120
7.9 Experimental setup for transmission response measurements of a plasmonic sensor using a broadband white light source. The light first passes through a broadband Glan Thompson polarizer that is used to linearly polarize the incoming light, then a broadband half wave plate that is used to change the polarization of the light. Afterwards, a combination of achromatic lenses L1 and L2, along with an iris is used to image the source onto the sensor with a reduced beam size that can be controlled with the iris. The transmitted light from the sensor is finally collected and sent to the spectrometer with the help another achromatic lens. 122
7.10 Response of fabricated plasmonic sensors:(a) Measured transmission spectra (solid curves) for fabricated arrays compared with numerical calculations (dashed curves) from COMSOL, for parameter values measured from the (b) SEM image of the corresponding sensor with nanohole diameter of: 287 nm, and periodicities of 473 nm and 485 nm along the x and y axis, respectively. . 124
7.11 Schematic of the experimental setup. The twin beams (probe and conjugate) generated with FWM are overlapped and sent through a plasmonic sensor inside a chamber and transmitted beams are again separated for intensity difference noise measurement. The setup is used to detect small changes in the refractive index of air with a sensitivity below the shot noise limit. 126
7.12 3D rendering of a plasmonic structure inside a hermetically sealed chamber used to provide a controlled modulation of the air refractive index with an ultrasonic transducer. 128
7.13 Direct squeezing measured without losses (bypassing sensor and beam splitters to overlap and separate probe and conjugate beams). The blue trace represents the shot-noise and red trace represents the squeezing. The traces are averaged 10 times with a sweep time of 3 seconds. 130
7.14 Measured squeezing with the plasmonic sensor: SNL normalized traces at 200 kHz and zero span. The blue trace represents shot noise, the red trace represents the measured squeezing when probe and conjugate go through the setup without the plasmonic structure in place and the yellow trace represents the amount of squeezing when probe and conjugate beams also pass through the plasmonic structure. The traces are for zero span and averaged 10 times over a sweep time of 3 seconds. 132

7.15 Detection of a 200 kHz modulation signal using twin-beam probing: The black trace represents the shot noise, the maroon trace represents the squeezing with both probe and conjugate bypassing only the sensor, the blue trace represents the squeezing measurement when both probe and conjugate beam pass through the sensor, and the orange trace represents the squeezing with both probe and conjugate passing through the sensor with an applied modulation at 200 kHz with 1 Volt amplitude signal input to the ultrasound transducer. All the traces corresponds to a span of frequencies from 199 kHz to 201 kHz and averaged 10 times over a sweep time of 3 seconds. 134
7.16 Normalized squeezing traces at 200 kHz and zero span: The blue represents the SNL, the red trace represents SNL with signal, the yellow trace represents amount of squeezing when probe and conjugate beams pass though the sensor and the purple trace represents squeezing with signal modulation. The orange (green) trace represents measured squeezing traces with probe (conjugate) pass through sensor and conjugate (probe) is used as reference. The traces are for zero span and averaged 10 times over a sweep time of 10 seconds. 137

Abstract

Quantum metrology leverages quantum resources to surpass classical limits in measurement sensitivity, enabling new capabilities across fields ranging from fundamental physics to sensing, imaging, and navigation. As these techniques mature, an increasing emphasis is being placed on translating quantum-enhanced performance into practical, robust systems that can operate outside controlled laboratory environments. The overarching objective of the work presented in this dissertation is to develop sensing platforms that achieve improved performance by leveraging quantum resources in realistic, noisy environments. In particular, this work focuses on the use of squeezed states of light, and investigates how two-mode squeezed states generated through four-wave mixing can be developed into compact sources and integrated with practical fiber-optic and plasmonic sensing platforms.

Squeezed states of light, and in particular two-mode squeezed states (twin beams), constitute a powerful resource in quantum metrology. Their reduced quantum noise enables measurements below the noise level that can be achieved with classical resources, know as the shot-noise limit, offering genuine quantum advantages in precision sensing and measurement. Beyond their fundamental interest, such states provide a pathway toward practical quantum technologies capable of outperforming classical approaches in real-world applications. For many practical implementations, it is therefore highly advantageous to demonstrate squeezed light sources that are compact, stable, and compatible with existing photonic infrastructures. This is needed to lower the barrier

to incorporate quantum resources into experiments and sensing platforms, particularly in environments where bulky or delicate optical setups are impractical.

To demonstrate a pathway toward practical quantum sensing with squeezed light, this dissertation presents experimental studies spanning both the development of deployable squeezed-light sources and their application in practical or real-world sensing platforms. We present the development of a compact, narrowband, fiber-coupled source of squeezed light based on four-wave mixing in hot ^{85}Rb vapor. The system achieves more than 4 dB of intensity-difference squeezing after propagation through polarization-maintaining fibers, demonstrating that strong quantum correlations can be preserved even when fiber coupled. This platform serves as a standalone proof-of-principle demonstration of a deployable, low–size, weight, and power (low-SWaP) squeezed-light source that is well suited for applications where fiber delivery of quantum-correlated light can be readily integrated into existing experimental and sensing platforms.

In addition to this source development, the dissertation investigates two distinct applications of twin-beam for quantum-enhanced sensing. The first one focuses on fiber Bragg grating (FBG) sensors, which are widely used to monitor strain, vibration, and temperature in applications ranging from civil infrastructure and aerospace systems to oil and gas pipeline monitoring. By coupling the squeezed light into separate FBGs and employing differential detection, common-mode noise is suppressed while localized perturbations are retained. This work provides a feasibility study for using twin-beams to enhance the sensitivity of FBG-based sensors beyond classical limits while providing robustness against environmental noise.

The second application examines plasmonic sensors based on surface plasmon resonances in metallic nanostructures, which enable highly sensitive detection of small changes in refractive index. Such plasmonic sensors are particularly useful for applications in chemical and biological sensing, environmental monitoring, and lab-on-chip platforms, where compactness and high sensitivity to refractive index changes are critical. A dual-probing scheme is introduced in which both beams of a two-mode squeezed state interact with a polarization-dependent plasmonic nanostructure. By exploiting opposite spectral response for orthogonal polarizations, this approach improves measurement sensitivity relative to our previous technique of using one beam to probe the plasmonic sensor and the other to serve as a reference. This new technique takes advantage of transducing information into both the beams while preserving the benefits of differential detection for noise cancellation.

Taken together, these studies illustrate complementary approaches for leveraging quantum correlations for practical sensing problems. Through the development of a compact, fiber-compatible squeezed-light source and independent demonstrations of enhanced performance in both fiber-optic and plasmonic sensors, this dissertation advances pathways for translating quantum sensing approaches based on quantum states of light from laboratory demonstrations into deployable metrology tools.

Patents, Publications and Conference Presentations

Patents

1. A. M. Marino, J. Sharma, S. Kim, U. Jain, and J. Tabjula, "Enhanced Sensitivity Fiber Bragg Grating Sensors and Methods of Use," *Ser. No. 19/335,412 (2025) (in submission).*

Publications

1. U. Jain, and A. M. Marino, "Quantum-Enhanced Sensing with Dual Probing Twin Beams," *(in preparation).*

2. U. Jain, and A. M. Marino, "Quantum-Enhanced Fiber Bragg Grating Sensing in Noisy Environments," *(in preparation).*

3. U. Jain, J. Choi, C. Hull, and A. M. Marino, "Compact Fiber-Coupled Narrowband Two-Mode Squeezed Light Source," *Optics Letters* **50**, 5165–5168 (2025).

4. M. Dowran, A. L. Win, U. Jain, A. Kumar, B. J. Lawrie, R. C. Pooser, and A. M. Marino, "Parallel Quantum-Enhanced Sensing," *ACS Photonics* **11**, 3037–3045 (2024).

5. S. Sanders, A. Kumar, M. Dowran, U. Jain, B. J. Lawrie, R. C. Pooser, and A. M. Marino, "Lattice Resonances of Nanohole Arrays for Quantum-Enhanced Sensing," *Phys. Rev. Applied* **17**, 014035 (2022).

Conference Presentations

1. U. Jain, and A. M. Marino, "Quantum-Enhanced Fiber Bragg Grating Sensors in the Presence of Background Noise," 56$^{\text{th}}$ Annual Meeting of the APS Division of Atomic, Molecular, and Optical Physics (DAMOP), June 2025, Portland, Oregon, USA (Talk).

2. U. Jain, J. Choi, C. Hull, and A. M. Marino, "Quantum Sensing with Fiber Bragg Grating Sensors," 55$^{\text{th}}$ Annual Meeting of the APS Division of Atomic, Molecular, and Optical Physics (DAMOP), June 2024, Fort Worth, Texas, USA (Poster Presentation).

3. U. Jain, J. Choi, C. Hull, and A. M. Marino, "Fiber-Coupled Twin Beams from Four Wave Mixing in Rubidium," 53$^{\text{rd}}$ Annual Meeting of the APS Division of Atomic, Molecular, and Optical Physics (DAMOP), June 2022, Orlando, Florida, USA (Poster Presentation).

4. M. Dowran, U. Jain, and A. M. Marino, "Parallel Quantum Sensing with Spatially Multimode Twin Beams of Light," 52$^{\text{nd}}$ Annual Meeting of the APS Division of Atomic, Molecular, and Optical Physics (DAMOP), June 2021 (Online Talk).

5. U. Jain, M. Dowran, and A. M. Marino, "Enhanced Quantum Sensing with Dual Probing Twin Beams," 52$^{\text{nd}}$ Annual Meeting of the APS Division of Atomic, Molecular, and Optical Physics (DAMOP), June 2021 (Online Poster Presentation).

List of Acronyms

AOM	acousto-optic modulator
SWaP	size weight and power
BS	beam splitter
QCRB	quantum Cramer-Rao bound
EOM	electro-optic modulator
EOT	extraordinary optical transmission
FBG	fiber Bragg grating
FWM	four-wave mixing
TB	twin beams
LIGO	Laser Interferometer Gravitational-Wave Observatory
OPO	optical parametric oscillator
PBS	polarizing beam splitter
PSD	power spectral density
PZT	piezoelectric transducer
QFI	quantum Fisher information
TEC	thermoelectric cooler
SNL	shot noise limit

Chapter 1

Introduction

The study of light and its interaction with matter has been central to modern physics, leading to breakthroughs that not only deepened our understanding of nature but also transformed technology. From the invention of the laser to the development of precision measurement tools, progress in optics has repeatedly pushed the boundaries of what can be measured and controlled [1, 2]. Over the past several decades, research in quantum optics has revealed that light can be prepared in nonclassical states with properties unattainable by classical sources [3, 4]. Among these, squeezed states of light have attracted particular attention because of their ability to reduce noise beyond what can be achieved with classical resources, given by the shot-nose limit for optical systems, opening the door to measurements with unprecedented sensitivity [5, 6].

This capability is especially significant as metrology applications increasingly demand precision at the precision that cannot be attained with classical systems. The recognition that quantum resources such as superposition, entanglement, and squeezing can outperform classical strategies has given rise to what is often described as the "second quantum revolution," where concepts once considered primarily a focus of fundamental science are being translated into practical technologies [7, 8]. In this context, squeezed states of light, and in particular two-mode squeezed states or twin beams, have become a versatile tool for enhancing sensing platforms [9, 10]. These quantum states enable a direct path toward improving optical sensors that are already

widely used in science, engineering, and industry, bridging the gap between fundamental quantum optics and real-world metrology [11, 12].

However, a central challenge remains in translating these quantum advantages from laboratory demonstrations into practical sensing technologies. Many current implementations rely on complex and sensitive optical systems that are not readily adaptable to real-world environments. The work presented in this dissertation aims to bridge this gap by developing and applying two-mode squeezed states of light in compact and application-oriented sensing platforms, including fiber-optic and plasmonic systems.

1.1 Quantum Revolution

The first quantum revolution emerged in the early twentieth century with the formulation of quantum mechanics, fundamentally altering our understanding of matter, light, and measurement. Phenomena such as wave–particle duality, the quantization of energy, and the probabilistic interpretation of physical laws demonstrated that classical physics could not provide a complete description of nature [13, 14, 15]. This theoretical shift not only deepened our grasp of fundamental science but also gave rise to practical technologies that continue to define the modern world. Semiconductors, lasers, transistors, and magnetic resonance imaging are just a few examples of devices that rely directly on principles first uncovered through quantum mechanics [16, 1, 17].

Within this broader transformation, the field of quantum optics established itself as

a central player. The invention of the laser in 1960 provided coherent light sources with unprecedented stability and control [1]. Lasers became indispensable for spectroscopy, telecommunications, and precision measurements, but they also revealed the intrinsic fluctuations dictated by quantum mechanics. The uncertainty principle dictates that the quadratures of the electromagnetic field cannot both be measured with arbitrary precision, introducing unavoidable quantum noise into measurements [18, 4]. This quantum noise defines the so-called shot-noise limit (SNL), a bound that constrains the sensitivity of classical optical measurements regardless of improvements in the experimental apparatus [5].

What initially appeared as a barrier soon became an opportunity. In 1963, Roy Glauber developed the quantum theory of coherence, providing the mathematical tools to describe quantum states of light [3]. His work laid the foundation for understanding that certain nonclassical states, such as squeezed states, can redistribute quantum noise between quadratures without violating the uncertainty principle [4, 19]. This realization was transformative, as it suggested that the SNL could be surpassed by carefully engineering the quantum state of the electromagnetic field. The first experimental demonstration of nonclassical light appeared in 1977, when Kimble and Mandel observed photon antibunching in resonance fluorescence from a single atom [20]. This was followed in 1985 by Slusher and colleagues, who reported the first observation of squeezed states of light through nonlinear interactions in sodium vapor [6]. These experiments confirmed that quantum states of light can be generated and controlled in the laboratory, opening the door to new regimes of measurement precision.

The first quantum revolution not only transformed our conceptual framework but also seeded the experimental techniques that continue to shape modern physics. Theoretical advances coupled with experimental breakthroughs established quantum optics as a powerful platform where the quantum nature of light could be harnessed directly [3, 4]. These developments set the stage for what is now referred to as the second quantum revolution, where the focus has shifted from understanding fundamental phenomena to deliberately engineering quantum states for technological applications [7].

1.2 Second Quantum Revolution and Quantum Sensing

While the first quantum revolution transformed science and technology through the discovery and exploitation of quantum principles, the second quantum revolution represents a shift in how we deliberately harness these principles to design and control complex quantum systems. Beginning in the late 20th and early 21st centuries, researchers gained the ability not only to observe quantum phenomena but to engineer them in ways that could outperform their classical counterparts [7]. This era is characterized by advances in quantum information, quantum communication, quantum computation, and quantum sensing, where quantum resources such as superposition, entanglement, and squeezing are no longer curiosities but tools that can be leveraged for real technologies [8, 9].

Quantum sensing, in particular, has emerged as one of the most promising frontiers of this revolution. Classical optical sensors are inherently limited by the SNL, which

arises from the discrete nature of photons or particles. Quantum optical sensors exploit nonclassical states of light, such as squeezed states, entangled states, or states in a coherent superposition, to achieve sensitivities beyond this limit [5, 21]. This enables measurements with higher resolution, smaller uncertainties, and access to sensitivities that would be inaccessible with classical strategies. One widely used approach, particularly relevant to squeezed-state metrology, relies on a simple principle: by using correlations or reduced fluctuations in carefully prepared quantum states, one can reduce measurement noise in the observable of interest, while satisfying the uncertainty principle [4].

The impact of quantum sensing is already being felt across diverse fields. In optics, squeezed light has been used to enhance interferometric measurements, with the most prominent example being the Laser Interferometer Gravitational-Wave Observatory (LIGO), where the use of squeezed states reduces quantum noise and improves the detection of gravitational waves [22, 23]. In atomic physics, cold-atom interferometers are being developed for navigation, geodesy, and tests of fundamental physics [24, 25]. Other applications include chemical detection, biomedical imaging, and nanoscale sensing, where surpassing classical limits can yield dramatic improvements in performance [11]. Quantum-enhanced spectroscopy, microscopy, and precision timekeeping illustrate how these techniques extend far beyond traditional laboratory physics into practical technologies [12].

In this sense, quantum sensing exemplifies the spirit of the second quantum revolution. It not only deepens our understanding of the quantum world but also demonstrates clear

technological advantages in real-world settings. By harnessing entanglement, squeezing, and other nonclassical resources, quantum sensors can probe weaker signals, operate in noisier environments, and open up entirely new application domains [10, 12]. This paradigm shift bridges the gap between fundamental physics and deployable technology, marking a critical step toward integrating quantum systems into everyday scientific and practical tools [7].

1.3 Thesis Outline

This dissertation is organized into eight chapters, each addressing a distinct aspect of the motivation, theory, and implementation of quantum-enhanced sensing using two-mode squeezed light. Chapter 1 provides a general introduction and contextual background, including the historical development of quantum mechanics, the first and second quantum revolutions, and the emergence of quantum sensing as a central area of applied quantum science. Chapter 2 reviews the theoretical foundations of quantum optics that are relevant for this work. It introduces the quantum picture of coherent and squeezed states of light, and the properties of two-mode squeezed states (twin beams).

Chapter 3 focuses on the generation of twin beams through four-wave mixing (FWM) in hot rubidium vapor. It describes the relevant atomic energy-level scheme, the role of pump and seed fields, the experimental apparatus required to generate two-mode squeezing and the properties of the generated states. Optimization strategies, operating conditions, and measurement techniques for quantifying squeezing are also presented.

Chapter 4 establishes the conceptual framework for quantum-enhanced sensing. It introduces fundamental noise limits in measurement, reviews sensing strategies based on squeezed states, and discusses sensitivity bounds using tools such as the quantum Fisher information, providing a bridge between twin beam generation and the sensing applications explored in later chapters.

Chapter 5 then turns to the development of a compact, narrowband, fiber-coupled source of squeezed light. The design goals and low-SWaP considerations are outlined, followed by a discussion of fiber coupling and performance evaluation. The results demonstrate large levels of noise reduction after fiber delivery, representing an important step toward deployable quantum-enhanced sensors.

The next two chapters focus on applications of twin beams to optical sensing platforms. Chapter 6 explores quantum-enhanced fiber Bragg grating (FBG) sensors, where the probe and conjugate beams interrogate separate FBGs. By implementing differential detection, common-mode noise suppression is achieved while localized perturbations are preserved. This work demonstrates the potential of this approach for applications such as structural health monitoring and pipeline leak detection. Chapter 7 extends the use of twin beams to plasmonic sensors, which exploit polarization-dependent resonances in nanostructured metallic devices. Such sensors are widely investigated for chemical and biological sensing, environmental monitoring, and lab-on-chip platforms, where compactness and high sensitivity to refractive-index changes are essential. A dual-probing scheme is introduced, in which both modes of the twin beams interact with the plasmonic nanostructure. Experimental results highlight the advantages of this

approach, including enhanced sensitivity compared to single-beam probing strategies.

Finally, Chapter 8 summarizes the main results of this dissertation and discusses their broader implications. Future research directions are outlined, including improvements to compact squeezed-light sources, scaling to multiplexed sensing architectures, and integration with photonic and plasmonic platforms for practical quantum technologies. Together, all these chapters trace a progression from theoretical foundations, to experimental generation of quantum states of light, to their adaptation for compact sources and real-world sensing applications.

Chapter 2

Quantum Light: Squeezed States of Light

The quantum description of light departs fundamentally from the classical wave picture by recognizing that the electromagnetic field itself is quantized. This quantization gives rise to phenomena such as photon statistics, vacuum fluctuations, and the unavoidable quantum noise associated with measurement. While classical optics is often sufficient to describe many systems, a quantum framework becomes essential whenever fluctuations at or below the SNL play a significant role. Within this framework, the vacuum is not simply the absence of photons but a fluctuating ground state of the quantized electromagnetic field, exhibiting fluctuations that manifests in observable ways, setting the ultimate noise floor for optical measurements [3].

One of the most important classes of quantum states for metrology are squeezed states of light. These are nonclassical states in which the noise in one field quadrature is reduced below the SNL, at the cost of increased fluctuations in the conjugate quadrature, consistent with the Heisenberg uncertainty principle [5, 19]. The ability to redistribute quantum noise between quadratures makes squeezed light a powerful resource for precision measurement, allowing sensitivities beyond the classical limit. Experimental demonstrations of squeezed states date back to the mid-1980s [6], and their applications have since expanded to areas ranging from gravitational wave detectors [22] to quantum imaging and spectroscopy [26, 11].

The concept of squeezing naturally extends to two-mode systems, where quantum

correlations between a pair of optical fields lead to noise suppression in joint quadrature observables formed from both modes [27, 28]. The two mode squeezed states of light or twin beams are central to this dissertation, as they provide a practical and versatile path to quantum-enhanced sensing [10]. Before discussing sensing applications of two mode squeezing in detail; however, it is useful to briefly review the quantum picture of the electromagnetic field, the nature of coherent and squeezed states, and the methods used to detect and characterize them. These topics are covered in the following sections.

2.1 Quantum Mechanical Description of Light

In quantum mechanics, physical observables are represented by operators rather than classical variables. In general, these operators do not commute, leading to intrinsic limits on the precision with which certain pairs of observables can be simultaneously measured. This fundamental limitation is expressed by the Heisenberg uncertainty principle and has no classical analogue [18].

For any two Hermitian operators $\hat{A}$ and $\hat{B}$ representing conjugate observables, the uncertainty principle states that the product of their variances satisfies

$$\langle(\Delta\hat{A})^2\rangle \langle(\Delta\hat{B})^2\rangle \geq \frac{1}{4}\left|\langle\hat{C}\rangle\right|^2, \tag{2.1}$$

where the operator $\hat{C}$ is defined through the commutation relation

$$\hat{C} = i[\hat{A}, \hat{B}]. \tag{2.2}$$

Here, the variance of an operator $\hat{A}$ is defined as

$$\langle(\Delta\hat{A})^2\rangle = \langle\hat{A}^2\rangle - \langle\hat{A}\rangle^2, \tag{2.3}$$

and similarly for $\hat{B}$. This relation highlights a key departure from classical physics: even in the absence of technical noise, quantum fluctuations impose a fundamental limit on the simultaneous knowledge of noncommuting observables.

A quantum mechanical description of light is obtained by quantizing the electromagnetic field. As introduced by Glauber [3], a single-mode monochromatic electric field of angular frequency ω can be modeled as a quantized harmonic oscillator and written as

$$\hat{E}(t) = E_0 \left(\hat{a} e^{-i\omega t} + \hat{a}^\dagger e^{i\omega t} \right), \tag{2.4}$$

where $\hat{a}$ and $\hat{a}^\dagger$ are the annihilation and creation operators, respectively, and

$$E_0 = \sqrt{\frac{\hbar\omega}{2\epsilon_0 V}} \tag{2.5}$$

is the electric field amplitude associated with a single mode confined to a volume V. The operators $\hat{a}$ and $\hat{a}^\dagger$ obey the bosonic commutation relation $[\hat{a}, \hat{a}^\dagger] = 1$ and act to lower or raise the photon number of the field, respectively.

Since the annihilation and creation operators are non-Hermitian, they do not correspond directly to measurable quantities, so it is convenient to express the field in terms of Hermitian quadrature operators. We can write the annihilation operator as

$$\hat{a} = \hat{X} + i\hat{Y}, \tag{2.6}$$

the electric field operator can be rewritten as

$$\hat{E}(t) = 2E_0 \left[\hat{X} \cos(\omega t) + \hat{Y} \sin(\omega t) \right], \tag{2.7}$$

where $\hat{X}$ and $\hat{Y}$ are the field quadrature operators corresponding to the real and imaginary components of the complex field amplitude. These operators define the

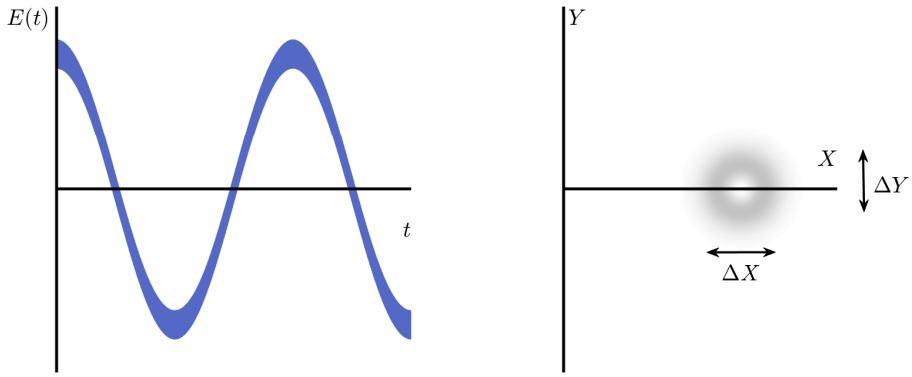


Figure 2.1: Phase-space representation of an electric field: The electric field (left) can be described in phase-space representation (right) by its in and out of phase components $\hat{X}$ and $\hat{Y}$ that are equivalent to the real and imaginary parts of the complex electric field respectively.

amplitude and phase quadratures of the electric field and form the orthogonal axes of the phase-space representation shown in Fig. 2.1. This representation provides a convenient framework for visualizing and analyzing quantum fluctuations of the optical field.

The quadrature operators satisfy the commutation relation

$$[\hat{X}, \hat{Y}] = \frac{i}{2}, \tag{2.8}$$

which leads directly to the uncertainty relation

$$\langle(\Delta\hat{X})^2\rangle \langle(\Delta\hat{Y})^2\rangle \geq \frac{1}{16}. \tag{2.9}$$

This uncertainty relation governs the quantum fluctuations of the electromagnetic field and establishes the fundamental noise floor for optical measurements. Different

quantum states of light are distinguished by how they distribute noise between these two quadratures, a concept that forms the basis for coherent and squeezed states discussed in the following sections.

2.2 Coherent States of Light

Coherent states are the quantum representation of classical states that most closely resemble classical monochromatic light. Coherent states are minimum-uncertainty states of the field quadratures and represent the lowest noise level achievable with classical states of light. They define the SNL, which serves as the fundamental sensitivity bound for optical measurements performed with classical resources [3, 5].

A coherent state $|\alpha\rangle$ is defined as an eigenstate of the annihilation operator,

$$\hat{a}|\alpha\rangle = \alpha|\alpha\rangle, \tag{2.10}$$

where $\alpha = |\alpha|e^{i\phi}$ is a complex number representing the amplitude and phase of the optical field. Equivalently, a coherent state can be generated by applying the displacement operator $\hat{D}(\alpha)$ to the vacuum state,

$$|\alpha\rangle = \hat{D}(\alpha)|0\rangle, \tag{2.11}$$

where the displacement operator is given by

$$\hat{D}(\alpha) = \exp\left(\alpha\hat{a}^\dagger - \alpha^*\hat{a}\right). \tag{2.12}$$

This shifts the vacuum state in phase space without altering its noise properties.

For a coherent state, the uncertainties of the field quadratures are equal and attain the minimum value allowed by the uncertainty principle,

$$\langle(\Delta\hat{X})^2\rangle = \langle(\Delta\hat{Y})^2\rangle = \frac{1}{4}, \tag{2.13}$$

such that the uncertainty relation

$$\langle(\Delta\hat{X})^2\rangle\langle(\Delta\hat{Y})^2\rangle = \frac{1}{16} \tag{2.14}$$

is saturated. In phase space, a coherent state is therefore represented by a circular uncertainty distribution centered at the point $(\langle\hat{X}\rangle, \langle\hat{Y}\rangle)$, with equal noise along both quadrature axes.

For sufficiently large amplitudes, $|\alpha| \gg 1$, coherent states provide a well-defined optical phase and closely approximate the output of an ideal laser. The phase-space representation of a coherent state is shown in Fig. 2.2 (a) with equal uncertainities in both the quadratures.

Because coherent states minimize quadrature uncertainties while maintaining equal noise in both conjugate variables, they define the fundamental noise limit for classical optical fields, below which classical states cannot operate, and therefore serve as the natural reference for identifying nonclassical states of light. Any reduction of noise below the coherent state level in a given quadrature can lead to a quantum advantage, as discussed in the following section on squeezed states of light.

2.3 Single-Mode Squeezed States

While coherent states define the minimum noise level achievable with classical light, quantum mechanics allows this limit to be surpassed through the redistribution of quantum fluctuations between conjugate quadratures. Single-mode squeezed states are nonclassical states of light in which the uncertainty in one quadrature is reduced below the SNL, at the expense of increased fluctuations in the conjugate quadrature, consistent with the Heisenberg uncertainty principle [18, 19].

It follows from Eq. (2.9) that for a squeezed state

$$\langle(\Delta\hat{X})^2\rangle < \frac{1}{4} \qquad \text{or} \qquad \langle(\Delta\hat{Y})^2\rangle < \frac{1}{4}. \tag{2.15}$$

Such states can be either amplitude squeezed (if the first condition is satisfied) or phase squeezed (if the second condition is satisfied). Figures 2.2 (b) and (c) show the phase space representation of squeezed states by an ellipse with its minimum axis aligned with $\hat{X}$ direction for amplitude squeezed and the $\hat{Y}$ direction for phase squeezed states [19, 29].

Squeezing can be described by the unitary squeezing operator

$$\hat{S}(\zeta) = \exp\left[\frac{1}{2}\left(\zeta^*\hat{a}^2 - \zeta\hat{a}^{\dagger 2}\right)\right], \tag{2.16}$$

where $\zeta = se^{i\theta}$ is the complex squeezing parameter, with s denoting the magnitude of squeezing and θ determining the orientation of the noise ellipse in phase space. Acting on the vacuum state, the squeezing operator produces a single-mode squeezed vacuum state [30, 4].

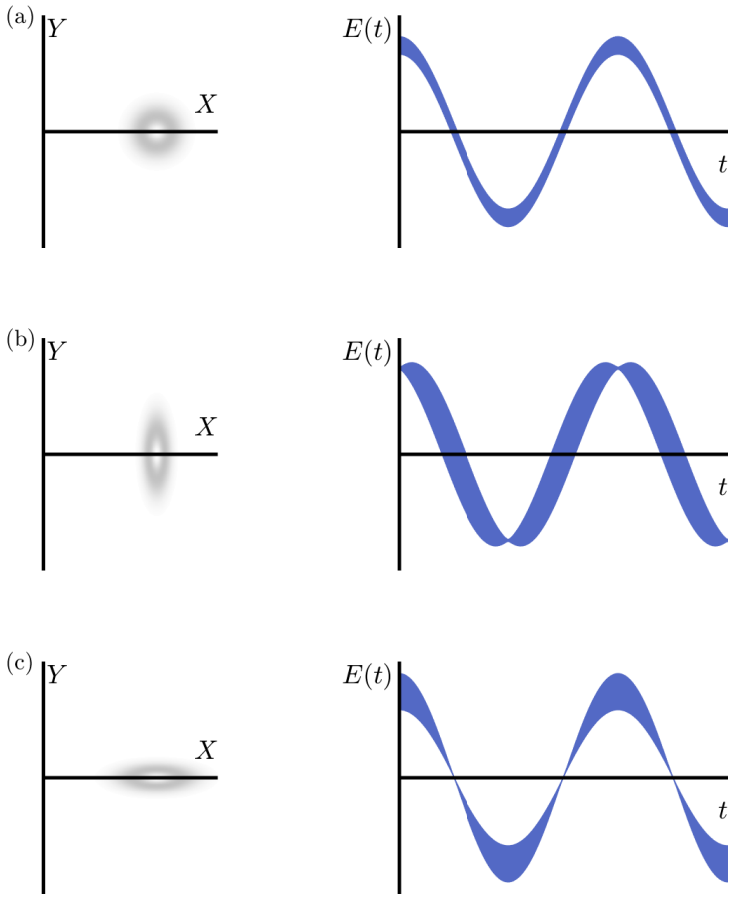


Figure 2.2: Phase-space distribution and corresponding electric field behavior for (a) a coherent state, (b) an amplitude-squeezed state, (c) and a phase-squeezed state.

In experimental implementations, vacuum displaced states are often squeezed to produce bright squeezed states, which can be written as

$$|\alpha, \zeta\rangle = \hat{S}(\zeta)\hat{D}(\alpha)|0\rangle, \tag{2.17}$$

where $\hat{D}(\alpha)$ is the displacement operator. Bright squeezed states combine a large coherent amplitude with reduced quantum noise in a selected quadrature, while the orthogonal quadrature exhibits increased fluctuations due to the uncertainty principle. These states retain the phase reference provided by the coherent displacement, enabling phase-sensitive detection schemes while benefiting from noise reduction below the shot-noise limit [5]. As a result, they are particularly useful for precision measurements where high optical power and reduced noise are both required.

Single-mode squeezed states provide enhanced sensitivity in measurement schemes where the signal is encoded in a specific quadrature of the field. For example, in interferometric measurements, phase variations are mapped onto one quadrature, and squeezing that quadrature leads to improved sensitivity. However, this enhancement is limited to the particular quadrature being measured, while the orthogonal quadrature remains anti-squeezed [5, 9].

2.4 Two-Mode Squeezed States

The concept of squeezing can be generalized from a single optical mode to multiple modes of the electromagnetic field. In a two-mode squeezed state, quantum correlations are established between a pair of optical modes, leading to noise reduction in joint

observables formed from both fields. These states are commonly referred to as two-mode squeezed states or twin beams [19, 10].

A two-mode squeezed state can be generated by the action of the two-mode squeezing operator on a pair of vacuum or coherent states,

$$\hat{S}_{a,b}(\zeta) = \exp\left(\zeta^* \hat{a}\hat{b} - \zeta \hat{a}^\dagger \hat{b}^\dagger\right), \tag{2.18}$$

where $\hat{a}$ and $\hat{b}$ are the annihilation operators of the two modes and $\zeta = se^{i\theta}$ is the squeezing parameter. In this process, photons are created or annihilated in pairs, one in each mode, giving rise to strong correlations between the two fields [5, 4].

While each individual mode of a two-mode squeezed state typically exhibits excess noise in its quadratures, appropriately defined joint quadratures can display squeezing below the SNL. Defining the collective quadrature operators as

$$\hat{X}_\pm = \frac{1}{\sqrt{2}}(\hat{X}_a \pm \hat{X}_b), \qquad \hat{Y}_\pm = \frac{1}{\sqrt{2}}(\hat{Y}_a \pm \hat{Y}_b). \tag{2.19}$$

These joint quadrature correlations reflect the nonclassical nature of twin beams and form the basis for intensity-difference squeezing [6].

The origin of squeezing in two-mode systems can be understood by examining the transformation of the field operators under the two-mode squeezing interaction. Applying the unitary operator $\hat{S}_{a,b}(\zeta)$ to the annihilation operators yields

$$\hat{S}^\dagger_{a,b} \hat{a}\, \hat{S}_{a,b} = \hat{a}\cosh(s) - \hat{b}^\dagger e^{i\theta}\sinh(s), \tag{2.20}$$

$$\hat{S}^\dagger_{a,b} \hat{b}\, \hat{S}_{a,b} = \hat{b}\cosh(s) - \hat{a}^\dagger e^{i\theta}\sinh(s), \tag{2.21}$$

which show that the two modes become correlated through the mixing of annihilation and creation operators. In particular, the appearance of the creation operator of one

mode in the transformation of the other mode (e.g., $\hat{b}^\dagger$ in $\hat{a}_{out}$ and $\hat{a}^\dagger$ in $\hat{b}_{out}$) indicates that photons are generated in correlated pairs across the two modes. This coupling between $\hat{a}$ and $\hat{b}^\dagger$ (and vice versa) is the signature of the two-mode squeezing interaction and gives rise to strong quantum correlations between the probe and conjugate fields.

As a consequence of these correlations, individual quadratures of each mode exhibit excess noise, while specific joint quadratures display reduced fluctuations. Evaluating the variances of the collective quadratures yields

$$\langle(\Delta\hat{X}_-)^2\rangle = \langle(\Delta\hat{Y}_+)^2\rangle = \frac{1}{4}e^{-2s}, \tag{2.22}$$

while the conjugate joint quadratures satisfy

$$\langle(\Delta\hat{X}_+)^2\rangle = \langle(\Delta\hat{Y}_-)^2\rangle = \frac{1}{4}e^{2s}. \tag{2.23}$$

Thus, the reduction of noise in the squeezed joint quadratures is accompanied by increased fluctuations in the orthogonal joint quadratures, in accordance with the uncertainty principle.

This simultaneous squeezing of commuting joint quadratures (such as $\hat{X}_-$ and $\hat{Y}_+$) is a distinctive feature of two-mode squeezed states and underlies their usefulness for differential and correlated measurement schemes, even though only one observable is typically measured in a given experiment. In practical sensing applications, these joint quadratures correspond to observables such as intensity difference or phase sum, which can be accessed experimentally with high efficiency [9, 10].

Two mode squeezed states play a central role in quantum-enhanced sensing schemes that rely on differential or correlated measurements. Their ability to suppress common-

mode noise while preserving sensitivity to differential signals makes them well suited for practical sensing platforms, as explored in later chapters of this dissertation [6, 11].

2.5 Nonlinear Processes to Generate Quantum States of Light

The generation of squeezed and entangled states of light relies fundamentally on nonlinear interactions between optical fields and matter. In linear optical media, the response of the medium is proportional to the electric field, and the evolution of the field does not introduce correlations between photons. As a result, linear processes cannot produce nonclassical states of light.

In contrast, nonlinear media enable interactions in which the optical field depends on higher powers of the electric field. These interactions give rise to processes in which photons are created or annihilated in correlated pairs. At the quantum level, this corresponds to terms involving products of creation and annihilation operators, such as $\hat{a}^2$, $\hat{a}^{\dagger 2}$ in the single-mode case, or $\hat{a}\hat{b}$ and $\hat{a}^\dagger\hat{b}^\dagger$ in the two-mode case. These are the same operator forms that appear in the squeezing operators introduced earlier, and therefore provide the physical mechanism for generating squeezed and entangled states of light [31].

At the macroscopic level, nonlinear optical processes are described through the polarization response of a medium,

$$\mathbf{P} = \epsilon_0 \left(\chi^{(1)}\mathbf{E} + \chi^{(2)}\mathbf{E}^2 + \chi^{(3)}\mathbf{E}^3 + \cdots \right), \tag{2.24}$$

where ϵ_0 is the vacuum permittivity and $\chi^{(n)}$ denotes the nth-order nonlinear suscepti-

bility. The polarization acts as a source term in Maxwell's equations and therefore plays a direct role in the generation of electromagnetic fields. This can be seen by writing the wave equation for the electric field in a nonlinear medium,

$$\nabla^2 \mathbf{E} - \frac{1}{c^2}\frac{\partial^2 \mathbf{E}}{\partial t^2} = \frac{1}{\epsilon_0 c^2}\frac{\partial^2 \mathbf{P}_{\mathrm{NL}}}{\partial t^2}, \tag{2.25}$$

where $\mathbf{P}_{\mathrm{NL}}$ denotes the nonlinear component of the polarization. Oscillating terms in $\mathbf{P}_{\mathrm{NL}}$ at new frequencies therefore act as driving sources that generate corresponding electromagnetic fields.

As a result, higher-order polarization terms give rise to new optical fields whose frequencies, phases, and amplitudes are determined by the interacting input fields. When these fields are generated through the same nonlinear interaction, their quantum properties become intrinsically linked. At the quantum level, this manifests as correlations between field fluctuations, providing the physical origin of squeezing and entanglement.

One widely used mechanism for generating nonclassical light is parametric down-conversion based on a second-order nonlinear response ($\chi^{(2)}$) in nonlinear crystals. In this process, a photon from a strong pump field is converted into a pair of lower-frequency photons that are correlated in energy, momentum, and phase [32, 33]. Depending on the phase-matching conditions and mode structure, parametric down-conversion can produce either single-mode or two-mode squeezed states.

While $\chi^{(2)}$ systems have been extremely successful in demonstrations of squeezing and entanglement, they typically require optical cavities or waveguides to achieve

high nonlinear interaction strengths. This requirement arises because the intrinsic $\chi^{(2)}$ response of most materials is relatively weak, as it originates from higher-order perturbations of the electronic polarization and is only present in non-centrosymmetric media. As a result, efficient nonlinear conversion typically requires either high optical intensities or long interaction lengths. Optical cavities and waveguides enhance the effective nonlinearity by increasing the field intensity through spatial confinement or by allowing the optical fields to interact repeatedly with the nonlinear medium.

An alternative approach exploits third-order nonlinearities ($\chi^{(3)}$), which are naturally present in many media, including optical fibers and atomic vapors. In $\chi^{(3)}$ processes, correlations arise from interactions involving four photons, most commonly in the form of four-wave mixing. In its simplest picture, two photons from a strong pump field are converted into a correlated photon pair occupying two distinct modes, commonly referred to as the probe and conjugate [34, 35].

Third-order nonlinearities become particularly advantageous in systems where second-order nonlinearities are absent or suppressed, or where strong field–matter interactions can compensate for the weaker intrinsic nonlinearity. In atomic vapors, near-resonant enhancement can dramatically increase the effective $\chi^{(3)}$ response, enabling efficient generation of quantum-correlated light without the need for optical cavities or engineered waveguides. This makes $\chi^{(3)}$ processes based on atomic vapor four-wave mixing especially attractive for generating narrowband squeezed states that are naturally compatible with atomic transitions and free-space optical geometries [34, 35].

From a quantum perspective, parametric nonlinear optical interactions, such as

parametric down-conversion and four-wave mixing, can be viewed as processes that create photons in correlated pairs while conserving energy and momentum. Because the photons are generated simultaneously through the same interaction, their quantum fluctuations become intrinsically linked. If the photons occupy the same optical mode, the result is a single-mode squeezed state; if they populate distinct modes, a two-mode squeezed state, or twin beams, is produced [4, 36].

A key requirement for efficient nonlinear interactions is phase matching, which ensures that the interacting optical fields remain phase coherent over the length of the nonlinear medium. When the phase-matching condition is satisfied, the nonlinear polarization generated at different positions within the medium adds constructively, allowing the newly generated fields to build up efficiently. If this condition is not met, destructive interference suppresses the nonlinear conversion process. Although the detailed phase-matching conditions depend on the specific medium and interaction, their role is universal across nonlinear optical systems. The phase-matching conditions relevant to four-wave mixing in atomic vapors are discussed in detail in Chapter 3.

In addition, resonant enhancement in atomic vapors can significantly increase the effective nonlinear susceptibility, allowing the generation of narrowband squeezed states without the use of optical cavities [37]. Among the various $\chi^{(3)}$ platforms, four-wave mixing in hot alkali vapor has emerged as a particularly attractive source of two-mode squeezed light. This approach combines high gain, narrow bandwidth, and direct compatibility with atomic transitions, making it well suited for applications requiring strong quantum correlations.

In the following chapter, we focus on four-wave mixing in hot rubidium vapor as a platform for generating twin beams. We discuss the underlying atomic-level processes, phase-matching conditions, and experimental implementations that enable strong two-mode squeezing.

Chapter 3

Twin-Beam Generation via Four-Wave Mixing in Hot Rubidium Vapor

The experimental realization of two-mode squeezed states used throughout this dissertation is based on the nonlinear process of four-wave mixing in hot rubidium vapor. FWM in atomic vapors provides a platform for generating bright twin beams with strong quantum correlations, and has been extensively studied as a source of squeezed light [34, 37, 35]. This chapter introduces the physical mechanism of FWM in rubidium, describes the experimental apparatus, and presents the strategies employed to optimize squeezing under realistic laboratory conditions.

3.1 Generation of Twin Beams

In our lab, twin beams are generated through a process called FWM, which is a nonlinear interaction of four fields with a medium in which two photons are absorbed to generate two new photons. In our experiment, two photons of the same frequency, ω_{p}, called pump photons, interact with an atomic medium (a cell containing ^{85}Rb atoms) in a double-Λ configuration (Fig. 3.1(a)), to simultaneously generate two new photons called probe and conjugate at frequencies ω_{pr} and ω_{c}, respectively. Conservation of energy defines the frequency relation between the four fields such that $\omega_{\mathrm{p}}+\omega_{\mathrm{p}} = \omega_{\mathrm{pr}}+\omega_{\mathrm{c}}$.

If we do not have an input field (seed) for the FWM at the probe or conjugate frequencies to stimulate the process, the photon pairs will be generated spontaneously,

which leads to vacuum two-mode squeezed states. On the other hand, if we seed the FWM with either or both of these frequencies, photon pairs (at the frequencies of the probe and conjugate) will be generated from stimulated emission, producing bright two-mode squeezed states (bTMSS). Although both processes yield the same amount of squeezing, the bTMSS are displaced in phase space so that each beam has a mean number of photons significantly larger than 1. The presence of a strong optical field allows the quantum correlations to be measured as fluctuations around a large classical amplitude, enabling the use of standard photodetection techniques with higher signal-to-noise ratios. As a result, these states are considerably easier to manipulate and detect in practical experiments compared to vacuum two-mode squeezed states.

Figure 3.1(b) shows the simplified experimental setup for the FWM process. Orthogonally polarized seed probe and pump beams co-propagate through the rubidium vapor cell at a small crossing angle. Their interaction with the Rb atoms drives the FWM process, resulting in the generation of bright probe and conjugate beams that emerge along distinct propagation directions. This non-collinear geometry is chosen to satisfy the phase-matching condition, which ensures that the interacting optical fields remain phase coherent throughout the medium, allowing the generated fields to build up efficiently. To maximize the amount of squeezing, several parameters need to be optimized, such as the density of Rb atoms (which depends on the temperature of the vapor cell), the interaction volume (which depends on the sizes of the probe and pump beams and length of the vapor cell), single photon detuning (Δ), optical power of the pump beam, two photon detuning (δ), angle between seed and pump beams, etc.

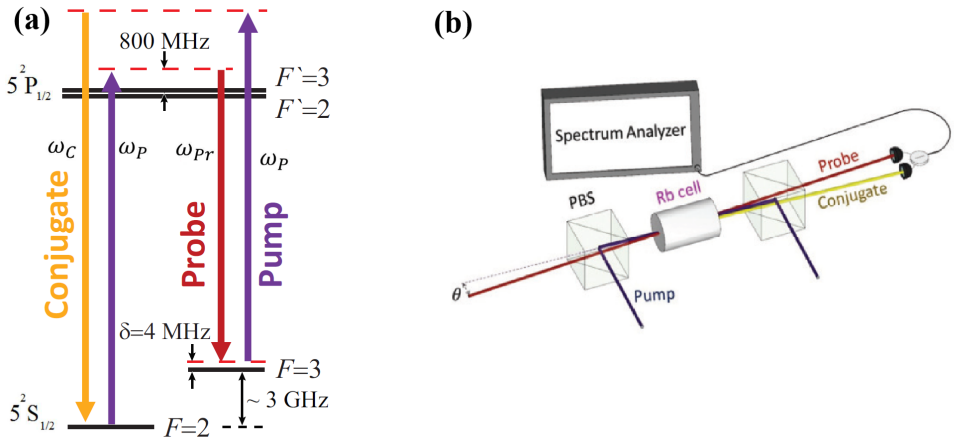


Figure 3.1: (a) FWM in a double-Λ configuration in Rb atoms: two pump photons (at frequency ω_p) and one seed photon at the probe frequency (ω_{pr}) result in pair photon emission at the probe and the conjugate (ω_c) frequencies. The frequency of the probe photons is red-detuned from the pump by ∼ 3 GHz, which is the energy separation between the two hyperfine structure (F=2 and F=3) ground states of the $5\,^2S_{1/2}$ energy level. (b) Simplified experimental setup for the FWM process. Orthogonally polarized probe and pump interact at the center of a Rb vapor cell and as a result a conjugate beam is generated. Intensities of probe and conjugate are measured with photodetectors and the difference photocurrent between the generated photocurrents is sent to a spectrum analyser to measure the intensity difference noise.

For an efficient FWM process, the frequency difference between the pump and the probe needs to be close to the separation between the two ground state hyperfine levels of ^{85}Rb , such that the pump and probe are on two-photon resonance ($\delta = 0$). This condition ensures coherent Raman coupling between the two ground hyperfine states, allowing a long-lived atomic coherence to build up and efficiently drive the four-wave mixing process. While in principle the optimum FWM process should occur at $\delta = 0$, a slight detuning is needed to compensate for the light shift introduced by the strong pump beam coupling the D1 $F = 3$ to F' transition of ^{85}Rb [38].

3.2 Noise Measurements

The probe and conjugate are measured using photodetectors that generate a photocurrent proportional to the optical intensity. The noise is characterized using an intensity-difference method (balanced detection), in which the photocurrents from the two detectors are subtracted to suppress common-mode noise and reveal quantum correlations. The resulting difference signal is then analyzed using a spectrum analyzer to determine the noise power as a function of frequency. This method can be used to determine the level of squeezing for the bTMSS or the SNL for a coherent state of light. To measure the twin beam noise, probe and conjugate beams are incident on photodetectors and the resulting photocurrents are subtracted, which cancels out the quantum correlated portions of the photocurrents to result in noise levels below the SNL. Similarly, to measure the SNL, a coherent state of light is divided into two

equal parts, with the help of beam splitter, and sent to photodetectors for balanced detection. The resulting photocurrents are classically correlated as the beam splitter sends common classical noises to both output beams and their subtraction results in the SNL. The ratio of twin beam noise to the SQL gives the level of squeezing [5, 6].

In general, both the probe and conjugate beams (modes a and b, respectively) can be seeded, so that the state of the field after the FWM process is of the form:

$$|\alpha, \beta, \xi\rangle = \hat{S}_{ab}(\xi)\hat{D}_a(\alpha)\hat{D}_b(\beta)|0, 0\rangle, \tag{3.1}$$

where $\hat{S}_{ab}(\xi)$ is the squeezing operator, $\hat{D}_a(\alpha)$ is the displacement operator, α and β are the displacement introduced by the displacement operator, and $\hat{a}$, $\hat{a}^\dagger$, $\hat{b}$ and $\hat{b}^\dagger$ are the corresponding creation and annihilation operators for the different modes.

For our experiments, we only seed the process with the probe field a with an amplitude α ($|\alpha|^2 \gg 1$), such that the field can be treated as a large classical amplitude with small quantum fluctuations. In this limit, the mean photon number is dominated by the coherent amplitude, and higher-order fluctuation terms can be neglected. As a result, the mean values of the output probe and conjugate beams can be written as

$$\begin{aligned} \langle \hat{n}_a \rangle &= |\alpha|^2 \cosh^2 s = |\alpha|^2 G, \\ \langle \hat{n}_b \rangle &= |\alpha|^2 \sinh^2 s = |\alpha|^2 (G-1), \end{aligned} \tag{3.2}$$

where G, defined as $\cosh^2 s$, is the gain of FWM process which quantifies the amplification of the seed probe beam after the nonlinear interaction. The noise or the variance

of the fields can be shown to be

$$\begin{aligned} \langle(\Delta\hat{n}_a)^2\rangle &= |\alpha|^2 G(2G-1), \\ \langle(\Delta\hat{n}_b)^2\rangle &= |\alpha|^2 (G-1)(2G-1). \end{aligned} \tag{3.3}$$

We can also find the noise of the difference signal $\langle[\Delta(\hat{n}_a - \hat{n}_b)]^2\rangle = \langle(\Delta\hat{n}_a)^2\rangle + \langle(\Delta\hat{n}_b)^2\rangle - 2(\langle\hat{n}_a\hat{n}_b\rangle - \langle\hat{n}_a\rangle\langle\hat{n}_b\rangle)$, to be

$$\langle[\Delta(\hat{n}_a - \hat{n}_b)]^2\rangle = |\alpha|^2, \tag{3.4}$$

which shows that the noise of the difference signal after the FWM process is the same as the noise of the input seed field $\hat{a}$. This is because the FWM generates photon pairs having identical noise properties in the ideal case, which when subtracted cancel and only the noise from the input seed is left [5, 34].

The noise of the output fields, from the FWM, can be compared with the SNL for the same total power as the twin beams by taking their ratio, i.e.

$$R_{\mathrm{FWM}} = \frac{\langle[\Delta(\hat{n}_a - \hat{n}_b)]^2\rangle_{\text{squeezed state}}}{\langle[\Delta(\hat{n}_a - \hat{n}_b)]^2\rangle_{\text{coherent state}}} = \frac{\langle[\Delta(\hat{n}_a - \hat{n}_b)]^2\rangle}{\langle\hat{n}_a\rangle + \langle\hat{n}_b\rangle} = \frac{1}{2G-1}. \tag{3.5}$$

We say that there is intensity difference squeezing if $R_{\mathrm{FWM}} < 1$ as the noise of the difference falls below the SNL expected for two independent coherent beams with the same total optical power. Figure 3.2 gives an example of the measured squeezing in twin beams, which is shown from our work. For this particular example, a maximum intensity-difference squeezing of 7.2 dB was obtained at a measurement frequency of 500 kHz for a cell temperature of 99 °C. The corresponding experimental parameters included a pump beam power of 135 mW with a Gaussian spatial profile and a waist

diameter of 0.6 mm, a probe beam with a Gaussian profile and a waist diameter of 0.6 mm, and a crossing angle of 0.4° between the pump and probe beams.

3.3 Effect of losses on squeezing

In an ideal intensity-difference measurement, the probe and conjugate photons generated by FWM are produced in pairs, so their correlated fluctuations cancel in the difference photocurrent and the noise is reduced below the SNL, as discussed in Sec. 3.2. In practice, optical losses and finite detector quantum efficiency degrade these correlations by coupling vacuum fluctuations into the detected modes. This section summarizes how loss modifies the observed intensity difference squeezing and shows why balancing the two detection channels is crucial for obtaining the best noise reduction [37, 39].

Optical loss in each arm can be modeled using a beam splitter with intensity transmission η, with the unused port injecting a vacuum mode. For the probe and conjugate modes (a and b), the transformations are

$$\hat{a} \rightarrow \sqrt{\eta_{\mathrm{pr}}}\,\hat{a} + \sqrt{1-\eta_{\mathrm{pr}}}\,\hat{a}_v, \tag{3.6}$$

$$\hat{b} \rightarrow \sqrt{\eta_{\mathrm{c}}}\,\hat{b} + \sqrt{1-\eta_{\mathrm{c}}}\,\hat{b}_v, \tag{3.7}$$

where η_{pr} and η_{c} represent the total transmissions in the probe and conjugate paths, respectively, including propagation losses, optical element losses, and photodiode quantum efficiency.

When the probe is seeded with a large coherent amplitude α ($|\alpha|^2 \gg 1$), the

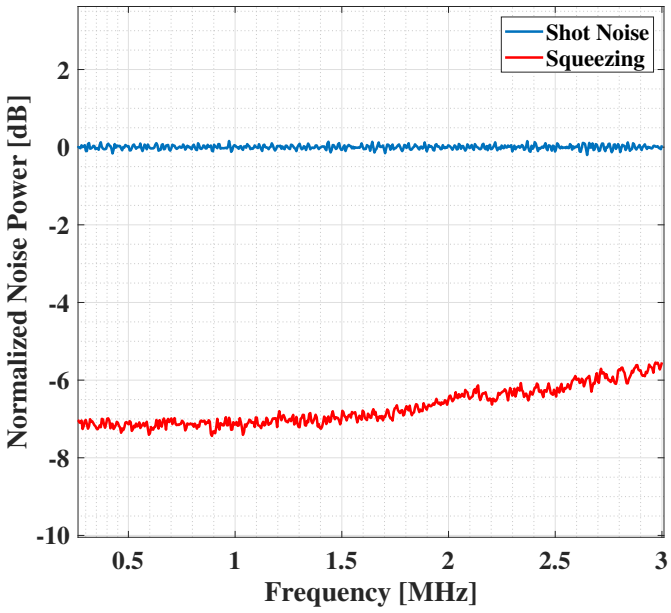


Figure 3.2: Intensity-difference squeezing spectrum: Normalized noise trace for the intensity difference from twin beams for a cell temperature of 99 °C, *pump beam with 135 mW of power (0.6 mm diameter) interacting at an angle of* 0.4° *with the probe beam (0.6 mm diameter). Red trace represents the normalized squeezing and the blue trace represents the shot noise. A maximum of 7.2 dB of squeezing is observed for the 500 kHz to 1MHz frequency region.*

squeezing parameter is s and the FWM gain is defined as

$$G \equiv \cosh^2(s). \tag{3.8}$$

In the absence of loss, the normalized intensity difference noise is

$$R_0 \equiv R_{\mathrm{FWM}} = \frac{\langle[\Delta(\hat{n}_a - \hat{n}_b)]^2\rangle}{\langle\hat{n}_a\rangle + \langle\hat{n}_b\rangle} = \frac{1}{2G-1}, \tag{3.9}$$

as derived in Sec. 3.2.

To include loss, we evaluate the variance of the intensity difference signal after applying the loss transformations in Eq. (3.7). Writing each field operator as a mean value plus a small fluctuation, $\hat{a} = \alpha + \delta\hat{a}$ and $\hat{b} = \beta + \delta\hat{b}$, the photocurrent fluctuations are linearized in $\delta\hat{a}$ and $\delta\hat{b}$. The noise of the difference signal after loss is then

$$\langle[\Delta(\hat{n}_a^{(\mathrm{loss})} - \hat{n}_b^{(\mathrm{loss})})]^2\rangle, \tag{3.10}$$

As in the loss-free case, the measured noise is normalized to the shot-noise limit corresponding to the same detected optical power. The SNL variance scales with the sum of the detected mean photon numbers,

$$\langle[\Delta(\hat{n}_a - \hat{n}_b)]^2\rangle_{\mathrm{SNL}} = \langle\hat{n}_a^{(\mathrm{loss})}\rangle + \langle\hat{n}_b^{(\mathrm{loss})}\rangle. \tag{3.11}$$

For seeded FWM, the mean photon numbers after loss are

$$\langle\hat{n}_a^{(\mathrm{loss})}\rangle = |\alpha|^2\eta_{\mathrm{pr}}\cosh^2(s), \qquad \langle\hat{n}_b^{(\mathrm{loss})}\rangle = |\alpha|^2\eta_{\mathrm{c}}\sinh^2(s), \tag{3.12}$$

so that the SNL normalization is proportional to

$$\eta_{\mathrm{pr}}\cosh^2(s) + \eta_{\mathrm{c}}\sinh^2(s). \tag{3.13}$$

Including loss in both arms, the normalized intensity-difference noise can therefore be written as

$$R_{\text{loss}} = \frac{\langle[\Delta(\hat{n}_a^{(\text{loss})} - \hat{n}_b^{(\text{loss})})]^2\rangle}{\langle\hat{n}_a^{(\text{loss})}\rangle + \langle\hat{n}_b^{(\text{loss})}\rangle} = 1 + \frac{2\eta_c^2 \sinh^4(s) + 2\sinh^2(s)\cosh^2(s)\left(\eta_{\text{pr}}^2 - 2\eta_{\text{pr}}\eta_c\right)}{\eta_{\text{pr}}\cosh^2(s) + \eta_c \sinh^2(s)}. \tag{3.14}$$

Equation (3.14) shows that optical loss reduces the effective quantum correlations and that imbalance between η_{pr} and η_c can prevent efficient noise cancellation.

In the limit of *balanced* loss, $\eta_{\text{pr}} = \eta_c \equiv \eta$, the normalized noise reduces to a simple mixture of the ideal squeezed noise and vacuum noise:

$$R_{\text{balanced loss}} = \eta R_0 + (1 - \eta). \tag{3.15}$$

The first term represents transmission of the initial squeezed state through the lossy channels, while the second term corresponds to vacuum noise coupled in by the loss. Thus, even for strong initial squeezing, any non-unity transmission sets a limit on the observable squeezing at the detectors.

3.4 Shot-Noise Limit Calibration

A reliable measurement of quantum noise reduction requires an accurate calibration of the SNL, which serves as the reference noise level for a coherent state with the same optical power. In practice, this calibration is essential for quantifying the degree of squeezing produced by the FWM process [37, 39]. To ensure an accurate comparison between the SNL and the twin-beam noise, several experimental conditions must be carefully matched. First, the optical power at the detectors during SNL calibration is

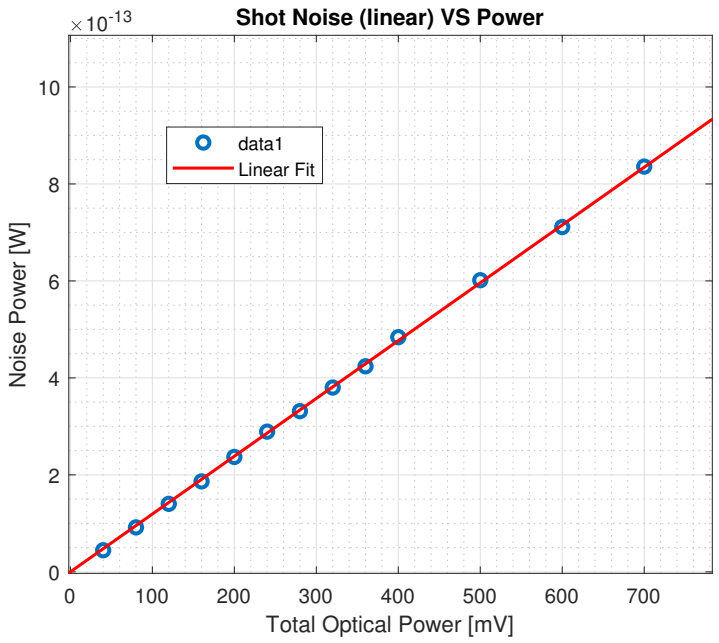


Figure 3.3: Sample data for calibrating the SNL: A linear behavior of the noise power vs. total optical power indicates that the measurement is shot-noise limited.

adjusted to equal the total power of the probe and conjugate beams combined. Second, the detection electronics are operated in a regime where electronic noise is well below the optical shot noise across the frequency range of interest. Finally, all the classical technical noise is canceled by the balanced detection is verified by confirming that the measured noise scales linearly with optical power to make sure that all classical noise is properly canceled out.

When the measured noise scales linearly with optical power, as shown in Fig. 3.3, the detection system is shot-noise limited and the shot-noise level can be accurately determined. In contrast, a quadratic dependence of noise on optical power indicates the presence of residual classical noise, preventing a reliable measurement of the shot-noise

limit. Once the SNL is established, the level of squeezing is quantified by normalizing the measured intensity-difference noise of the twin beams to this reference. Noise levels below the SNL indicate the presence of quantum correlations generated by the FWM process. This calibration procedure provides a robust and reproducible method for characterizing squeezing and is used consistently throughout this dissertation.

3.5 Spatial and Momentum Correlations in Twin Beams

In addition to correlations in photon number, twin beams generated via FWM exhibit strong spatial quantum correlations. These correlations originate from the conservation of momentum during the nonlinear interaction and play a central role in applications such as quantum imaging and spatially resolved metrology [35, 40].

At a fundamental level, the FWM process must satisfy both energy and momentum conservation. While energy conservation enforces the frequency relation $2\omega_{\mathrm{p}} = \omega_{\mathrm{pr}} + \omega_{\mathrm{c}}$, momentum conservation requires

$$2\mathbf{k}_{\mathrm{p}} = \mathbf{k}_{\mathrm{pr}} + \mathbf{k}_{\mathrm{c}}, \tag{3.16}$$

where $\mathbf{k}_{\mathrm{p}}$, $\mathbf{k}_{\mathrm{pr}}$, and $\mathbf{k}_{\mathrm{c}}$ are the wave vectors of the pump, probe, and conjugate fields, respectively. This phase-matching condition determines the spatial emission directions of the generated probe and conjugate beams [31, 40].

At a more detailed level, the phase-matching condition must account for the dispersive response of the atomic medium. In a dispersive medium, where the refractive index depends on the frequency of the propagating light, the wave vector of each optical field

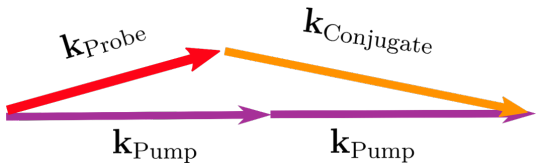


Figure 3.4: Phase-matching condition in FWM setup in a dispersive medium. Probe wave-vector (red) is at an angle to the pump wave-vector (maroon). Conjugate wave-vector is represented by yellow arrow.

is modified by the refractive index according to $\mathbf{k} = n(\omega)\omega/c$. During the four-wave mixing process in hot rubidium vapor, the dispersive contribution of the pump field can be neglected due to optical pumping, which effectively populates a single ground hyperfine state. Similarly, the conjugate field is far detuned from atomic resonances and therefore experiences negligible dispersion. By contrast, the probe field is near-resonant and acquires a refractive-index contribution.

As a result, the effective phase-matching condition is modified by the refractive index of the probe field, and perfect collinear momentum matching is generally no longer satisfied. In the non-collinear geometry used in hot rubidium vapor, shown in Fig. 3.4, the probe is injected at a small angle with respect to the pump, and the conjugate is generated symmetrically on the opposite side of the pump axis. The phase-matching condition is satisfied over a continuous range of transverse wave vectors, rather than a single direction. This gives rise to a broad angular bandwidth of the FWM process and underlies the inherently multi-spatial-mode nature of the generated twin beams. The extent of this angular bandwidth is set by the phase-matching tolerance of the

nonlinear interaction, which is determined by factors such as the dispersive properties of the medium, the interaction length, and the spatial profile of the pump beam.

Because photon pairs are generated simultaneously and must satisfy the phase-matching condition, photon number fluctuations at a given transverse wave vector in the probe beam are correlated with fluctuations of the corresponding transverse wave vector in the conjugate beam.

The spatial correlations generated through phase matching can be examined in different optical planes, leading to different properties in the near-field and far-field regimes. These regimes are discussed in detail below.

3.5.1 Near-Field and Far-Field Correlations

Spatial quantum correlations in twin beams can be analyzed either in the near field or in the far field of the nonlinear medium, corresponding to measurements in position space or transverse momentum space, respectively. The distinction between these two regimes provides complementary insight into the spatial structure of the correlations generated by the FWM process [37, 40].

In the near field, which corresponds to an image plane of the vapor cell, correlations appear between matching transverse positions in the probe and conjugate beams, as shown in Fig. 3.5 (b) where, as a representation, a circled region in the probe beam cross section is correlated to the similarly positioned circled region in the conjugate beam cross section. This behavior reflects the fact that photon pairs are generated at the same physical location within the interaction volume. Consequently, spatial

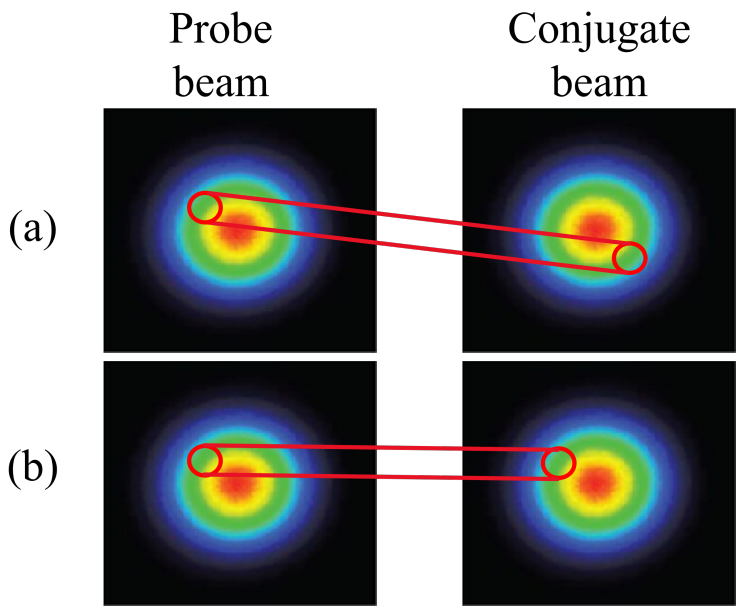


Figure 3.5: Distribution of correlated regions in (a) far field and (b) near field. The circled region on the left side (probe beam cross section) is correlated with the circled region on the right side (conjugate beam cross section).

measurement of photons in a localized region of the probe beam are correlated with fluctuations measured in the corresponding region of the conjugate beam.

In contrast, the far field corresponds to the Fourier plane of the optical system, where spatial information is represented in terms of transverse wave vectors. In this regime, momentum conservation governs the correlations, such that fluctuations for a transverse wave vector $\mathbf{k}_\perp$ in the probe beam are correlated with fluctuations for $-\mathbf{k}_\perp$ in the conjugate beam. These far-field correlations arise directly from the phase-matching condition of the four-wave mixing process and reflect the conservation of momentum during photon-pair generation. Figure. 3.5 (a) represents diagonally opposite correlated

regions, represented as circles, in the probe and conjugate beam cross sections.

3.5.2 Multi-Spatial-Mode Properties of Twin Beams

Defining characteristics of twin beams generated via FWM in hot atomic vapor include high gain, the absence of an optical cavity around the vapor cell, and their intrinsically multi-spatial-mode nature. Unlike cavity-based squeezing sources, where mode selection often restricts the output to a small number of transverse modes, the FWM process supports a continuum of spatial modes determined by the phase-matching bandwidth and the geometry of the interaction [34, 35].

Each correlated pair of spatial modes can be treated as an independent two-mode squeezed state. As a result, quantum noise reduction can be observed simultaneously across many spatial channels. The number of accessible spatial modes depends on several experimental parameters, including the pump beam size, interaction length, atomic density, and detuning. A larger pump beam increases the number of supported spatial modes by enlarging the transverse interaction area. A larger pump will have less k-vectors and thus a smaller range of correlated wave-vector pairs. A broader phase-matching permits correlations over a larger range of transverse wave vectors. In contrast, tight focusing reduces the effective interaction length. Stronger dispersion further tightens the phase-matching condition by narrowing the allowable wave-vector range. By controlling these parameters, the spatial structure of the twin beams can be tailored to suit specific experimental goals.

Having established the generation, noise properties, and spatial structure of twin

beams produced via FWM, the following chapter shifts focus from the source itself to its application in quantum-enhanced measurements. In particular, we examine how the quantum correlations inherent in two-mode squeezed states can be exploited to improve measurement sensitivity beyond classical limits in practical sensing scenarios.

Chapter 4

Quantum Sensing with Squeezed States of Light

Quantum sensing seeks to exploit nonclassical properties of quantum states to improve the precision with which physical parameters can be estimated. For optical based sensing, the sensitivity of classical schemes based on coherent states of light is fundamentally limited by the shot-noise limit, which arises from the Poissonian statistics of photon detection. Squeezed states of light offer a well-established pathway to surpass this limit by redistributing quantum noise between conjugate observables, enabling reduced measurement uncertainty for appropriately chosen detection schemes [5, 9].

Among the various classes of nonclassical states, two-mode squeezed states, or twin beams, are particularly well suited for sensing applications. The strong quantum correlations shared between the probe and conjugate beams enable noise reduction in differential measurements, making twin beams robust against common classical technical noise sources. These properties have been successfully leveraged in a wide range of sensing scenarios, including interferometry, absorption measurements, and imaging-based schemes [35, 41].

A quantum enhanced sensor has three main components: a quantum resource state (such as quantum states of light), a sensing device, and a detection system, as shown schematically in Fig. 4.1. We use twin beams of light as our quantum resource state. The sensing device is any element that transduces a physical parameter of interest into a measurable modification of the probing optical field, such as a change in intensity,

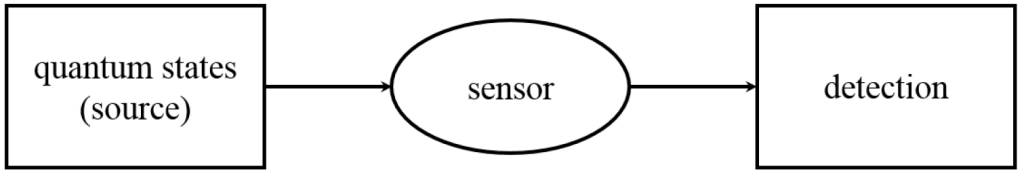


Figure 4.1: Components of a quantum enhanced sensing configuration: a source of quantum states, a sensing device, and a detection system. Enhancement in detection is possible when sensing device and detection scheme are already operating at their ultimate classical limit.

phase, frequency, or polarization.

Resonance sensors, which exhibit a strong optical response at the probing wavelength, provide a particularly effective implementation of such transduction. They operate by exhibiting a sharp optical response at specific wavelengths, such that small perturbations to the system produce measurable shifts in resonance frequency. This response makes resonant structures particularly sensitive transducers for converting physical parameters into optical signals. The final component is a detection system that reads out the signal encoded in our probing light by the sensing device. For our experiments, this is accomplished by using intensity-difference noise measurements.

From a practical perspective, the performance of a quantum sensor is determined not only by the degree of squeezing available at the source, but also by how efficiently quantum correlations are preserved throughout the entire measurement chain. Optical losses, finite detector efficiency, and environmental perturbations can all degrade the

achievable quantum advantage. This sensitivity to loss is particularly pronounced for squeezed states, where optical loss introduces uncorrelated vacuum noise that degrades the quantum correlations between the two modes. As discussed in the previous chapters, optical losses can reduce the observable level of squeezing, underscoring the importance of minimizing loss throughout the sensing system. As a result, quantum sensing must be approached as a system-level problem, where the source, sensing element, and detection strategy are jointly optimized to maximize sensitivity under realistic experimental conditions [42, 43].

In this chapter, we introduce the general framework used throughout this dissertation to implement quantum-enhanced sensing with squeezed states of light. Rather than focusing on a single sensing platform, the discussion emphasizes the common principles that govern sensitivity enhancement and the role of quantum correlations in suppressing measurement uncertainty. These concepts provide the foundation for the specific implementations presented in later chapters, where twin beams are applied to fiber-optic and plasmonic sensors to demonstrate quantum-enhanced performance in real life applications.

4.1 Measurement Sensitivity

The goal of any sensing system is to estimate a physical parameter with the highest possible precision. We define sensitivity as the minimum resolvable change of a parameter from the background noise. In optical sensing, this parameter may correspond to a

change in intensity, phase, frequency, or polarization of the light induced by interaction with a the sensor. The sensitivity of such measurements is fundamentally constrained by noise associated with the probing field and the detection process.

For classical optical measurements employing coherent states of light, the fundamental noise source is shot noise, which arises from the quantized nature of photodetection. Shot noise leads to root-mean-square fluctuations in the detected photon number that scale as the square root of the mean photon number, setting the SNL for measurement sensitivity. As a result, improving sensitivity within a classical framework typically requires increasing optical power or improving the sensor itself, which may be impractical or undesirable in many sensing applications due to power constraints, sample damage, or nonlinear effects.

In practice, additional technical noise sources, such as laser intensity noise, electronic noise, and environmental fluctuations, can further degrade sensitivity. While many of these contributions can be mitigated through differential or balanced detection techniques, the SNL represents a fundamental limit that cannot be surpassed using classical states of light alone. Quantum states of light provide a route to surpass the SNL by modifying the statistical properties of the optical field [5, 39].

For an intensity-based measurement, the signal-to-noise ratio (SNR) can be expressed as

$$\mathrm{SNR} = \frac{\langle \Delta I_{\mathrm{sig}} \rangle}{\sqrt{\langle (\Delta I)^2 \rangle}}, \tag{4.1}$$

where $\langle I_{\mathrm{sig}} \rangle$ represents the mean signal induced by a change in the parameter being measured, and $\sqrt{\langle (\Delta I)^2 \rangle}$ denotes the root-mean-square (RMS) uncertainty of the

measured intensity. Quantum enhancement is achieved when this RMS noise is reduced below the corresponding value obtained when probing with a coherent state of equal optical power as the quantum state.

Twin-beam sensing schemes are inherently robust against many technical noise sources, including laser intensity noise and electronic fluctuations, provided these contributions are common between the two detection channels. This robustness, combined with the ability to achieve sub-shot-noise performance, makes twin beams particularly attractive for sensing scenarios in which environmental noise or system instabilities are unavoidable [35, 37, 43].

4.2 Quantum-Enhanced Sensing using Twin Beams

Twin-beam sensing exploits the correlated nature of two-mode squeezed states by comparing the response of two optical modes subjected to different interactions. By performing differential detection, common-mode noise shared by the two beams is suppressed, while changes induced by the signal of interest are retained. If the signal affects only one beam, or affects the two beams in different ways, such as producing unequal magnitudes or opposite-sign responses, the differential measurement remains sensitive to the signal. In contrast, signals that couple identically to both beams are rejected along with common-mode noise.

To illustrate this concept more concretely, consider a differential sensing scheme in which a small external perturbation induces a change in the detected intensity of the

probe beam, δI_{probe}, and a corresponding change δI_{conj} in the conjugate beam. The detected intensities can be written as

$$I_{\text{probe}} = \bar{I}_{\text{probe}} + \delta I_{\text{probe}} + \Delta I_{\text{probe}}, \tag{4.2}$$

$$I_{\text{conj}} = \bar{I}_{\text{conj}} + \delta I_{\text{conj}} + \Delta I_{\text{conj}}, \tag{4.3}$$

where $\bar{I}$ denotes the mean detected intensity, δI represents the signal induced by a change in the parameter being measured, and ΔI represents intensity fluctuations about the mean due to noise. The differential signal measured at the output of the detector is defined as

$$\Delta I = I_{\text{probe}} - I_{\text{conj}}. \tag{4.4}$$

Substituting the expressions above yields

$$\Delta I = (\bar{I}_{\text{probe}} - \bar{I}_{\text{conj}}) + (\delta I_{\text{probe}} - \delta I_{\text{conj}}) + (\Delta I_{\text{probe}} - \Delta I_{\text{conj}}). \tag{4.5}$$

In practice, the mean intensities can be balanced such that $\bar{I}_{\text{probe}} \approx \bar{I}_{\text{conj}}$, leaving the differential signal primarily sensitive to the signal-induced and noise contributions. The mean differential signal associated with the perturbation is therefore

$$\langle \Delta I_{\text{sig}} \rangle = \langle \delta I_{\text{probe}} - \delta I_{\text{conj}} \rangle. \tag{4.6}$$

The noise of the differential measurement is characterized by the variance of the differential intensity,

$$\langle (\Delta I)^2 \rangle = \left\langle (\Delta I_{\text{probe}} - \Delta I_{\text{conj}})^2 \right\rangle, \tag{4.7}$$

such that $\sqrt{\langle (\Delta I)^2 \rangle}$ represents the root-mean-square (RMS) uncertainty of the differential signal.

Using the same definition of signal-to-noise ratio introduced earlier, the SNR for the differential measurement can be written as

$$\mathrm{SNR}_{\mathrm{diff}} = \frac{\langle \Delta I_{\mathrm{sig}} \rangle}{\sqrt{\langle (\Delta I)^2 \rangle}} = \frac{\langle \delta I_{\mathrm{probe}} - \delta I_{\mathrm{conj}} \rangle}{\sqrt{\langle (\Delta I)^2 \rangle}}. \tag{4.8}$$

For classical probing with coherent states, the variance $\langle (\Delta I)^2 \rangle$ is limited by shot noise and scales with the total detected optical power. In contrast, when twin beams are used, quantum correlations between the probe and conjugate beams reduce the differential intensity variance below the SNL. As a result, the differential SNR is enhanced relative to the coherent-state case for the same detected optical power, providing a clear signature of quantum-enhanced sensing.

4.3 Quantum Fisher Information and Fundamental Sensitivity Limits

An approach to determine the fundamental limits of quantum-enhanced sensing is provided by the concept of Quantum Fisher Information (QFI), which quantifies how a quantum state changed due to the change of the parameter of interest. Intuitively, the QFI measures how strongly a small change in the parameter θ modifies the quantum state, and therefore how much information about θ is encoded in the state itself. A larger QFI implies that even a small variation in the parameter produces a more distinguishable change in the quantum state, enabling a more precise estimation.

More formally, the QFI is defined in terms of the statistical distinguishability between nearby quantum states $\hat{\rho}(\theta)$ and $\hat{\rho}(\theta + d\theta)$, and can be calculated from the

symmetric logarithmic derivative associated with the state [44, 45]. Importantly, the QFI depends only on the quantum state and the way in which the parameter is encoded, and not on any particular measurement or detection strategy. This is important because it establishes the QFI as a fundamental upper bound on the precision achievable in estimating the parameter, independent of the specific measurement scheme employed. As such, it provides a way to assess the ultimate sensitivity of a given quantum state and to identify the optimal measurement strategy that would be required to reach this bound.

For a parameter θ encoded in a quantum state $\hat{\rho}(\theta)$, the quantum Cramér–Rao bound (QCRB) sets a fundamental lower bound on the variance of any unbiased estimator,

$$\mathrm{Var}(\theta) \geq \frac{1}{QFI}. \tag{4.9}$$

This bound represents the ultimate precision limit achievable with the given quantum state, regardless of the specific measurement performed. While different detection schemes may extract the information with varying efficiency, no measurement can surpass the limit imposed by the QFI. Consequently, increasing the QFI directly corresponds to increasing the maximum amount of information that can be extracted about the parameter θ, and therefore to an improvement in the fundamental sensitivity limit.

In the sensing schemes studied here, the signal is ultimately read out through intensity-based measurements. For squeezed states of light, the QFI is therefore directly linked to the variance of the measured intensity. In particular, reducing the quantum

fluctuations in intensity, such as through intensity-difference squeezing between twin beams, allows smaller parameter-induced changes in the optical field to be resolved more clearly [46, 47]. As a result, the suppression of intensity noise provided by squeezing and two-mode correlations leads to an increase in the QFI and an improvement in the fundamental sensitivity limit.

In the later chapters of this dissertation, these concepts are applied to specific sensing platforms. In particular, for plasmonic sensors where the parameter of interest is encoded in a spectral or polarization-dependent optical response, sensitivity enhancement is achieved using two-mode squeezed states. By optimizing parameters such as nanohole geometry, the QFI associated with the measurement can be maximized.

Having established the central concepts of quantum enhanced sensing using two-mode squeezed light, including the role of intensity difference detection, noise suppression below the SNL, and the connection to fundamental sensitivity limits through tools such as the QFI, the next step is to address the practical requirements for implementing these ideas in deployable sensing systems. In the following chapter, we therefore move from the sensing framework to the experimental engineering of the quantum resource itself, and describe the development of a compact, narrowband, fiber-coupled twin-beam source based on FWM in hot rubidium vapor. Then, the later chapters show how the twin beams are used to enhance the sensitivity of fiber Bragg grating sensors and plasmonic nanostructure sensors under realistic experimental constraints.

Chapter 5

Compact Fiber-Coupled Twin-Beam Source

5.1 Introduction and Motivation

The generation of squeezed states of light has played a central role in advancing quantum optics and quantum metrology. In particular, two-mode squeezed states (twin beams) provide strong quantum correlations that can be exploited to reduce measurement noise below the SNL. While such states have been studied extensively in laboratory environments, a major challenge remains in translating these sources into compact and robust systems that can be deployed in real-world applications. Bridging this gap requires moving beyond large, table-top experiments toward stable, fiber-coupled squeezed-light sources with a small footprint and reduced system complexity [5, 9, 10]. This chapter describes the development of such a compact source based on FWM in hot rubidium vapor, designed with low-SWaP (size, weight, and power) considerations in mind.

Early demonstrations of FWM-generated squeezing in hot atomic vapors established it as an accessible and powerful method for producing bright twin beams [6, 34]. Compared to nonlinear crystals, atomic vapors offer advantages such as narrowband emission naturally matched to atomic transitions, high nonlinear gain, and the ability to generate strong correlations without the need for optical cavities [6, 34, 37]. These features make FWM particularly appealing for applications in quantum-enhanced sensing,

quantum communication, and quantum imaging. However, traditional implementations of FWM-based squeezed-light sources have generally relied on large free-space optical layouts that require careful alignment, making them unsuitable for practical deployment. For squeezed light to move from laboratory demonstrations to field-ready devices, the sources must be made compact, robust, and compatible with fiber delivery.

The motivation for compact fiber-coupled sources extends across both fundamental and applied domains. On the fundamental side, robust sources enable more reliable experiments in quantum optics, including studies of entanglement distribution, quantum repeaters, and hybrid quantum systems. On the applied side, fiber-coupled squeezed light can be directly integrated into sensor networks, communication links, and interferometric systems, where fiber delivery is often essential and offer a quantum advantage.

A compact and narrowband source also plays a critical role in advancing quantum sensing platforms, particularly in atomic systems where the narrowband nature of the source enables efficient interaction with well-defined atomic transitions. Such compatibility is essential in applications where long-term stability and environmental robustness are required. In many sensing applications there are technical constraints such as power, size and weight that must be carefully managed. A fiber-coupled squeezed-light source built on a compact optical breadboard minimizes these issues, while also reducing the alignment burden on operators. The low-SWaP design directly addresses the need for systems that can be scaled, transported, and integrated without sacrificing performance.

This chapter presents the design and characterization of such a compact, fiber-

coupled source of two-mode squeezed light at 795 nm, generated through FWM in a ^{85}Rb vapor cell. We describe the design choices made to reduce system complexity, the experimental methods for optimizing fiber coupling, and the procedures for benchmarking noise performance relative to the SNL. Finally, we report results showing more than 4 dB of squeezing after fiber delivery, representing a significant step toward deployable quantum-enhanced sensing platforms [48].

5.2 Design Goals and Low-SWaP Considerations

The development of a compact, narrowband, fiber-coupled source of two-mode squeezed light was motivated by the need to transition quantum optics experiments from the laboratory into real-world applications. While bulk FWM setups in rubidium vapor cells have demonstrated strong levels of squeezing in free-space configurations [34, 35], these systems are typically large and difficult to integrate with existing optical platforms that could directly benefit from fiber optic delivery of squeezed light. For quantum-enhanced sensing to become deployable, it is necessary to engineer sources that are compact, robust, and compatible with fiber delivery while still maintaining appreciable levels of squeezing. These requirements fall under the broader low-SWaP (size, weight, and power) design, which guides the development of photonic technologies intended for field use.

The design goals for this system were defined by several key considerations. First, the footprint of the apparatus had to be reduced without sacrificing optical access to

the rubidium vapor cell or the ability to control beam sizes and focusing conditions. A compact geometry not only eases integration but also reduces long-term stability issues associated with mechanical drift. Unlike free-space systems, where alignment tolerances can be actively monitored, a deployable system could benefit from passive stability and efficient coupling over extended time scales. Secondly, the optical power budget was a critical design factor. While higher pump powers can in principle generate stronger squeezing, they also introduce unwanted effects such as excess spontaneous emission and Kerr effect that degrade the level of squeezing. The Kerr effect causes the refractive index of the medium to depend on the intensity and affects the spatial profile of the beams [31, 38].

Low-SWaP design also requires careful consideration of thermal and mechanical constraints. Rubidium vapor cells must be heated to achieve sufficient atomic density for efficient nonlinear interaction. The cell was housed in a compact oven with temperature control, while surrounding optics were arranged in a minimized geometry that avoided long beam paths. Optical mounts and fiber couplers were selected for both their compactness and robustness.

The schematic in Fig. 5.1 illustrates the overall design. Both the pump and the seed probe beams are fiber-delivered using polarization-maintaining fibers, ensuring stable input polarization. Inside the vapor cell, the pump and probe intersect at a small angle at the center of the cell, establishing the phase-matching geometry required for efficient FWM. As a result of the nonlinear interaction, the probe beam is amplified and a conjugate beam is generated on the opposite side of the pump.

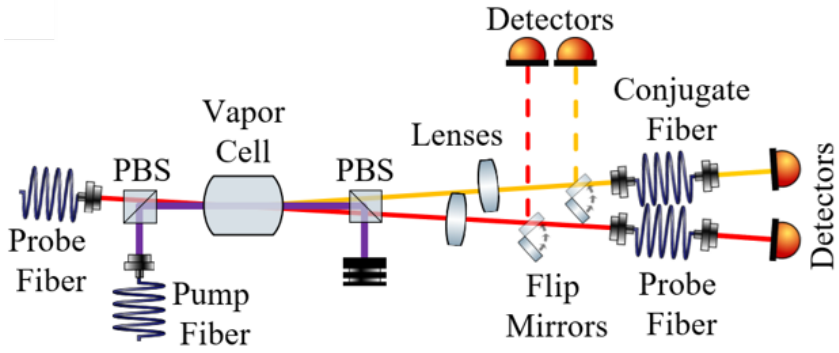


Figure 5.1: Schematic of compact experimental setup for generating fiber-coupled twin beams through a FWM process in a hot ^{85}Rb vapor cell. The pump and seed probe beams are delivered via polarization-maintaining fibers and overlap at the center of the vapor cell to establish the phase-matching geometry. The nonlinear interaction amplifies the probe and simultaneously generates the conjugate beam on the opposite side of the pump. After the cell, the probe and conjugate are coupled back to polarization maintaining fibers using f–to-f optical systems. Flip mirrors allow switching between direct free-space detection and fiber-coupled detection, enabling comparison of squeezing performance before and after fiber delivery. Reprinted with permission from [48].

To transition back to fiber delivery, each of the output beams is collected using a pair of lenses and steering mirrors that form an f–to-f imaging system onto fiber couplers. This arrangement preferentially couple momentum-correlated spatial modes (coherence areas) of the probe and conjugate to the fibers. This minimizes coupling of uncorrelated spatial modes, which would otherwise add excess thermal noise and reduce squeezing. In the default measurement configuration, the probe and conjugate are directly fiber-coupled to balanced detectors to characterize the intensity difference squeezing at the output of the fiber. As a reference measurement or diagnostic check, mirrors can be flipped into the beam paths to bypass the fibers, allowing direct free-space detection of the twin beams. This dual configuration provides flexibility in comparing performance with and without fiber coupling and ensures that losses and degradation of squeezing introduced by the fiber coupling process are well quantified [48].

As can be seen from the schematic the compact design integrates fiber delivery on both the input and output sides, while maintaining a minimal free-space interaction region confined to the rubidium vapor cell. This design reduces alignment sensitivity, facilitates long-term stability, and achieves the primary goal of creating a low-SWaP source of squeezed light that is fully compatible with fiber-based systems.

5.3 Fiber Coupled Squeezing Optimization

A key challenge in coupling twin beams into optical fibers lies not only in matching their spatial profiles to the fiber mode but also in addressing the multimode nature of

the fields generated by FWM. The phase-matching condition,

$$\vec{k}_{\text{pump}} + \vec{k}_{\text{pump}} = \vec{k}_{\text{probe}} + \vec{k}_{\text{conjugate}}, \tag{5.1}$$

ensures momentum conservation in the FWM process as shown in the Fig. 5.2. In the far field, however, this condition does not imply a strict point-to-point correlation between probe and conjugate photons. Because the pump beam has a finite transverse size, its angular spectrum contains a spread of $\vec{k}$-vectors, leading to correlations between one probe mode and a distribution of conjugate modes. In the spatial domain, this manifests as multiple correlated subregions across the transverse beam profiles, referred to as coherence areas [35, 49].

The existence of multiple coherence areas means that twin beams are inherently multimode. Because the FWM process supports multiple spatial coherence areas, the generated probe and conjugate fields are inherently multimode, consisting of many independent pairs of two-mode squeezed spatial modes. When coupling into single-mode fibers, imperfect spatial mode matching leads to the collection of uncorrelated modes in addition to the correlated ones. These uncorrelated modes retain the intrinsic thermal statistics of each beam and, once projected onto the same fiber mode, contribute excess noise that does not cancel in the intensity difference, thereby degrading the observed squeezing.

In other words, if uncorrelated regions are coupled into single-mode fibers, they contribute excess thermal noise, degrading the observed squeezing. Thus, efficient fiber coupling requires more than maximizing transmission, it requires selecting conditions

where predominantly correlated modes are captured. Prior studies have shown that the number and size of coherence areas depend strongly on the pump beam size, with smaller pumps producing fewer and larger coherence areas in the far field [49, 50]. This provides a strategy to stimulate close to a single coherence area in the probe and conjugate beams.

In our design, the pump and probe beams were adjusted to have equal $1/e^2$ waist diameters of approximately 0.6 mm at the center of a 12-mm-long isotopically pure ^{85}Rb vapor cell. By matching the pump and probe beam sizes and tightly focusing them to comparable waist diameters at the center of the vapor cell, the FWM interaction is constrained to a reduced transverse area, which increases the spatial coherence area and limits the total number of supported spatial modes. In a seeded FWM process, the input probe preferentially stimulates emission into the spatial modes that overlap with the seed, producing bright, strongly correlated probe–conjugate mode pairs within this region. Other spatial modes allowed by phase matching but lacking overlap with the seed grow only from spontaneous emission and remain weak. By reducing the number of supported modes and enhancing the dominance of the seeded region, this geometry effectively concentrates the probe–conjugate correlations into a single dominant coherence area, improving spatial mode purity and facilitating efficient fiber coupling with reduced excess noise. As a result, most of the bright portion of the probe beam becomes close to a single coherence area correlated with the bright portion of the conjugate beam.

Once the spatial correlations were optimized in this way, conventional mode matching

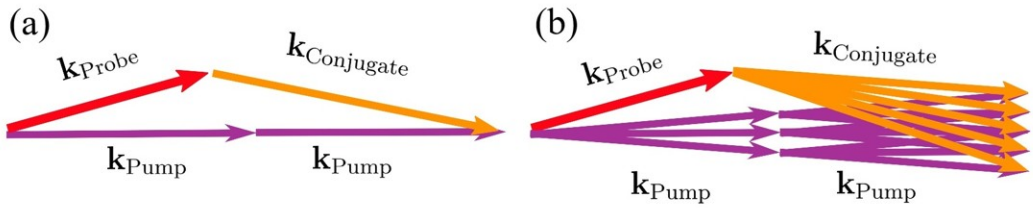


Figure 5.2: Illustration of momentum correlations imposed by the phase-matching condition in four-wave mixing. (a) For an idealized pump with infinite transverse extent, the $\vec{k}$-vectors of the probe and conjugate are correlated one-to-one in momentum space. (b) For a finite pump size, the spread of $\vec{k}$-vectors of the pump leads to correlations between probe $\vec{k}$-vectors and multiple conjugate $\vec{k}$-vectors, producing multiple coherence areas in the far field. Reprinted with permission from [48].

into the fiber became the primary consideration in realizing maximum fiber coupling efficiency for both probe and conjugate beams. After the FWM process, the amplified probe and conjugate beams were collected with two separate f–to–f imaging systems. The probe arm employed a 100 mm focal length lens, while the conjugate arm used a 125 mm lens. The strong pump induces a cross-Kerr nonlinearity in the vapor, producing an intensity-dependent refractive index experienced by the probe and conjugate fields [31]. Because the probe frequency lies significantly closer to the atomic resonance than the conjugate, it experiences a stronger cross-Kerr lensing effect. This results in a greater modification of the probe's wavefront curvature and effective beam waist compared to the conjugate. Different focal lengths in the probe and conjugate arms are therefore required to compensate for these unequal nonlinear distortions and to achieve

matched spatial modes at the fiber inputs. Typical coupling efficiencies exceeded 90% for both probe and conjugate beams.

In summary, fiber coupling of twin beams requires careful management of both spatial correlations and mode matching. The reduced and equal pump and probe beam waists ensures that the majority of light coupled into the polarization-maintaining fibers originated from correlated regions, thus minimizing the excess noise and preserving strong squeezing in the fiber-coupled configuration.

5.4 Experimental Setup

The compact source was constructed on a small optical breadboard with a footprint of 12 inches $\times$ 12 inches, designed to minimize size while maintaining sufficient flexibility for alignment and diagnostics. Figure 5.3 shows a photograph of the experimental setup. The optical layout closely follows the schematic shown in the previous subsection, but here the physical implementation highlights the degree of compactness achieved in a reduced footprint.

The light source for the experiment was a Ti:Sapphire laser operating near the D_1 line of ^{85}Rb at 795 nm. A fraction of the output was frequency shifted by 3.04 GHz using a double-pass AOM to generate the seed probe beam. This frequency shift established the two-photon detuning required for the FWM process. Both the strong pump and the weak seed probe were coupled into PM fibers and delivered to the breadboard which improved the long-term stability of the input beams.

On the breadboard, the pump and probe beams were collimated after their fibers and directed into a 12-mm-long glass vapor cell containing isotopically enriched ^{85}Rb. The vapor cell was housed in a compact oven with temperature control and operated at approximately 99°C, providing sufficient atomic density for an efficient nonlinear interaction. At the cell, the pump and probe overlapped at a small angle of about 0.4°, satisfying the phase-matching condition and had equal waists of ~ 600 μm ($1/e^2$ diameter). With a pump power of approximately 135 mW, this configuration yielded strong parametric gain and measurable squeezing. This pump power is significantly lower than typically used, which is needed for a low SWaP system.

After the FWM process, the amplified probe and the newly generated conjugate beam exited the cell on opposite sides of the pump. Each beam was collected using an f–to–f imaging system and coupled into PM fibers with typical coupling efficiencies exceeding 90%. Then the fiber-coupled probe and conjugate were directed to the balanced detectors to measure the squeezing. Flip mirrors allowed the beams to be redirected to free-space detectors, enabling direct measurement of squeezing for comparison. For calibration, the squeezed-light measurements were compared to the shot-noise level obtained by splitting a coherent beam of the same total power onto the detectors.

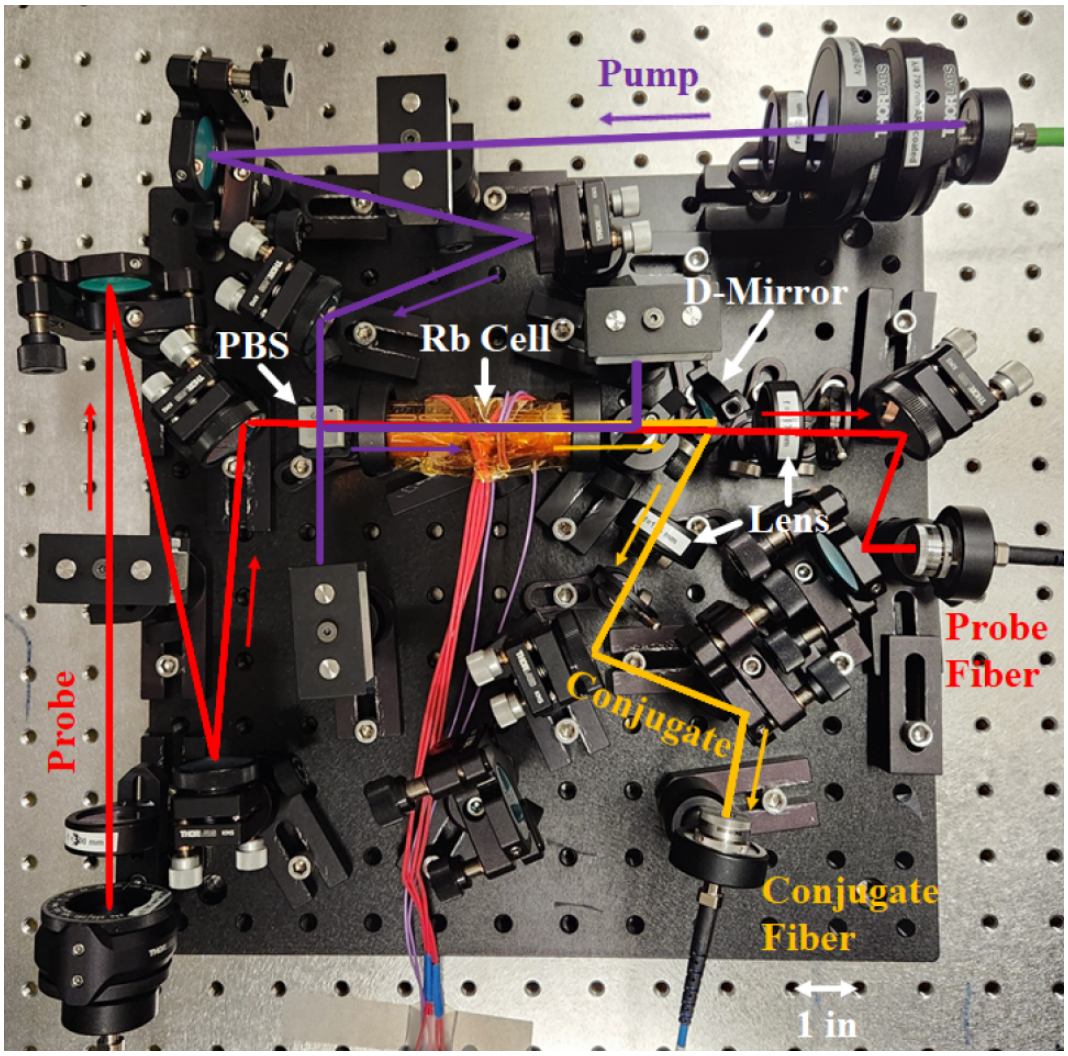


Figure 5.3: Photograph of the compact experimental setup for generating fiber-coupled twin beams via four-wave mixing in a hot ^{85}Rb vapor cell. The pump and probe beams are delivered through polarization-maintaining fibers, collimated and overlapped at the center of the vapor cell housed in a temperature-controlled oven. After the nonlinear interaction, the amplified probe and conjugate are collected with f–to-f imaging systems (focal lengths 100 mm probe arm, 125 mm conjugate arm) and coupled back into PM fibers with $> 90\%$ efficiency. Reprinted with permission from [48].

5.5 Results and Conclusions

Figure 5.4 shows the measured intensity–difference noise of the twin beams, normalized to the SNL (blue trace at 0 dB). To understand the impact of fiber coupling, we compare the squeezing measured before the output fibers (bypassing them with flip mirrors) to the squeezing measured after the fibers.

When we bypass the output fibers, the yellow trace in Fig. 5.4 shows an intensity–difference squeezing of approximately -7.2 dB in the lower frequency region, with the level gradually rolling off at higher analysis frequencies due to the narrowband response of the FWM process and the detector bandwidth. This measurement characterizes the quantum correlations produced directly by the source. With both probe and conjugate coupled into their respective single-mode PM fibers at 90% efficiency each, we obtain a maximum of -4.4 dB of squeezing at an analysis frequency of 1 MHz (red trace).

For reference, the green trace in Fig. 5.4 shows the *expected* squeezing if the 10% fiber-coupling inefficiency were due *only* to optical loss. In the simple loss model, a variance V_0 (watts) transforms as

$$V_{\text{loss}} = \eta\, V_0 + (1 - \eta), \tag{5.2}$$

with η is the overall transmission; the corresponding value of the noise level in dB is $S_{\text{dB}} = 10 \log_{10} V_{\text{loss}}$. Using the measured value of V_0 to be 0.19 mW corresponding to -7.2 dB and $\eta = 0.90$ for both beams, the predicted level at 1 MHz is about 0.234 mW or -6.3 dB (green trace). The fact that the measured post-fiber value is 0.363 mW or

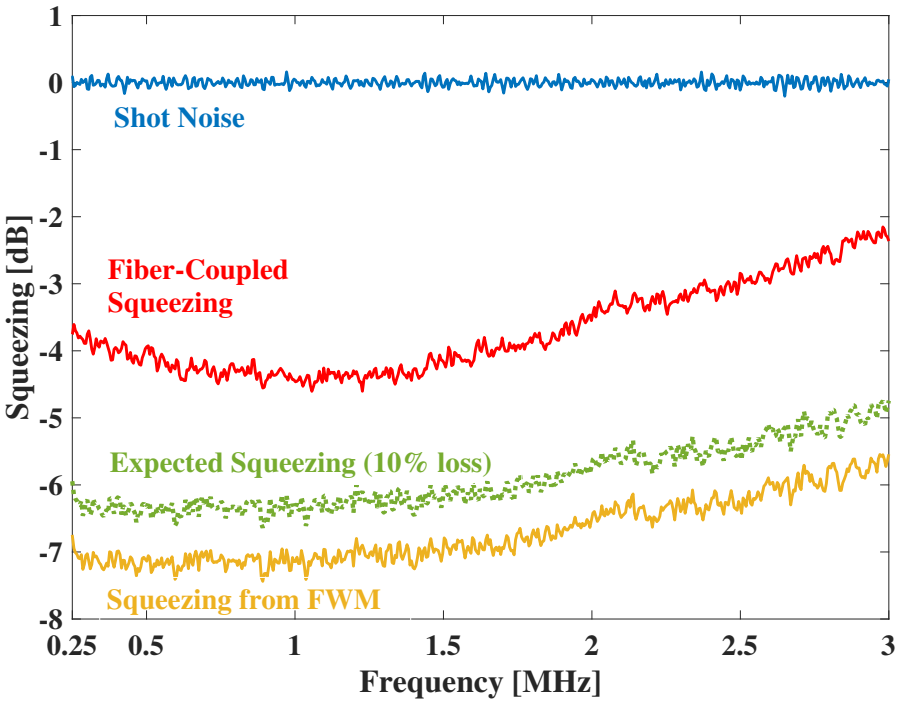


Figure 5.4: Intensity–difference noise normalized to the SNL (blue, 0 dB): squeezing before the output fibers (yellow, ≈ −7.2 dB), squeezing at the output *of the fibers (red, −4.4 dB at 1 MHz), and the* expected *squeezing for a simple 10% pure-loss model (green, ≈ −6.3 dB at 1 MHz). Experimental conditions: pump power 135 mW, pump–probe crossing angle* 0.4°*, 12 mm* ^{85}*Rb cell. Reprinted with permission from [48].*

−4.4 dB indicates that imperfect spatial mode matching couples a small fraction of *uncorrelated* (thermal-statistics) spatial modes along with the correlated bright modes into the fibers, which raises the noise floor beyond what pure optical loss would produce.

To account for the additional degradation beyond pure optical loss, we model imperfect fiber coupling as an effective beamsplitter that mixes the ideal squeezed fields with noise entering through the unused port. In addition to vacuum fluctuations

associated with ordinary loss, imperfect spatial mode matching causes a fraction of uncorrelated spatial modes—each exhibiting thermal photon-number statistics—to be coupled into the single-mode fiber. Once projected onto the fundamental fiber mode, these uncorrelated modes become indistinguishable from the correlated modes and contribute excess noise that does not cancel in the intensity difference measurement.

Following Ref. [51], the measured variance after fiber coupling can be written as

$$V' = \eta V_0 + (1-\eta)\left[\epsilon V_{\mathrm{th}} + (1-\epsilon)V_{\mathrm{vac}}\right], \tag{5.3}$$

where V_0 is the initial squeezing of the twin beams, η is the fiber coupling efficiency (assumed equal for probe and conjugate), $V_{\mathrm{vac}} = 1$ represents vacuum noise normalized to the shot-noise limit, and $V_{\mathrm{th}} > 1$ denotes the normalized thermal noise associated with uncorrelated spatial modes. The parameter ϵ represents the fraction of the uncoupled power that contributes thermal noise, with $\epsilon = 0$ corresponding to pure optical loss and $\epsilon = 1$ corresponding to coupling of only uncorrelated thermal modes.

Using $\eta = 0.9$, an initial squeezing level of -7.2 dB, and assuming comparable contributions from vacuum and thermal noise ($\epsilon \approx 0.5$), the predicted squeezing level is approximately -3.2 dB, in reasonable agreement with the observed reduction. While this simplified model overestimates the contribution of uncorrelated modes, it captures the essential mechanism by which imperfect spatial mode matching converts multimode structure into excess thermal noise, thereby limiting the achievable squeezing after fiber coupling.

Two effects are particularly relevant here: (i) residual mismatch of the fiber-mode

profile to the far-field bright mode of each beam, and (ii) a slight mismatch of the effective imaging planes for probe and conjugate (the desired plane is the Fourier plane of the cell center), both of which are complicated by the cross-Kerr-induced wavefront reshaping of the probe as it is closer to resonance.

Both effects impact the fidelity with which correlated spatial modes are selected during fiber coupling. Residual mismatch between the fiber mode and the far-field bright mode causes the fiber to collect a superposition of correlated and uncorrelated spatial modes rather than a single coherence area, allowing thermal-statistics fluctuations from uncorrelated regions to enter the detected signal. Similarly, imperfect matching of the effective imaging planes for the probe and conjugate results in the collection of spatial modes that are not momentum-matched. In both cases, the resulting projection of uncorrelated modes onto the same fiber mode introduces excess noise that does not cancel in the intensity-difference measurement.

Overall, the compact, fiber-coupled source delivers $\sim$4.4 dB of intensity–difference squeezing *at the outputs of the fibers* at 1 MHz while operating with $\sim$135 mW of pump power and a small (0.4°) pump–probe angle. This performance, achieved on a 12×12 inches breadboard with AR-coated *input* fiber facets and $> 90\%$ coupling, demonstrates that spatial-mode optimization (equal pump/seed waists, far-field coupling, and f–to-f relays) can preserve strong quantum correlations in a low-SWaP, fiber-deliverable configuration.

Chapter 6

Quantum-Enhanced Fiber Sensing

6.1 Introduction and Motivation

Fiber-optic sensors have emerged as one of the most versatile and robust platforms for precision metrology over the past several decades. Among the various different types of sensors, *fiber Bragg gratings* (FBGs) have attracted widespread attention because their intrinsically wavelength-encoded response provides absolute, drift-resistant measurements, while their compatibility with telecommunication components, multiplexing capability, and robustness in harsh environments make them more practical and scalable than many other fiber-optic sensing approaches [52, 53]. The basic idea is that a periodic modulation of the refractive index within an optical fiber reflects a narrow band range of wavelengths, centered around the Bragg wavelength. Any external perturbation of the FBG due to strain, pressure, or temperature modifies the grating period and hence the Bragg wavelength and the effective index of the guided mode, leading to a measurable spectral shift [54]. This intrinsic link between environmental perturbations and optical response has positioned FBGs as indispensable tools for structural health monitoring, aerospace systems, oil and gas infrastructure, and biomedical applications [55, 56].

From a sensing perspective, the appeal of FBGs lies in their multiplexing capability, compact size, and immunity to electromagnetic interference. Large arrays of gratings can

be inscribed along a single fiber, enabling distributed monitoring across tens of kilometers with millimeter-scale resolution [57]. In addition, their reflective geometry allows simple integration into optical networks without requiring complex inline couplers or free-space optics. For these reasons, FBGs have become a mature commercial technology for classical sensing, routinely used in oil pipeline leak detection, aircraft wing load monitoring, bridge strain mapping, and real-time seismic measurements [58, 59].

However, for classically probed sensors, like FBG sensors, their sensitivity remains fundamentally limited by photon shot noise. In classical interrogation schemes, whether using tunable lasers, interferometric demodulation, or phase-generated carrier techniques, the smallest detectable wavelength or strain is ultimately limited by shot noise and, for measurement observables that depend linearly on the measurand, scales as $1/\sqrt{N}$, where N is the number of detected photons [39, 29]. As a result, further improvements in interrogation electronics or laser stability cannot indefinitely overcome this quantum noise floor. This realization has motivated interest in incorporating nonclassical states of light into FBG interrogation systems, where the reduced quantum fluctuations of squeezed states can lower the effective noise below the SNL.

In this thesis, we pursue the integration of fiber Bragg grating sensors with *two-mode squeezed light generated from FWM in rubidium vapor*. The motivation for using twin beams rather than single-mode squeezed light is twofold. First, twin beams enable balanced intensity-difference detection, which naturally cancels common-mode technical noise, thereby improving robustness against classical background fluctuations such as laser power drifts [37, 42]. Second, the use of twin beams beams enables a

differential sensing architecture in which two identical FBG sensors experiencing the same environmental perturbations produce similar response in both gratings, while any localized disturbance closer to one FBG results in a differential strain response. The underlying quantum correlations allow common background noise to be strongly suppressed in the intensity-difference measurement, enhancing sensitivity to weak localized signals such as those associated with pipeline leaks [56].

The specific application motivation of this work lies in leak detection for oil and gas pipelines. Current monitoring technologies are often limited by latency (slow pressure-drop methods), low spatial resolution (acoustic monitoring), or susceptibility to false alarms. FBG-based systems, on the other hand, are robust and passive devices that detect small strain-induced wavelength shifts with sub-nanometer precision. By embedding quantum-enhanced interrogation into this framework, our approach seeks to demonstrate a new class of quantum-enhanced fiber sensors that enhances the sensitivity of a perturbation signal through noise floor reduction below the SNL.

In this chapter we investigate how fiber Bragg gratings can serve as a practical platform for quantum-enhanced sensing. We begin by characterizing FBGs designed to operate at 795 nm, making them directly compatible with our rubidium-based squeezed light source. We then describe an interrogation scheme that takes advantage of the correlations in the twin beams and balanced detection to suppress noise. The system is first tested with coherent light in order to establish a classical baseline and to validate our analysis methods. These results set the stage for future demonstrations of squeezing-enhanced sensitivity once technical challenges with stable squeezed-light

delivery are addressed.

6.2 FBG Working Principle

Figure 6.1 shows an FBG, which consists of a short section of optical fiber with a periodic refractive-index variation that acts as a distributed mirror that reflects specific wavelengths of light while transmitting others. When broadband light propagates through the fiber, constructive interference occurs only for the wavelength that satisfies the Bragg condition, while all other wavelengths are transmitted through the grating, as shown in Fig. 6.1.

The resonance wavelength, known as the Bragg wavelength, is determined by

$$\lambda_B = 2n_{\text{eff}}\Lambda, \tag{6.1}$$

where n_{eff} is the effective refractive index of the fiber core, and Λ is the grating period, i.e., the spacing between adjacent refractive-index planes. Light satisfying this condition experiences coherent back-reflection along the fiber, producing a narrow reflection peak centered at λ_B, as shown in Fig. 6.2. The bandwidth of this reflection peak depends on the grating length and the modulation depth of the refractive index.

Any variation in either n_{eff} or Λ alters the Bragg wavelength (Fig. 6.3), leading to a measurable shift in the reflected spectrum. This response forms the basis for FBG-based sensing, where external perturbations such as strain or temperature modify the grating properties [52, 53, 54]. The fractional wavelength shift can be expressed as

$$\frac{\Delta\lambda_B}{\lambda_B} = (1 - p_e)\varepsilon + (\alpha + \xi)\Delta T, \tag{6.2}$$

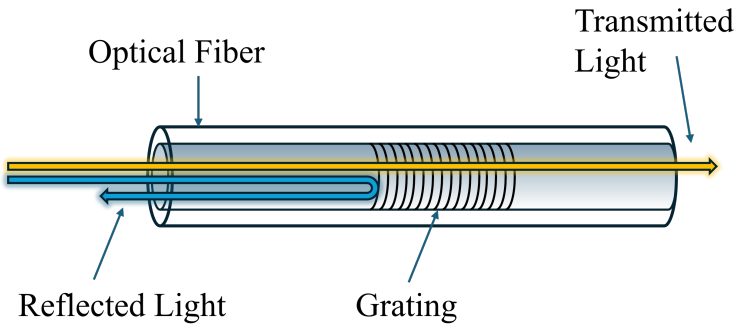


Figure 6.1: Schematic of an FBG: An FBG consists of a short section of optical fiber with a periodic refractive-index variation in its core effectively acting as a diffraction grating. This grating makes certain wavelengths reflect back and others transmit depending on the grating separation. Here blue arrow represents reflected light and the yellow arrow represents transmitted light.

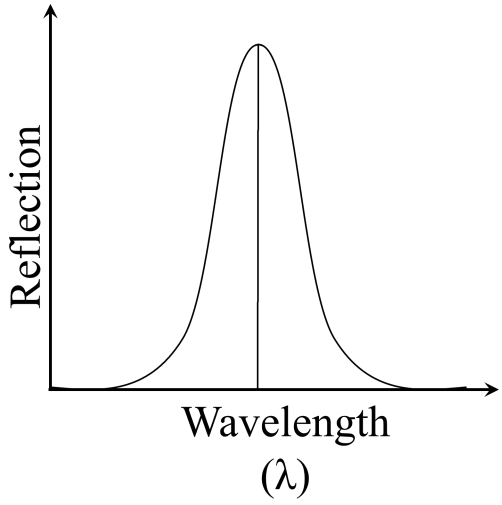


Figure 6.2: Reflection response of an FBG sensor. The central wavelength is called Bragg wavelength.

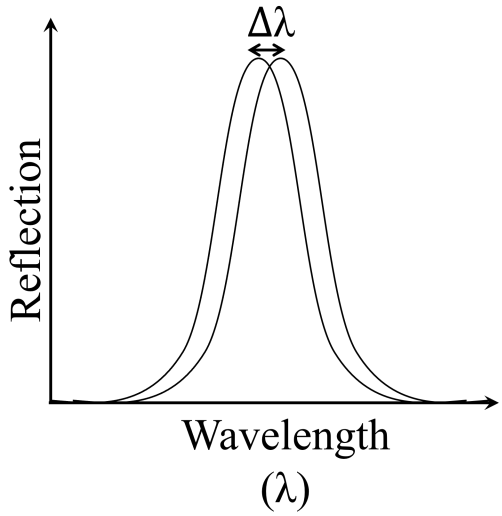


Figure 6.3: Operational principle of FBG sensor: Wavelength shift in FBG response due to a strain or temperature variation: Any perturbations in the temperature or strain causes a shift in effective Bragg wavelength. If the perturbation is periodic, the whole reflection spectrum shifts back and forth periodically.

where ε is the applied strain, ΔT is the temperature change, p_e is the effective photoelastic constant, α is the thermal expansion coefficient of the fiber, and ξ is the thermo-optic coefficient describing the temperature dependence of the refractive index [53].

When an FBG is put under a tensile strain, the grating period increases while the effective refractive index decreases due to the photoelastic effect; although these contributions act in opposite directions, the change in grating period dominates, resulting in a net redshift of the Bragg wavelength. Conversely, compressive strain or cooling causes a blueshift. The linear and repeatable wavelength dependence enables FBGs to

serve as precise and multiplexable sensing elements for applications such as structural health monitoring, vibration detection, and oil or gas pipeline leak diagnostics [56, 57, 59].

6.3 FBG Characterization

Most commercially available FBGs are designed for operation in the telecommunication bands near 1310 nm or 1550 nm, where silica fibers exhibit minimal loss and diode lasers are widely available. However, our source of quantum light is based on the rubidium D_1 transition at 795 nm, which required custom-designed gratings centered near this wavelength. For this work, we had FBGs fabricated in single-mode PM optical fibers using the UV phase-mask inscription technique [53], in which interference fringes generated by a diffracted UV beam through a silica phase mask produce a periodic refractive-index modulation in the photosensitive fiber core. This technique provides excellent reproducibility and accurate control of the Bragg wavelength by selecting an appropriate phase-mask period. Each grating was designed to have a nominal Bragg wavelength of 795 nm, a reflectivity of approximately 98%, and a bandwidth of about 0.3–0.4 nm.

The reflection and transmission spectra of the 795 nm FBGs were characterized to verify their optical response and temperature-tuning behavior. A small portion of the laser beam at 795 nm was coupled into the fiber containing the FBG, and the laser wavelength was scanned across the 795 nm range using a tunable Ti:Sapphire source.

The reflected optical power was monitored with a photodiode and normalized to the summation of total reflected and transmitted power.

Temperature tuning was performed by mounting the FBG on a thermoelectric cooler (TEC) in good thermal contact with the fiber. The temperature was varied between 20°C and 60°C in steps of 20°C while monitoring the reflected spectrum. The measured reflection spectra are shown in Fig. 6.4, where the reflection peaks shift systematically toward longer wavelengths as the temperature increases. This behavior arises from both the thermo-optic effect, which increases the refractive index of the fiber core, and the thermal expansion of the grating period.

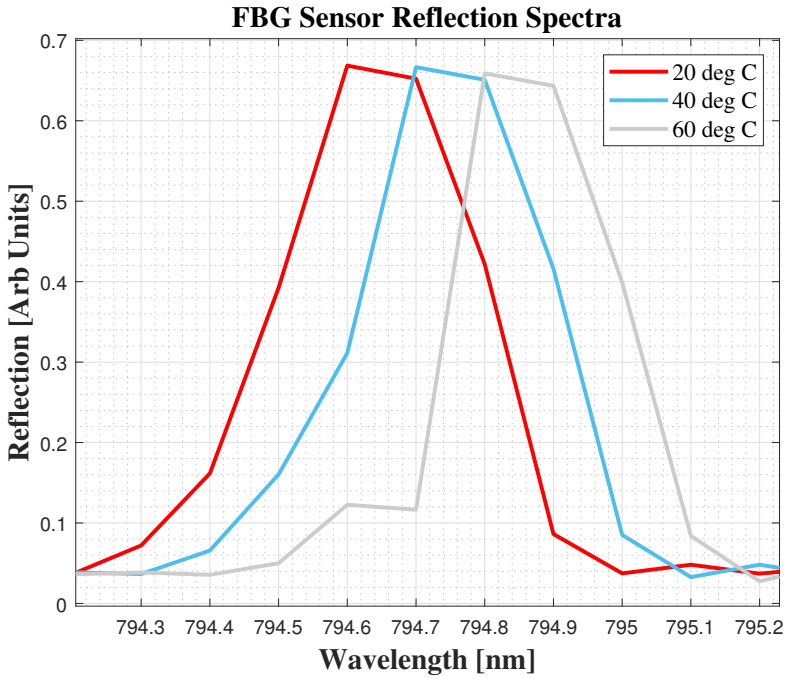


Figure 6.4: Measured reflection spectra of the 795 nm fiber Bragg grating for three different temperatures: 20° C (red), 40° C (blue), and 60° C (gray). The Bragg wavelength shifts to longer wavelengths as the temperature increases due to the combined thermo-optic and thermal expansion effects.

This characterization is essential for two reasons. First, the thermal tunability of the FBG enables precise alignment of the Bragg resonance with the wavelengths of the probe and conjugate beams generated with the four-wave mixing process in rubidium vapor. By tuning the FBG reflection peak to overlap with the twinbeam wavelengths, one can optimize the reflection efficiency which is critical for maintaining the largest possible squeezing level after the gratings. Second, tuning the FBG such that the operating point lies on the slope of the reflection curve maximizes the system's strain-to-intensity

transduction efficiency. Small shifts in the Bragg wavelength, induced by mechanical vibration or acoustic perturbations, translate into measurable intensity modulations in the reflected signal. This slope-based interrogation enhances the sensitivity of the measurement without requiring large modulation amplitudes.

The steepness of the reflection spectrum of the FBGs plays a crucial role in determining both the transduction slope and the achievable signal-to-noise ratio. However, there exists a trade-off: operating at the steepest slope improves sensitivity but can introduce additional optical losses that degrade the squeezing. Consequently, the gratings were tuned to an intermediate point that provided a good balance between signal strength and squeezing retention.

In addition to the temperature characterization, the polarization dependence of the FBG response was also examined. Polarization maintaining fibers were chosen for the FBGs so as to separate the back reflected light through the FBGs from the incident light which is discussed later in the experimental schematic part. Because the gratings are written in polarization-maintaining (PM) fibers, the effective refractive indices experienced by light polarized along its fast and slow axes are slightly different. To quantify this effect, we measured the reflection spectra for two orthogonal input polarization states, one aligned along the fast axis and the other along the slow axis of the fiber. This measurement helps determine how polarization alignment can influence the FBG resonance and provides an additional degree of control for fine-tuning the sensor response if needed.

Figure 6.5 shows the measured reflection spectra for the two polarization states. The

blue trace corresponds to the same polarization used in the temperature characterization at 40 °C, while the orange trace represents the orthogonal polarization. A clear wavelength shift is observed between the two, with the orthogonal polarization exhibiting a lower Bragg wavelength. This behavior is consistent with the birefringence of the PM fiber, where light polarized along the fast axis experiences a slightly lower effective refractive index compared to the slow axis.

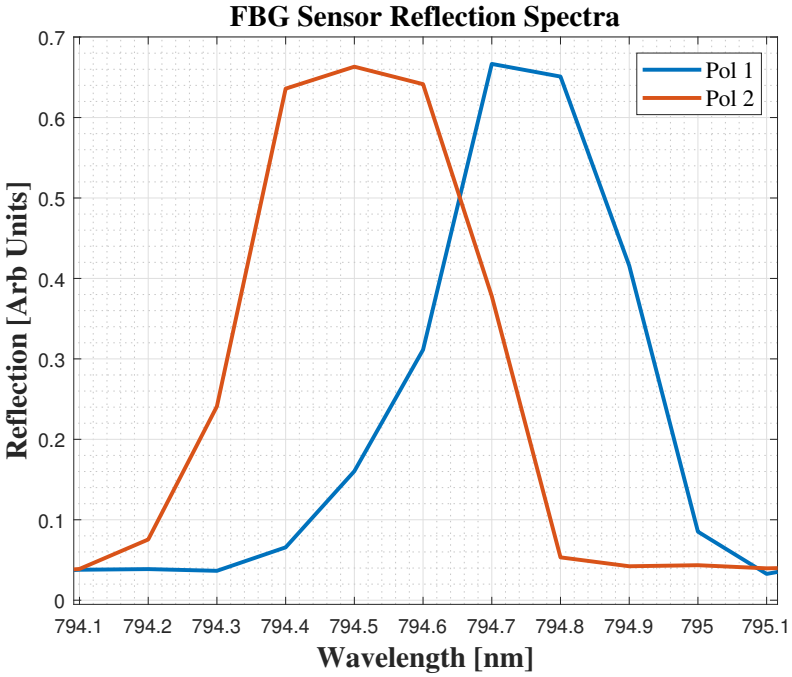


Figure 6.5: Measured reflection spectra of the 795 nm fiber Bragg grating for two orthogonal input polarization states: The blue trace corresponds to the reference polarization at 40 °C, while the orange trace represents the orthogonal polarization. The latter shows a slight shift toward shorter wavelength due to the lower effective refractive index experienced by the fast-axis polarization of the PM fiber.

In summary, the FBGs used in this work were custom-fabricated and characterized for operation at 795 nm to match the rubidium-based twin-beam source. They exhibit narrow reflection bandwidths, high reflectivity (99%), and predictable thermal tuning behavior, providing a robust and tunable sensing element for quantum-enhanced fiber sensing.

6.4 Experimental Scheme and Detection

One of the principal challenges in using quantum-enhanced sensing techniques in real-world measurements is the presence of environmental and technical noise, which can obscure quantum noise reduction and limit achievable sensitivity. Fluctuations arising from laser power drifts, acoustic vibrations, and thermal variations often dominate over quantum noise in practical settings, thereby eroding the advantage provided by nonclassical states of light. Consequently, the practical deployment of quantum sensing technologies requires strategies that not only reduce fundamental quantum noise but also actively suppress or reject classical noise sources.

In this experiment, these challenges are addressed by combining quantum correlations with a differential sensing architecture. By interrogating two near-identical FBG sensors with the probe and conjugate beams and performing balanced intensity-difference detection, noise contributions that are common to both channels are strongly suppressed. This approach allows the underlying quantum correlations to be exploited in a noisy environment, enabling enhanced sensitivity to high-frequency mechanical

perturbations that produce differential strain responses while maintaining robustness against environmental fluctuations.

The experimental arrangement used to implement quantum-enhanced fiber sensing is shown schematically in Fig. 6.6. The twin beams, probe and conjugate, generated from the FWM process in hot ^{85}Rb vapor are first coupled into PM fibers and delivered to the sensing stage. The key idea of the experiment is to interrogate two separate fiber Bragg gratings (FBG1 and FBG2) with these quantum-correlated beams and to perform differential intensity detection to extract the signal of interest, a high frequency mechanical vibration signal, while suppressing common-mode noise.

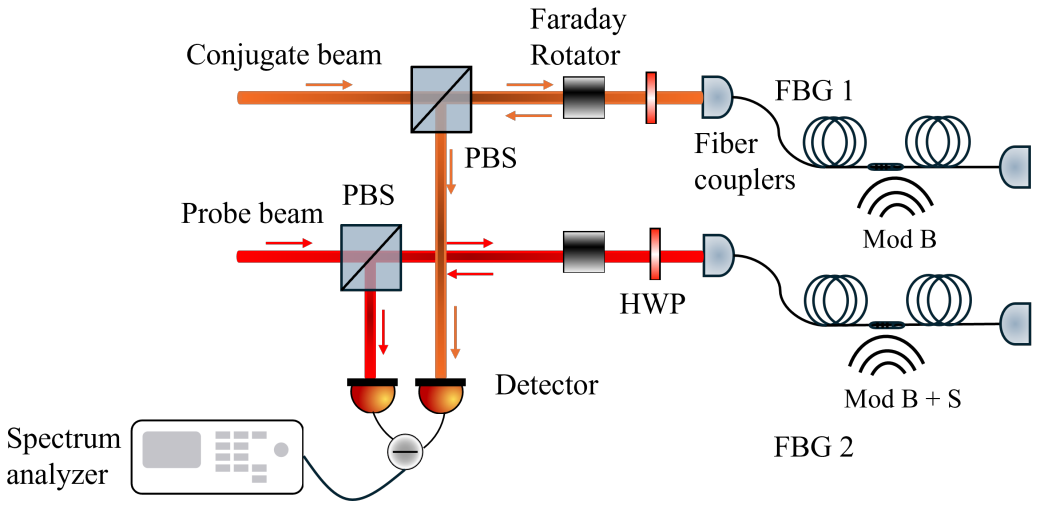


Figure 6.6: Experimental layout for quantum enhanced FBG sensing: Twin-beams are coupled to FBG1 and FBG2 in separate arms, reflected back probe and conjugate beams are collected on two photo detectors for intensity difference noise measurement. Mechanical vibration signals in the FBGs are emulated from two piezo attached mechanically to the FBGs and modulated separately with common background noise (B) and a signal (S) on one of the FBGs. All mechanical vibrations couple to the intensity modulation signal in the FBGs that is measured on spectrum analyzer.

Optical configuration

The probe and conjugate beams, matched in polarization and power, are coupled into two separate fiber channels containing FBG1 and FBG2, respectively. The Bragg wavelengths of the two gratings are tuned to be identical, ensuring that both arms respond equivalently to environmental perturbations. This symmetry is crucial for enabling common-mode noise cancellation. Each FBG reflects a majority of the incident

light near the Bragg wavelength while transmitting the rest. The reflected beams are sent to the detector, which measures the intensity difference noise trace between the two beams.

To ensure stable operation, an f-to-f optical system is used to couple the probe and conjugate beams to the fibers collimators using FC/APC connectors. Polarization control is achieved using half-wave plates placed before the fiber collimators, allowing the polarization axes of the probe and conjugate beams to be aligned with the principal axes of the PM fibers within the FBG assemblies. Faraday rotators are used to separate the back reflecting light from the incoming light. The optical powers incident on each FBG were approximately 150 μW to ensure identical detection gain.

Light reflected from the FBGs retraces the same optical path back through the fiber collimators. Upon returning, the beams experience an additional polarization rotation due to the nonreciprocal Faraday rotator and waveplate combination, causing their polarization to be orthogonal to that of the incident beams. As a result, the reflected signals are redirected by the beam splitter into separate spatial paths and sent to the photodetectors. This configuration enables efficient separation of the reflected sensing signals from the input beams while maintaining polarization stability.

Signal generation and modulation

To emulate a dynamic strain-sensing environment, the fiber Bragg gratings were mechanically coupled to a piezoelectric actuator capable of inducing controlled, time-varying strain. As shown in Fig. 6.7, the FBG fiber was rigidly clamped between two mechanical

posts, with a piezo actuator attached to one of them. Voltage signals applied to the piezo result in small periodic elongations of the fiber, thereby producing dynamic strain in the grating region.

The strain induced by the piezoelectric modulation produces a time-dependent shift in the Bragg wavelength of the FBG. When the probe and conjugate beams are biased on the slope of the FBG reflection spectrum, these wavelength shifts are transduced into intensity modulations of the reflected optical fields. By varying the modulation amplitude and frequency of the piezo signal, the dynamic optical response of the FBG could be characterized under both narrowband and broadband excitation conditions.

The piezo actuator was driven using a function generator configured to produce different excitation profiles. In particular, a broadband white-noise voltage signal spanning the frequency range from 200–300 kHz was applied to simulate a realistic noisy background environment. In addition, a single-frequency sinusoidal voltage at 250 kHz was superimposed on the broadband drive in some experiments. This combination allowed simultaneous study of both broadband background disturbances and a narrowband signal of interest, closely mimicking practical sensing scenarios where weak signals must be extracted in the presence of significant environmental noise.

This experimental approach provides a controlled platform to study the transduction characteristics of the FBG sensor and to develop signal-processing techniques for noise suppression. In particular, it enables systematic investigation of common-mode noise rejection and signal-to-noise ratio enhancement, which are essential for evaluating the advantages of differential and quantum-enhanced detection schemes discussed in later

sections.

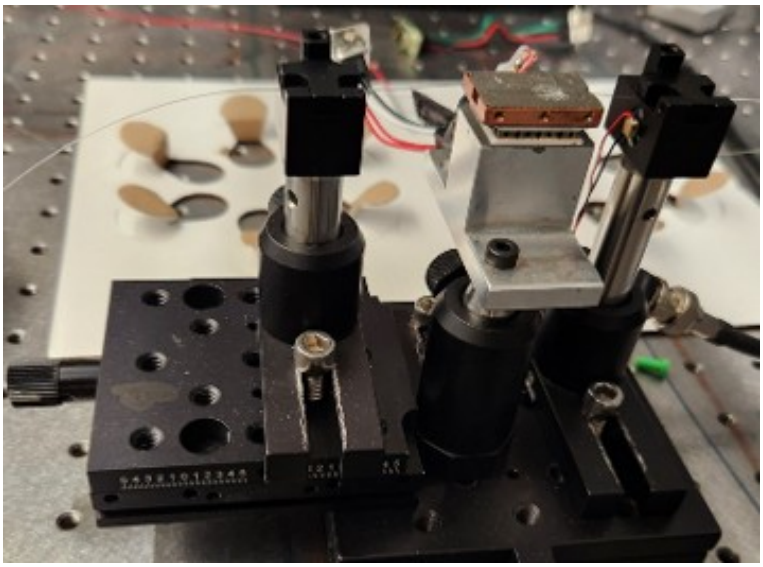


Figure 6.7: Mechanical excitation scheme for generating dynamic strain in the fiber Bragg gratings: The FBG fiber is clamped between two rigid posts, with a piezoelectric actuator attached to one post. Voltage signals applied to the piezo induce controlled vibrations and strain in the grating, producing time-dependent shifts in the Bragg wavelength that are converted into optical intensity modulations. A TEC is also put in contact with the FBG to have additional control over the response of the FBG, and therefore reflection, by varying the temperature slightly.

Detection scheme

After reflection from the FBGs, the probe and conjugate beams are directed to a pair of high-quantum-efficiency photodiodes that form a balanced detector. The photocurrents from the two detectors are subtracted, yielding the intensity-difference signal with

the modulation signal imparted by the FBGs. Because the twin beams are quantum-correlated in amplitude, common-mode noise, such as laser power noise, or environmental perturbations, cancels in the subtraction process. This enables quantum noise reduction below the SNL in the measurement.

The electronic output of the balanced detector is analyzed using a spectrum analyzer. In the absence of modulation, the measured noise power corresponds to the intensity-difference squeezing of the twin beams. When a modulation is applied to only one of the FBGs, the signal appears as a spectral peak on top of the squeezed noise floor. By comparing the noise spectra obtained with and without modulation, as well as with coherent (classical) light, we can directly quantify the signal-to-noise enhancement provided by the quantum correlations.

Calibration and reference measurements

For calibration of the shot-noise level, a coherent beam derived from the same Ti:Sapphire laser is used. The beam is split evenly between the two detectors using a 50/50 beam splitter, and the difference signal is measured to establish the shot-noise baseline. The optical powers are adjusted so that the total power incident on the photodiodes matches that of the twin-beam case, ensuring an accurate comparison. The measured squeezing is then expressed in decibels as

$$R = 10 \log_{10} \left(\frac{V_{\text{diff}}}{V_{\text{SNL}}} \right), \tag{6.3}$$

where V_{diff} is the measured variance of the intensity-difference signal with the twin beams and V_{SNL} is the corresponding shot-noise level.

This configuration provides a flexible platform for comparing classical and quantum interrogation of FBG sensors. By using twin beams to probe two nominally identical FBGs, the measurement directly exploits quantum correlations in the intensity fluctuations of the probe and conjugate fields. Because both FBGs transduce environmental perturbations in the same manner, classical noise contributions appear predominantly as common-mode fluctuations and are suppressed by balanced detection. In contrast, the quantum-correlated nature of the twin beams reduces the fundamental intensity-difference noise floor below the SNL, allowing differential strain signals to be resolved with enhanced sensitivity. This architecture therefore isolates the quantum advantage by combining common noise rejection with nonclassical noise suppression, providing a clear and experimentally robust comparison between classical and quantum interrogation of FBG sensors.

6.5 Signal Analysis and Data Processing

The data acquired from the balanced photodetectors were analyzed using a combination of spectrum-analyzer measurements and a MATLAB-based fast Fourier transform (FFT) approach. Because the experiments were conducted under two distinct operating conditions—first with squeezed light for single-frequency modulation, and later with only coherent light for broadband noise studies—the analysis is presented in two parts.

Part I describes the direct spectral measurements under single-tone excitation, where the squeezing level could be retrieved from the raw spectrum-analyzer traces. Part II describes the more detailed FFT-based analysis used for broadband, noise-intensive measurements, performed after the Ti:Sapphire laser developed stability issues that prevented locking the laser at the correct wavelength to achieve FWM and hence generate twin beams.

6.5.1 Part I: Single-Frequency Measurements with Squeezed Light

Before broadband studies were attempted, the FBG system was characterized using a single sinusoidal modulation applied to only one of the FBGs. In this configuration, the signal could be observed directly on a spectrum analyzer without the need for offline FFT processing. The FWM was optimized to produce approximately 6.5 dB of initial squeezing at the output of the vapor cell. After all optical losses, including fiber coupling, propagation losses and reflection from the two FBGs, the squeezing level at the detectors was reduced to approximately 1.2 dB.

A sinusoidal voltage at 400 kHz was applied to the piezo attached to FBG1, while FBG2 remained unmodulated. The reflected probe and conjugate beams were detected with a balanced photodetector, and the resulting photocurrent difference was analyzed on the spectrum analyzer. A clear spectral peak at 400 kHz was observed above the squeezed-noise floor. Figure 6.8 shows the shot-noise trace (blue trace), the measured squeezed-noise trace with the modulation peak (yellow trace), and the initial squeezing trace measured directly after the Rb cell (red trace).

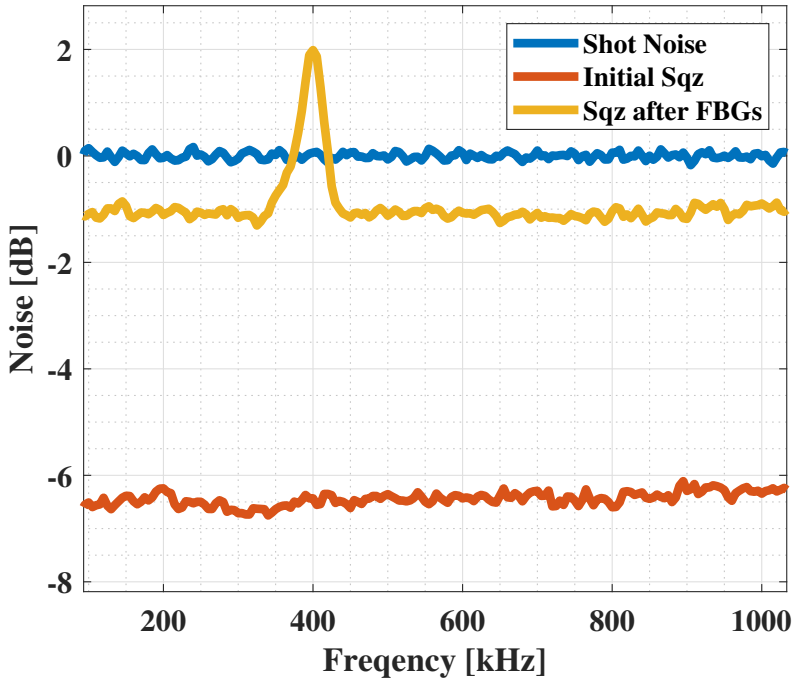


Figure 6.8: Spectral characterization of the twin-beam after interfacing with the FBG sensors with only one of them with an applied 400 kHz modulation: The blue trace is the shot-noise reference, the yellow trace shows the reduced squeezing level after fiber coupling and reflection from the FBG, and the red trace shows the initial squeezing directly after the Rb cell. The modulation peak at 400 kHz is clearly visible above the squeezed-noise floor, demonstrating successful transduction of the strain signal onto the intensity-difference measurement.

These single-frequency measurements serve two purposes. First, they confirm that the FBG response could be cleanly imprinted onto the intensity-difference measurement. Second, they provided the baseline squeezed-light performance and the amount of

squeezing remaining after all the losses are considered.

Before transitioning to broadband noise analysis, an additional set of measurements was carried out using coherent light only, as the Ti:Sapphire laser started having issues with the wavelength locking and could no longer generate squeezed light with FWM. In this test, a controlled two-tone modulation was introduced: FBG2 was driven with a 200 kHz signal to emulate a background noise component and a 400 kHz signal representing the target signal. Figure 6.9 illustrates the FBG configuration where Mod B+S (background signal at 200 kHz and target signal at 400 kHz) are applied to FBG2 and no modulation is applied to FBG1. With FBG1 left unmodulated, the spectrum exhibited two clear peaks corresponding to the modulation frequencies applied to FBG2. Figure 6.10 shows shot noise trace (blue trace) and background signal peak and target signal peak at 200 kHz and 400 kHz respectively (orange trace), when the modulation is switched on.

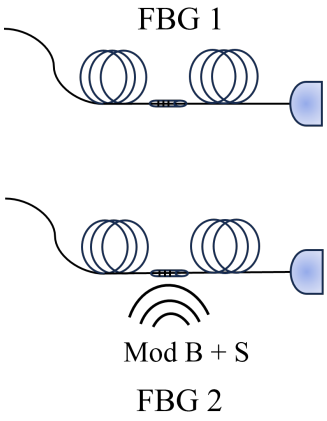


Figure 6.9: Modulaiton configuration used for two-tone coherent-light test. FBG2 is driven with a background modulation at 200 kHz (Mod B) and a signal at 400 kHz (Mod S), while FBG1 remains unmodulated. This arrangement allows the background and signal components to appear distinctly in the intensity-difference spectrum, enabling characterization of the sensor response prior to common-mode cancellation.

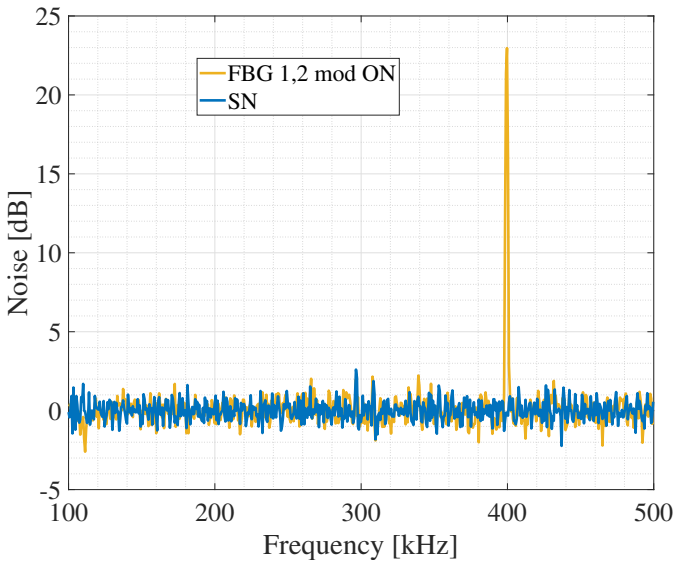


Figure 6.10: Measured spectral response for the configuration shown in Fig. 6.9. The blue trace represents the shot-noise reference, while the orange trace shows the detected spectrum when the two-tone modulation is applied to FBG2 only. Two prominent peaks appear at 200 kHz and 400 kHz, corresponding to the background component and the signal, respectively. This measurement establishes the baseline response before applying common-mode cancellation techniques.

To demonstrate common-mode cancellation, a modulation at 200 kHz was also applied to FBG1, creating a controllable replica of the background signal already present in FBG2. By independently tuning the amplitude and phase of this modulation, the 200 kHz components from both FBGs were adjusted to interfere destructively in the intensity-difference measurement. The configuration for this dual-modulation case is shown in Fig. 6.11, where both FBGs experience an identical background modulation

at 200 kHz, while only FBG2 carries the 400 kHz signal. Figure 6.12 shows the corresponding spectral measurement. When the modulation parameters were optimally matched, the 200 kHz background peak was almost completely suppressed, leaving only the isolated 400 kHz signal peak clearly visible above the noise floor. This result confirms that common-mode noise suppression can be effectively implemented in our dual-FBG scheme, enabling selective enhancement of the desired signal even under coherent-state operation.

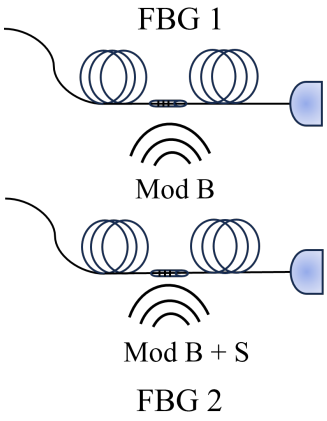


Figure 6.11: Configuration for demonstrating common-mode cancellation using a dual FBG configuration with coherent light. Both FBG1 and FBG2 are driven with an identical 200 kHz background modulation (Mod B), while FBG2 also senses the 400 kHz signal (Mod S). By adjusting the phase and amplitude of the 200 kHz drive for FBG1, the background components can be made to interfere destructively in the intensity-difference measurement.

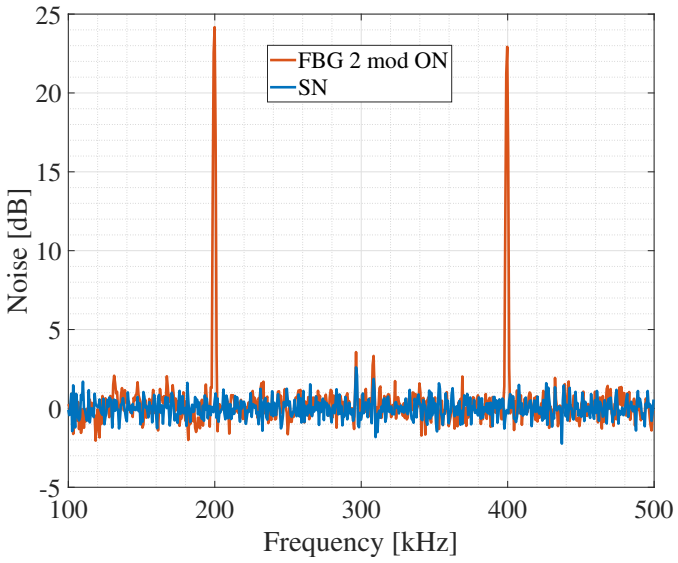


Figure 6.12: Measured spectral response for the dual-modulation configuration shown in Fig. 6.11. The blue trace is the shot-noise reference, while the yellow trace shows the detected spectrum when both FBGs are driven with a 200 kHz background modulation and FBG2 with the additional 400 kHz signal. By tuning the amplitude and phase of the background drive on FBG1, the 200 kHz background peak is completely canceled, leaving only the 400 kHz signal peak. This result demonstrates active common-mode suppression in the dual-FBG system.

6.5.2 Part II: Broadband Analysis with FFT Processing

In order to quantitatively characterize the fiber–FBG sensing scheme under realistic broadband noise conditions, we implemented a time-domain acquisition and post-processing approach based on time traces acquired with an oscilloscope and MATLAB analysis. The goal of this approach is to (i) reconstruct the system response to both

broadband and narrowband excitations, (ii) evaluate common-mode noise suppression in the dual-FBG configuration, and (iii) establish a classical sensitivity benchmark for future quantum-enhanced measurements.

Data acquisition and preprocessing

The modulation signals applied to the FBGs were generated using the RIGOL UltraStation control software, which is a computer software for an arbitrary waveform generator. It is used to program a function generator to produce time-multiplexed waveforms. The function generator outputs were routed to the two piezoelectric actuators attached to FBG1 and FBG2, with independent control over the waveforms sent to each actuator. This is done through two channels available in the function generator that can be phase referenced to each other. In parallel, a reference output was also taken from one of the channels using a splitter. And the trigger output from the function generator is used for synchronized acquisition of all channels.

Four voltage traces were recorded simultaneously on a high-speed deep-memory oscilloscope to store long time traces:

- $V_1(t)$: photodetector output for the probe beam reflected from FBG1,
- $V_2(t)$: photodetector output for the conjugate beam reflected from FBG2,
- $V_{\mathrm{ref}}(t)$: reference copy of the drive signal from the function generator,
- $V_{\mathrm{trig}}(t)$: trigger signal used to define the start of each acquisition window.

Each acquisition consists of on the order of 10^7 samples per channel, recorded at a sampling rate of 2 MS/s. This sampling rate provides sufficient resolution to resolve features in the 200–300 kHz band of interest while keeping the data volume manageable for oscilloscope memory and offline analysis.

In practical sensing environments, slow drifts and time-dependent environmental perturbations, such as temperature fluctuations and mechanical creep can continuously modify the response of the sensor and the effective balance between the two detection channels. These variations can degrade common-mode noise rejection and obscure weak signals of interest if not properly tracked. To address this challenge, the measurement protocol is designed to incorporate an effective real-time calibration strategy within each acquisition segment. By interleaving broadband excitation, combined background-plus-signal conditions, and a shot-noise reference within a single time record, the system response and noise floor can be continuously characterized and updated. This approach enables compensation for slow drifts, maintains optimal balancing between the two FBG channels, and maximizes suppression of environmental background noise, thereby allowing weak localized signals to be reliably extracted under realistic, time-varying conditions.

To systematically probe the sensor response, the function generator waveform was designed with three time "slots" within each acquisition segment. A single segment had a duration of 15 ms and was divided into three equal 5 ms slots:

1. **Slot 1 (Broadband characterization):** 200–300 kHz band-limited white noise

applied to *both* FBG1 and FBG2. This configuration characterizes the broadband transfer function and response of the dual-FBG system.

2. **Slot 2 (Broadband + signal tone):** 200–300 kHz white-noise background applied to both FBGs, *plus* an additional sinusoidal modulation at 250 kHz applied only to FBG1. This slot emulates a weak signal superimposed on a noisy background.

3. **Slot 3 (Shot-noise reference):** no drive signal applied to either FBG, with identical optical power on the detectors. This slot provides the shot-noise reference spectrum under the same optical conditions.

The third acquisition slot, which provides a shot-noise reference using coherent light, is included solely for experimental characterization and benchmarking of the system performance under controlled laboratory conditions. In a practical field-deployed sensing scenario, this reference measurement would not be required, as the system would operate continuously with the sensing configuration alone. Instead, Slot 3 serves to establish an absolute noise baseline against which the performance of the quantum-enhanced interrogation can be quantitatively evaluated.

Figure 6.13 shows oscilloscope traces acquired during the measurement. The blue and red traces, labeled V_1 and V_2, correspond to the photodetector outputs from FBG1 and FBG2, respectively. The yellow trace shows the reference signal taken directly from the function generator output driving FBG1 via a splitter, while the maroon trace corresponds to the trigger used for timing synchronization. The recorded time-

domain data are organized into consecutive acquisition segments of 15 ms duration, each of which is further subdivided into three 5 ms slots corresponding to the waveform configurations described above.

In post-processing, the start of each acquisition section is determined using the trigger channel to ensure that each 15 ms segment began at the same point in the composite waveform. The raw traces were then:

- segmented into individual segment with a duration of 15 ms,
- further split into 5 ms sub-segments corresponding to Slots 1–3.

This structured segmentation allowed separate analysis of pure broadband response, broadband-plus-signal response, and the shot-noise baseline within a single acquisition, while maintaining identical experimental conditions across all three cases.

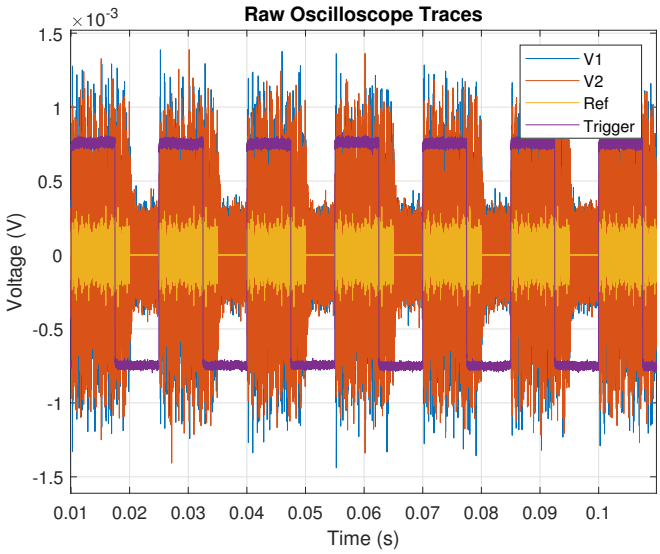


Figure 6.13: Oscilloscope traces showing multiple segments of 15 msec each. V1 and V2 are photodiode measured voltages from FBG1 and FBG2, Ref is the input signal to the FBG1 PZT from the function generator and Trigger trace is from the function generator, used to define the start of each acquisition window.

Frequency-domain analysis

Each 5 ms sub-segment was treated as a separate time window for spectral analysis. For each detector channel $i \in \{1, 2\}$ corresponding to FBG1 and FBG2 and for the reference channel (directly from the function generator output), the discrete Fourier transform was computed as

$$Y_i(f) = \frac{\mathrm{FFT}[V_i(t)]}{N}, \tag{6.4}$$

where N is the number of samples in the sub-segment and f denotes the corresponding frequency bin. The power spectral density (PSD) was then obtained according to

$$P_i(f) = |Y_i(f)|^2. \tag{6.5}$$

Then balanced detection is then implemented to suppress noise contributions that are common to both detection channels. By forming the difference spectrum, classical technical noise and environmental perturbations that couple similarly into both FBG responses are largely canceled. Balanced detection was implemented in the frequency domain by forming the complex difference spectrum

$$Y_{\text{diff}}(f) = Y_1(f) - Y_2(f), \tag{6.6}$$

with the corresponding differential PSD

$$P_{\text{diff}}(f) = |Y_{\text{diff}}(f)|^2 = |Y_1(f) - Y_2(f)|^2. \tag{6.7}$$

For each slot (broadband only, broadband + 250 kHz signal, and shot noise), the PSDs were averaged over many segments to improve the SNR of the corresponding spectra. This averaging suppresses random fluctuations and highlights reproducible spectral features such as the broadband response envelope and the narrow 250 kHz peak. One thing to note is that the approach of just getting the difference is not very accurate as each FBG has a different spectral response, which means that noise is not properly canceled.

System transfer function extraction

To accurately model how each FBG–detector arm converts mechanical strain into an optical intensity modulation, we extract a complex transfer function for each arm using only the broadband excitation present in Slot 1. For each detector channel $i \in \{1, 2\}$, the transfer function is defined as

$$H_i(f) = \frac{Y_i^{(1)}(f)}{Y_{\text{ref}}^{(1)}(f)}, \tag{6.8}$$

where $Y_i^{(1)}(f)$ and $Y_{\text{ref}}^{(1)}(f)$ denote the Fourier spectra of the detector outputs and the reference drive signal in Slot 1. Because Slot 1 contains only the shared 200–300 kHz broadband excitation, the extracted $H_i(f)$ captures the full linear response, including amplitude scaling, phase delay, and frequency-dependent sensitivity, of each FBG arm under identical, noise conditions.

The transfer functions $H_1(f)$ and $H_2(f)$ are subsequently applied to the spectra from Slots 2 and 3, enabling:

- **Common-mode cancellation in Slot 2:** revealing the isolated 250 kHz signal peak by evaluating the differential spectrum

  $$Y_{\text{diff}}^{(2)}(f) = Y_1^{(2)}(f)H_2(f) - Y_2^{(2)}(f)H_1(f),$$

  This cross-weighted subtraction compensates for residual mismatches in amplitude response and phase delay between the two FBG detector arms. By weighting each channel with the transfer function of the opposite arm, the broadband response common to both channels is equalized before subtraction, ensuring that identical environmental excitations cancel across the full frequency band.

- **Shot-noise extraction in Slot 3:** by applying the same Slot 1 transfer functions to the no-drive dataset,

$$Y_{\text{diff}}^{(3)}(f) = Y_1^{(3)}(f)H_2(f) - Y_2^{(3)}(f)H_1(f).$$

This strategy ensures a consistent and self-calibrated framework for comparing background suppression, signal isolation, and shot-noise performance. To implement this technique, the corresponding power spectral densities are obtained and averaged across all segments to obtain high-SNR. Figure. 6.14 shows comparison of post processed differential spectrum and the SN traces (shown in black and pink traces respectively) zoomed around the 200-300 kHz region. The blue and red traces shows individual cross weighted spectrum traces for FBG1 and FBG2. Ideally, with perfect cancellation, the black trace should overlap with pink trace.

We see that our differential trace shows imperfect cancellation, which is likely dominated by limitations in the transfer-function extraction and application. In particular, $H_1(f)$ and $H_2(f)$ are estimated from finite-length broadband records in individual slots and carries statistical uncertainty. Small errors in the estimated amplitude or phase response then translate into incomplete equalization prior to subtraction. In addition, the effective transfer functions can drift slowly within a measurement due to changes in the FBG bias point (temperature drift, mechanical creep), so that the response during consecutive slots would not be perfectly identical to that inferred from prior slots. We are therefore exploring improved transfer-function estimation strategies that are more robust to noise and phase errors.

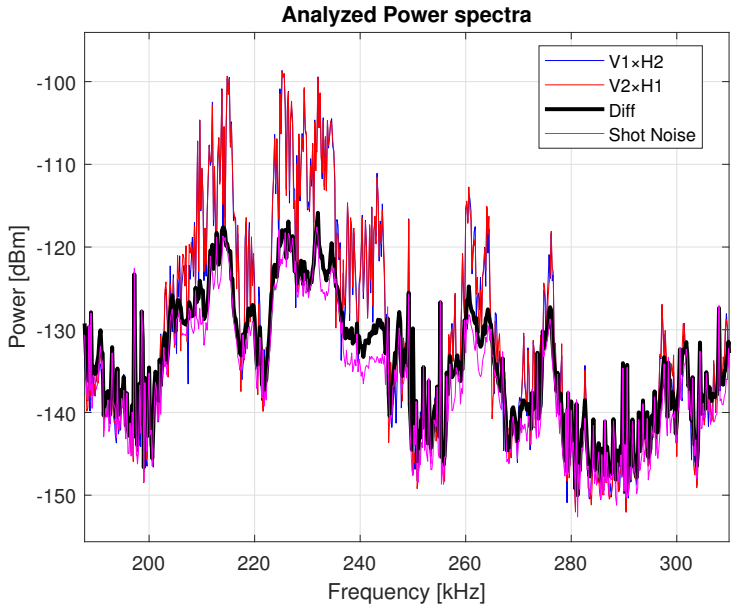


Figure 6.14: Comparison of the averaged post-processed differential spectrum and the shot-noise (SN) reference. The black trace shows the cross-weighted differential spectrum of FBG1 and FBG2, obtained by applying the transfer function of each arm to the opposite channel prior to subtraction. The pink trace shows the corresponding shot-noise spectrum extracted from the no-drive dataset using the same analysis procedure. The red and blue traces show individual cross-weighted spectrum of FBG1 and FBG2.

Common-mode noise suppression and validation

Slot 1 provides the baseline case in which both FBGs experience identical broadband excitation. After applying the transfer functions, perfect common-mode cancellation would yield

$$Y_{\text{diff}}^{(1)}(f) = Y_1^{(1)}(f)H_2(f) - Y_2^{(1)}(f)H_1(f) \approx 0, \tag{6.9}$$

this is for slot 2 without a signal, just background noise and correspondingly

$$P_{\mathrm{diff}}^{(1)}(f) = |Y_{\mathrm{diff}}^{(1)}(f)|^2 \approx P_{\mathrm{SNL}}(f). \tag{6.10}$$

Here, the approximation in Eq. (6.9) refers to the suppression of the correlated classical (common-mode) components of the signal. However, this cancellation does not eliminate the intrinsic quantum fluctuations, so the remaining noise power is set by the shot-noise level, as indicated in Eq. (6.10).

In Slot 2, an additional narrowband 250 kHz modulation is applied only to FBG1. The differential spectrum after applying the Slot 1 transfer functions is

$$Y_{\mathrm{diff}}^{(2)}(f) = Y_1^{(2)}(f)H_2(f) - Y_2^{(2)}(f)H_1(f). \tag{6.11}$$

Since the broadband background is common to both arms, it should cancel out when implementing the difference, while the 250 kHz tone, present only in FBG1, should remain. This produces a clean, isolated spectral peak at 250 kHz in $P_{\mathrm{diff}}^{(2)}(f)$ with a SN background.

This method directly demonstrates:

1. strong common-mode rejection of shared broadband noise,

2. selective preservation of differential signals,

3. the suitability of the dual-FBG architecture for detecting weak signals buried beneath large broadband disturbances.

These coherent-light results provide a classical benchmark that will later be combined with quantum noise suppression once stable squeezing operation is restored.

Broadband response and quantum enhancement

Applying the Slot 1-derived transfer functions to the no-drive dataset in Slot 3 yields the calibrated shot-noise spectrum,

$$P_{\mathrm{SNL}}(f) = |Y_1^{(3)}(f)H_2(f) - Y_2^{(3)}(f)H_1(f)|^2, \tag{6.12}$$

ensuring that the reference noise floor is measured under identical processing conditions.

In future measurements employing quantum-correlated twin beams, the degree of quantum enhancement at each analysis frequency would be quantified by comparing the signal-bearing differential spectrum to the corresponding shot-noise level,

$$\eta(f) = 10\log_{10}\left(\frac{P_{\mathrm{diff}}^{(2)}(f)}{P_{\mathrm{SNL}}(f)}\right). \tag{6.13}$$

Chapter 7

Quantum-Enhanced Plasmonic Sensing

7.1 Introduction and Motivation

In this work, we aim to not only surpass classical noise limits using quantum resources, but to do so in sensing platforms that are compatible with real-world constraints such as compactness, robustness, and integration with existing photonic technologies. While two-mode squeezed states provide a powerful quantum resource, their practical utility ultimately depends on the availability of sensing elements that can efficiently transduce external perturbations into measurable optical signals without destroying the underlying quantum correlations. In this chapter, we focus on plasmonic sensors as a promising interface between quantum light and applied sensing, motivated by their strong field confinement, large optical response to environmental changes, and compatibility with compact, chip-scale implementations. Our group has previously shown that plasmonic sensors maintain the quantum properties of twin beams used to probe them giving rise to quantum enhanced sensing [42]. These characteristics make plasmonic structures particularly attractive for translating quantum noise reduction into enhanced sensitivity for applications such as refractive-index sensing, chemical detection, and nanoscale environmental monitoring. These characteristics make plasmonic structures particularly attractive for translating quantum noise reduction into enhanced sensitivity for applications such as refractive-index sensing, chemical detection, and nanoscale environmental

monitoring. In particular, plasmonic sensors are widely used in biosensing, surface chemistry analysis, and detection of minute changes in local refractive index, making them highly relevant for real-world sensing applications.

We are interested in being able to better take advantage of our quantum resources in quantum enhanced sensing applications. To this end, we use plasmonic sensors as sensing devices to sense small changes in refractive index of the surrounding air with the help of quantum correlated twin beams.

7.2 Plasmonic Sensors and Sensitivity Calculation

Plasmonic sensors are optical read-out devices consisting of a thin metal layer sandwiched between air and a dielectric material as shown in Fig. 7.1, whose transmission changes as a result of changes in the refractive index of the air surrounding it. When probed with an electromagnetic field (EM field), their response is based on electron excitations at the metal-dielectric interface [55, 60]. The light couples to plasmonic excitations according to the phase matching condition at the interface following the boundary condition [55, 61]: $\vec{k}_{\text{light}} = \vec{k}_{\text{hole}} + \vec{k}_{\text{plasmons}}$, where $\vec{k}_{\text{light}}$ is the wave vector of light parallel to the surface, $\vec{k}_{\text{hole}}$ the wave vector of plasmon polariton along the nanoholes, and $\vec{k}_{\text{plasmons}}$ is the wave vector of the surface plasmon polariton supported at the metal–dielectric interface. Because the plasmon wave vector is larger than that of free-space light at the same frequency ($k_{\text{SPP}} > k_0$), direct coupling from free-space radiation is not possible [61]; the periodic structure supplies the required momentum to satisfy the

phase-matching condition and enable efficient excitation of plasmonic modes.

Surface plasmons are electromagnetic excitations that are tightly confined to the metal–dielectric interface, with a significant fraction of their electric field extending into the surrounding dielectric medium. Because of this strong field overlap, the properties of the plasmonic mode depend directly on the refractive index of the adjacent dielectric and therefore the surface plasmon excitation is sensitive to changes in the refractive index of the dielectric materials. Any change or modulation in the refractive index results in a shift of the characteristic transmission or reflection spectra of the plasmonic sensors [55, 62]. This property is very useful for determining changes in refractive index based on change in transmission or reflection of light through these sensors.

Typically the plasmonic sensors have a metal layer with a thickness larger than the skin depth of the metal. This makes the layer opaque for the incident EM waves. The addition of sub wavelength nanoholes in the metal layer can result in the excitation of surface plasmons. These localized excitations can couple to localized excitation on the other side of the metal layer that are then reemitted as photons. This coupling is maximum near the resonance wavelength that depends on the periodicity of nanoholes, and gradually decreases for smaller and larger wavelengths of the incident light. Under classical considerations, neither the metal film nor the sub-wavelength apertures would be expected to transmit appreciable light [63]. A metal layer with a thickness exceeding its skin depth should strongly attenuate incident electromagnetic waves, rendering the film effectively opaque. Similarly, apertures with dimensions smaller than the wavelength of the incident light should support only evanescent fields, leading to

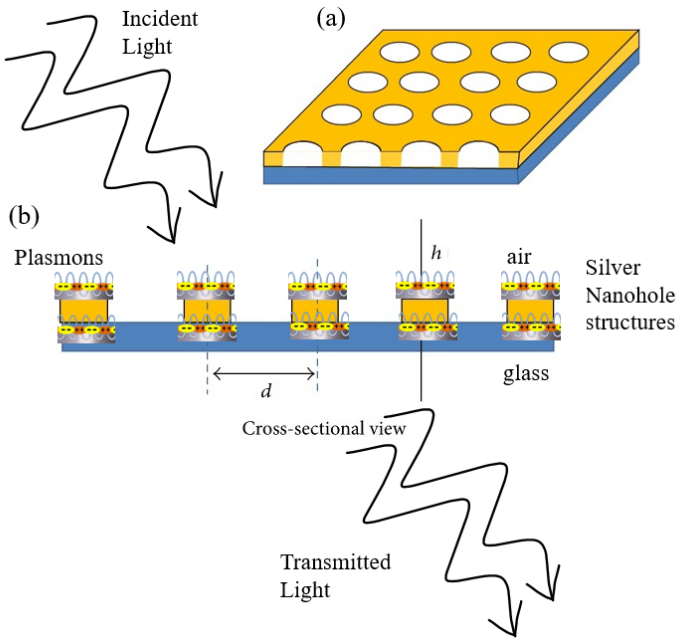


Figure 7.1: Schematic of plasmonic sensor:(a) Plasmonic sensor with circular nanohole structures in a silver metal film over a glass substrate. (b) Photon-plasmon-photon conversion process resulting in transmission for a particular resonance wavelength.

negligible transmission according to conventional diffraction theory. The observation of significant optical transmission through such a structure therefore cannot be explained by simple geometric or single-particle models [63]. Instead, the enhanced transmission arises from a coherent photon–plasmon–photon conversion process mediated by surface plasmon excitations at the metal–dielectric interfaces, giving rise to what is known as extraordinary optical transmission [63, 64].

A typical transmission spectrum showing extraordinary transmission for a plasmonic sensor is shown Fig. 7.2, with the resonance wavelength at the center. The transmission spectra of these sensors can be tuned by changing the geometry and periodicity of the

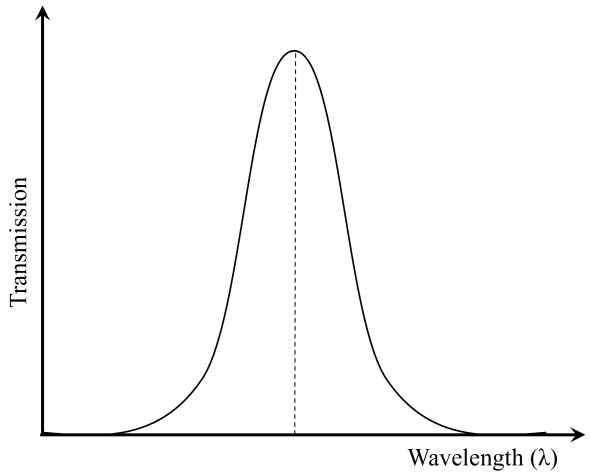


Figure 7.2: Extraordinary Transmission: Transmission spectrum of a plasmonic sensor with the resonance wavelength at the center shown with a vertical line.

nanohole structures [55, 62]. Besides these parameters, the resonance wavelength can be shifted by changing the angle of incidence and the refractive index of the dielectric materials. Therefore, for a fixed wavelength of the incident probing light, changes in refractive index (Δn) of the surrounding air can result in changes in transmission of the probing beam. Such changes in the transmission can be detected by a photodetector only if they are larger than the noise floor of the measurement.

We define the sensitivity of the sensor as the minimum resolvable change in refractive index (Δn_{min}), which is given by:

$$\Delta n_{min} = \frac{1}{\left|\partial\langle\hat{I}\rangle/\partial n\right|}\sqrt{\langle(\Delta\hat{I})^2\rangle}, \tag{7.1}$$

where $\langle\hat{I}\rangle$ is the optical intensity of the probing light, n is the index of refraction and $\langle(\Delta\hat{I})^2\rangle$ is the variance of the intensity measurement. In this expression, $\partial\langle\hat{I}\rangle/\partial n$ is a

property of plasmonic sensor that accounts for the amount of change in the intensity upon a change in refractive index.

Using plasmonic sensors as sensing devices and twin beams as quantum resources, our group has previously shown quantum enhancement in the detection of changes in the refractive index of air [42]. In particular, a plasmonic sensor was probed by one of the twin beams while the other beam was used as a reference for intensity difference noise measurements. Here, to better take advantage of resources, i.e. the total number of photons probing the sensor, we consider probing the sensor with both probe and conjugate beams as a way to further increase the sensitivity.

By designing nanohole arrays with different periodicities along orthogonal directions [65, 66], the plasmonic sensor exhibits polarization-dependent transmission responses, resulting in slightly shifted resonance features when probed with twin beams polarized along each periodicity. This is because a different lattice period shifts the phase-matching condition, which in turn shifts the plasmon resonance wavelength. In such a configuration, a change in refractive index will produce different changes in transmission for the two beams.

If the transmission responses are shifted far enough (for example Fig. 7.3) such that they have opposite slopes at the probing wavelength, while performing intensity difference noise measurements the contribution to the signal from both beams will add up. This is due to the fact that if any changes in the refractive index generates the response of transmission for the two beams that is completely out of phase. Figure. 7.4 shows such normalized transmission spectra for two orthogonal linearly polarized field,

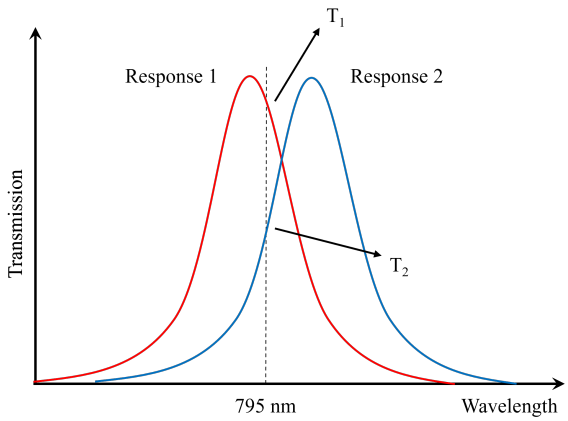


Figure 7.3: Shifted EOT spectrum for dual probing scheme: Transmission spectra of a plasmonic sensor corresponding to two orthogonally polarized probing beams.

i.e. the fraction of light transmitted through the sensor.

The vertical line in Fig. 7.4 marks the wavelength of our twin beams (795 nm). As the refractive index changes the resonance frequency of the sensor for both polarizations will shift in the same direction and would result in a change in transmission at 795 nm. If such a sensor is probed with orthogonal linearly polarized twin beams, the maximum achievable sensitivity or the minimum resolvable change in refractive index (Δn_{min}) can be estimated by applying Eq. (7.1), where $\langle \hat{I} \rangle$ is the intensity difference between transmitted probe beam and transmitted conjugate beam through the sensor, $\langle \hat{I} \rangle = \langle \hat{n}_p \rangle - \langle \hat{n}_c \rangle = T_p \langle \hat{n}_p \rangle_\circ - T_c \langle \hat{n}_c \rangle_\circ$, T_p and T_c are the transmission values at 795 nm, $\langle \hat{n}_p \rangle_\circ$ and $\langle \hat{n}_c \rangle_\circ$ are the mean values of probe and conjugate before probing the sensor and their summation ($\langle \hat{n}_p \rangle_\circ + \langle \hat{n}_c \rangle_\circ$) represents the resources in the measurement.

For the case of intensity difference measurements, the change in intensity with

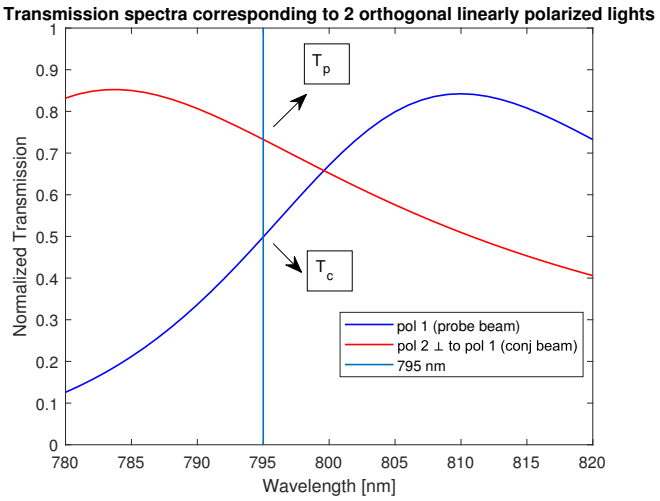


Figure 7.4: Normalized transmission spectra from plasmonic sensor for two orthogonally polarized twin beams. T_p and T_c are the transmission value at 795 nm for prob beam (red trace) and conjugate beam (blue trace), respectively.

respect to the change in index of refraction is given by

$$\frac{\partial\langle\hat{I}\rangle}{\partial n} = \frac{\partial\langle\hat{I}\rangle}{\partial\langle\hat{n}_p\rangle}\frac{\partial\langle\hat{n}_p\rangle}{\partial n} - \frac{\partial\langle\hat{I}\rangle}{\partial\langle\hat{n}_c\rangle}\frac{\partial\langle\hat{n}_c\rangle}{\partial n}, \tag{7.2}$$

For our particular configuration, the change in transmitted probe and conjugate values with respect to the change in refractive index can be written as:

$$\frac{\partial\langle\hat{n}_p\rangle}{\partial n} = -\left|\frac{\partial\langle\hat{n}_p\rangle}{\partial\lambda}\right| \times \left|\frac{\partial\lambda}{\partial n}\right|_{\lambda=795nm}, \qquad \frac{\partial\langle\hat{n}_c\rangle}{\partial n} = \left|\frac{\partial\langle\hat{n}_c\rangle}{\partial\lambda}\right| \times \left|\frac{\partial\lambda}{\partial n}\right|_{\lambda=795nm}, \tag{7.3}$$

where all the derivatives are evaluated at $\lambda = 795$ nm. The opposite signs for the two expressions takes into account that the transmission spectra in Fig. 6.1 have opposite slopes. The term $\partial\lambda/\partial n$ is a property of the sensor and can be calculated from numerical simulations by varying the refractive index of air and plotting the maxima of the transmission spectra against refractive index to obtain the rate of change.

Combining Eqs. (7.2) and (7.3), the change in intensity difference with respect to the change in index of refraction can be written as

$$\frac{\partial\langle\hat{I}\rangle}{\partial n} = \left(-\left|\frac{\partial\langle\hat{n}_p\rangle}{\partial\lambda}\right|\left|\frac{\partial\lambda}{\partial n}\right|\right) - \left(\left|\frac{\partial\langle\hat{n}_c\rangle}{\partial\lambda}\right|\left|\frac{\partial\lambda}{\partial n}\right|\right), \tag{7.4}$$

or

$$\frac{\partial\langle\hat{I}\rangle}{\partial n} = \langle\hat{n}_p\rangle_\circ\left(-\left|\frac{\partial T_p}{\partial\lambda}\right|\left|\frac{\partial\lambda}{\partial n}\right|\right) - \langle\hat{n}_c\rangle_\circ\left(\left|\frac{\partial T_c}{\partial\lambda}\right|\left|\frac{\partial\lambda}{\partial n}\right|\right), \tag{7.5}$$

and therefore

$$\left|\frac{\partial\langle\hat{I}\rangle}{\partial n}\right| = \left(\langle\hat{n}_p\rangle_\circ\left|\frac{\partial T_p}{\partial\lambda}\right| + \langle\hat{n}_c\rangle_\circ\left|\frac{\partial T_c}{\partial\lambda}\right|\right)\left|\frac{\partial\lambda}{\partial n}\right|. \tag{7.6}$$

We see that the contributions from both probe and conjugate add up. Since we want to minimize Δn_{min}, from Eq. (7.1), we want to maximize the $\frac{1}{|\partial\langle\hat{I}\rangle/\partial n|}$ and minimize $\sqrt{\langle(\Delta\hat{I})^2\rangle}$, which corresponds to the intensity difference noise between transmitted probe and conjugate beams. Since there will be a balance between enhanced signal and remaining level of squeezing, we need to consider maximizing QFI [44, 45, 47], which is discussed in the next section.

7.3 QFI for Plasmonic Sensors

When estimating a physical parameter, the achievable precision is fundamentally limited by the quantum properties of the probing state and the system under interrogation. As introduced in Chapter 2, the ultimate sensitivity is quantified by the quantum Fisher information (QFI), which sets the maximum amount of information that can be extracted about the parameter from any possible measurement [44, 45]. A larger QFI corresponds to a smaller detectable change in the parameter being estimated.

For the configuration in which one of the twin beams probes the sensor while the other beam serves as a reference, the QFI associated with estimating the transmission T of the sensor is given by [67]:

$$\mathrm{QFI}_T = \frac{1}{T - T^2[1 - \mathrm{sech}(2s)]}, \tag{7.7}$$

where T is the transmission of the sensor at 795 nm and s is the squeezing parameter of the twinbeam state. This expression quantifies the ultimate sensitivity to changes in transmission achievable with quantum-correlated twin beams, independent of the specific detection strategy.

To relate this result to refractive-index sensing, we note that the transmission through the plasmonic sensor depends on the refractive index of the surrounding medium, $T = T(n)$. For small perturbations, changes in transmission and refractive index are related by

$$\Delta T \simeq \frac{\partial T}{\partial n}\,\Delta n. \tag{7.8}$$

As a result, the variance in the refractive-index estimate can be expressed through error propagation as

$$\langle(\Delta n)^2\rangle = \langle(\Delta T)^2\rangle \left(\frac{\partial n}{\partial T}\right)^2 = \frac{\langle(\Delta T)^2\rangle}{\left(\frac{\partial T}{\partial n}\right)^2}. \tag{7.9}$$

For an optimal estimator operating at the quantum limit, the minimum variance in the estimation of T is given by the inverse of the corresponding QFI, $\langle(\Delta T)^2\rangle_{\min} = 1/\mathrm{QFI}_T$. Substituting this relation yields

$$\langle(\Delta n)^2\rangle_{\min} = \frac{1}{\mathrm{QFI}_T \left(\frac{\partial T}{\partial n}\right)^2}. \tag{7.10}$$

Equivalently, the QFI associated with estimating the refractive index n can be written as

$$\mathrm{QFI}_n = \mathrm{QFI}_T \left(\frac{\partial T}{\partial n}\right)^2 = \frac{1}{T - T^2[1 - \mathrm{sech}(2s)]} \left(\frac{\partial T}{\partial n}\right)^2. \tag{7.11}$$

This expression gives the ultimate quantum-limited sensitivity to refractive-index changes for the case in which a single beam probes the sensor and the other beam is used as a reference.

Maximizing the precision with which the refractive index can be estimated therefore requires maximizing the QFI, which is achieved through a combination of strong quantum correlations (large squeezing) and a large transmission slope with respect to refractive index. In our laboratory, we have achieved intensity-difference squeezing levels of up to 9 dB for optimized FWM parameters [42]. To exploit this quantum resource, we use COMSOL Multiphysics simulations to design nanohole-array plasmonic sensors whose transmission spectra, for two orthogonal linear polarizations, individually maximize the QFI at 795 nm for squeezing values close to 9 dB.

While the expressions above describe the case in which each beam probes the sensor independently, preliminary sensitivity analyses performed by Timmothy Woodworth indicate that even larger enhancements are possible when both probe and conjugate simultaneously interrogate the sensor. In particular, maximum sensitivity is obtained when the transmission spectra for the two polarizations have equal magnitudes but opposite slopes at the operating wavelength, enabling the signal contributions from both beams to add constructively while maintaining strong noise suppression.

The expressions above describe the case in which each beam probes the sensor

independently. As a first step toward optimizing a dual-probing sensing strategy, we therefore model different designs of our plasmonic sensors by individually maximizing the QFI for each beam when the other beam serves as a reference. This approach provides a practical and systematic method for leveraging the available quantum resources in the experiment. Under these conditions, the signal contributions from the probe and conjugate add constructively, while the quantum noise remains strongly suppressed, leading to an optimal balance between signal enhancement and noise reduction.

7.4 Modelling Nanohole Structures

We are interested in designing particular nanohole structures such that the transmission response of the plasmonic sensor is slightly shifted for two orthogonal linearly polarized fields, having opposite slopes at 795 nm. Moreover, we also want that the QFI for both the polarizations to be maximized at 795 nm.

We use COMSOL Multiphysics [68] to simulate the electromagnetic response of plasmonic nanostructures consisting of circular nanoholes patterned in a silver metal layer deposited on a glass substrate. To represent an extended nanohole array, the simulation domain is reduced to a single unit cell containing one circular aperture in the silver film, as shown in Fig. 7.5. Periodic (Floquet) boundary conditions are applied along both the x and y directions to mimic an infinite two-dimensional array in the transverse plane [64, 69]. This approach captures the collective plasmonic response of the array while significantly reducing computational cost.

We use a three-dimensional finite-element frequency-domain solver. The excitation field is defined as a normally incident plane wave impinging from the air side of the structure with a fixed linear polarization. To compute the optical response, power integration planes are placed above the metal film in air and below the structure in the glass substrate, allowing direct calculation of the total reflected and transmitted intensities through integration of the Poynting vector. The silver layer is modeled using experimentally measured complex permittivity, while the surrounding dielectric media (air and glass) are treated as homogeneous and lossless.

Along the propagation (z) direction, the simulation domain is terminated by perfectly matched layers (PMLs) placed both above the air region and below the glass substrate. These PMLs are designed to absorb outgoing electromagnetic waves over the full range of simulated wavelengths and incident polarizations, thereby preventing nonphysical reflections from the computational boundaries [70]. Between the nanohole structure and the PML regions, scattering boundary conditions are applied to ensure a smooth transition between the physical domain and the absorbing layers and to maintain numerical stability.

The excitation is introduced through a port defined in the air region above the metal film, corresponding to a normally incident plane wave propagating along the $-z$ direction. Separate simulations are performed for the two orthogonal linear polarizations, aligned along the x and y axes of the nanohole lattice, respectively. This layered boundary-condition and port-excitation configuration accurately reproduces open-space illumination and propagation through the nanostructure, ensuring that

the simulated transmission and reflection spectra faithfully capture the extraordinary optical transmission behavior of circular nanohole arrays.

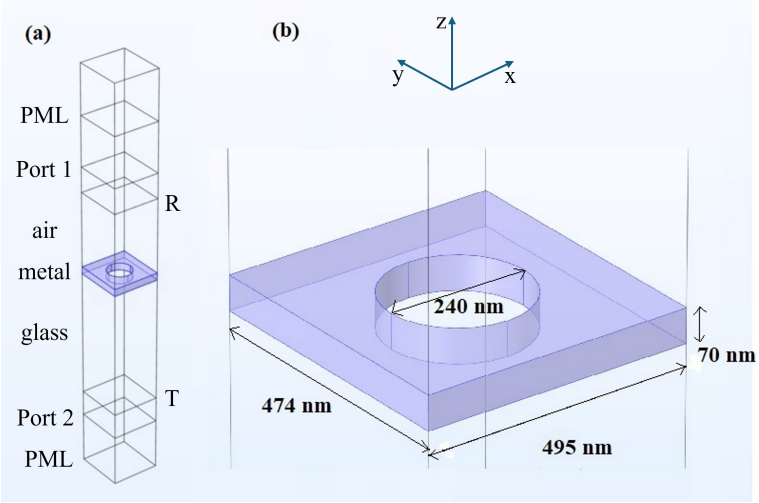


Figure 7.5: Unit cell used for COMSOL simulation of the plasmonic structure consisting of circular nanoholes in a silver metal layer over a glass substrate. (a) Silver nanohole structure with glass substrate at the bottom and air at the top. (b) Zoomed in image of unit cell made out of a silver film with a circular nanohole. The lengths along x and y axes of the unit cell defines the periodicities of the nano-hole structure in x and y directions, respectively.

To keep the transmission spectra for the two orthogonal polarizations shifted in such a way that they have opposite slopes we need different periodicities of nanoholes in x and y directions [63, 69]. After simulating multiple trials with different dimensions of nano hole structures, thickness of silver layer and periodicities of the nanoholes in x and y directions, we find the optimal geometry for the sensor such that the QFI maximized for both polarizations for about 9 dB of squeezing. We find that a 70 nm thick silver

layer on a glass substrate, consisting of circular holes with a of diameter 240 nm and a periodicity (center to center distance of the circles) of 495 nm and 474 nm in the x and y axes, respectively, gives maximum QFI at 795 nm wavelength.

Figure 7.6 and 7.7 show the normalized transmission spectra and corresponding QFI as a function of wavelength for squeezing varying from 0 dB to 10 dB. Figure 7.7(a) corresponds to the QFI for the transmission spectra for a linearly polarized probe along the larger periodicity of the nanoholes and Fig. 7.7(b) corresponds to QFI for the conjugate with an orthogonal linear polarization to that of probe. Both are maximized at 795 nm individually for 9 dB of squeezing.

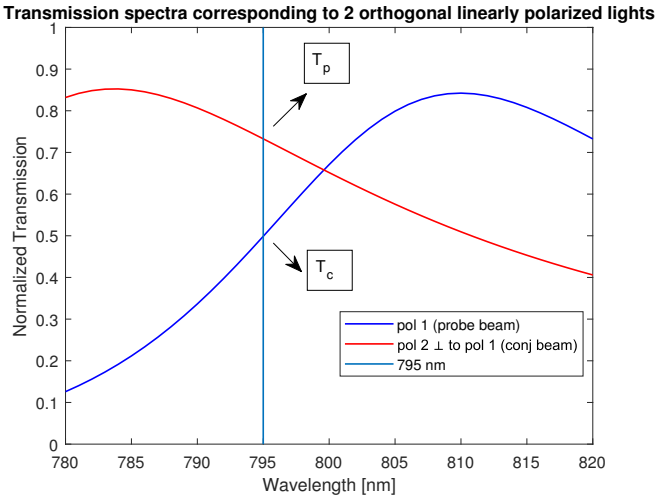


Figure 7.6: Transmission spectra simulation obtained through COMSOL for optimal parameters of the nanohole arrays. The red trace corresponds to the probe, polarized along the larger periodicity, and the blue trace corresponds to the conjugate, polarized perpendicular to the probe.

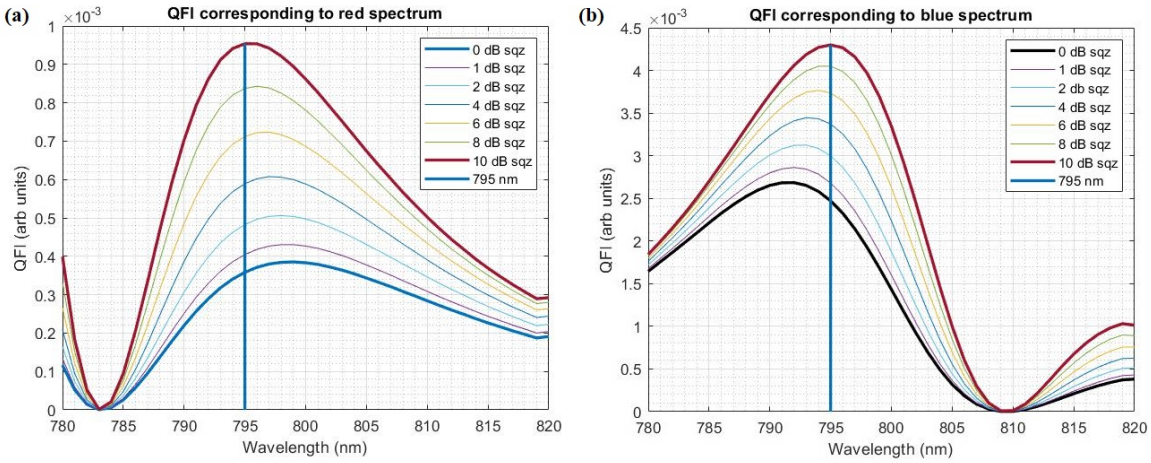


Figure 7.7: Quantum Fisher information as the level of squeezing increases from 0 to 10 dB as a function of wavelength for: (a) blue trace (conjugate) and (b) red trace (probe) in Fig. 7.6

COMSOL simulations suggests that as the angle of incidence of the light beam on the plasmonic structures increases, the transmission spectrum shifts to higher wavelengths. Therefore we modeled two other similar structures such that the QFI for both polarizations becomes maximum for a wavelength lower than 795 nm, this gives us some degree of tunability by adjusting the angle to optimize the QFI at 795 nm. We find that the optimum center to center distances of adjacent nanoholes should be (a=491 nm, b=470 nm) for a 2 degree angle of incidence and (a=484 nm, b=467 nm) for a 4 degree angle of incidence. The structure and specifications of the sensor are shown in Fig. 7.8.

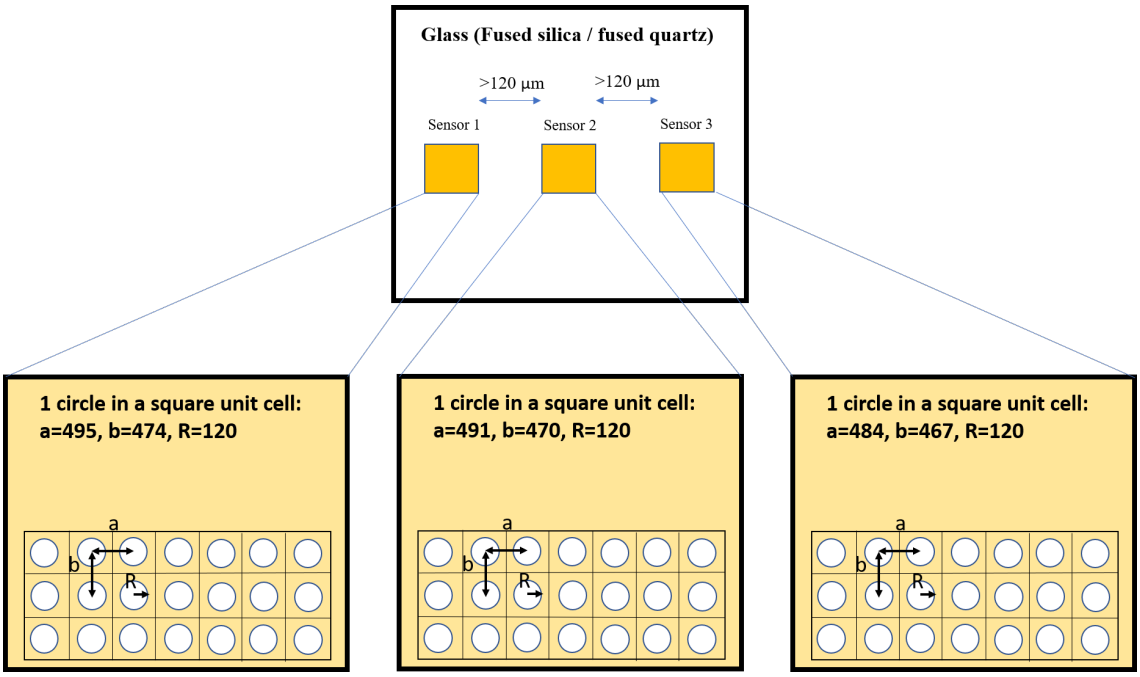


Figure 7.8: Plasmoic sensor specifications: dimensions and periodicities of the nanohole structures as optimized with COMSOL simulations to get the maximum QFI for two orthogonal linearly polarized light beams at 795 nm for a 0 degree (left sensor), 2 degree (middle sensor), and 4 degree (right sensor) angle of incidence.

7.5 Experimental Implementation

The experimental setup, to test the structures and then use them as sensors, consists of two different parts. The first one, shown in Fig. 7.9, was used for characterizing the sensor with a white light broadband source. The second setup, shown in Fig. 7.11, had been used for the experiment where refractive index modulation detection is enhanced using both probe and conjugate beams to probe the sensor simultaneously.

7.5.1 Characterization of the Sensor with Broad Band White Light

The experimental setup for characterizing the plasmonic sensors uses a broadband white light source (Halogen lamp Osram 64642-HLX-G6.35). This source can emit light in the range of 500 nm to 1100 nm. The diverging light from the lamp is coupled to a fiber to collimate and give a uniform illumination at the fiber output. Since the output of the fiber is not polarized, we use a broadband Glan-Thompson polarizer to linearly polarize the light, and a broadband half wave plate (HWP) to control and align the polarization of the incident light to the axis along a particular response of the plasmonic sensor. In general, the response of the plasmonic sensors depends on the polarization of the probing light. For this particular sensor, we are interested in the responses when the polarization is linear and aligned with either of the two symmetry axes of the nanohole structures.

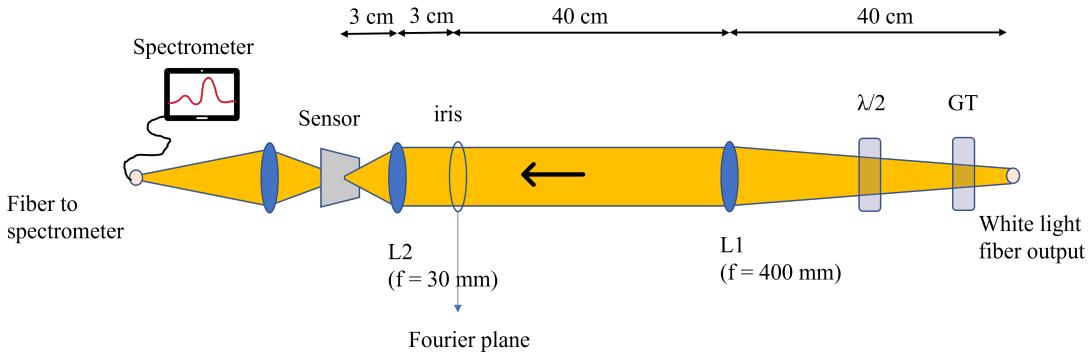


Figure 7.9: Experimental setup for transmission response measurements of a plasmonic sensor using a broadband white light source. The light first passes through a broadband Glan Thompson polarizer that is used to linearly polarize the incoming light, then a broadband half wave plate that is used to change the polarization of the light. Afterwards, a combination of achromatic lenses L1 and L2, along with an iris is used to image the source onto the sensor with a reduced beam size that can be controlled with the iris. The transmitted light from the sensor is finally collected and sent to the spectrometer with the help another achromatic lens.

As shown in Fig. 7.9, a $4f$ imaging system composed of achromatic lenses, L2 and L3, is used to adjust the size of the beam with a flat wavefront on the plamonic sensor [71]. The size of our plasmonic sensor is 120 μm $\times$ 120 μm, and the beam size at the position of the sensor is set to $\approx$ 75 μm. This size ensures that the beam is fully contained inside the sensor. An iris is placed at the Fourier plane of the illuminating light after lens L1, which serves as a filter and leads to a change in the beam size and k vector components at the position of the sensor. The transmitted light from the

sensor is then sent to a Thorlabs compact CCD spectrometer, model CCS100 (operating wavelength: 500 nm to 1100 nm).

The sensor sits on a 3D translational stage so that we can adjust its position with respect to the incident beam. First we measure the transmission from the plasmonic structure and then, using the 3D stage, slide to the glass substrate to measure the transmission. The light transmitted from the glass substrate is used as a reference to normalize the transmission from the plasmonic sensor. While measuring the transmission from the plasmonic sensor and the reference glass substrate, the position of the sample is kept fixed in the direction of light propagation, such that the beam spot size on the sensor and the glass substrate remains the same.

Figure 7.10 shows a comparison between the transmission spectra for two orthogonal linearly polarized fields from COMSOL simulations and experimental data. The dimensions (radius of circles) and periodicities (center to center distance in x and y axis) of these structures are measured from SEM images.

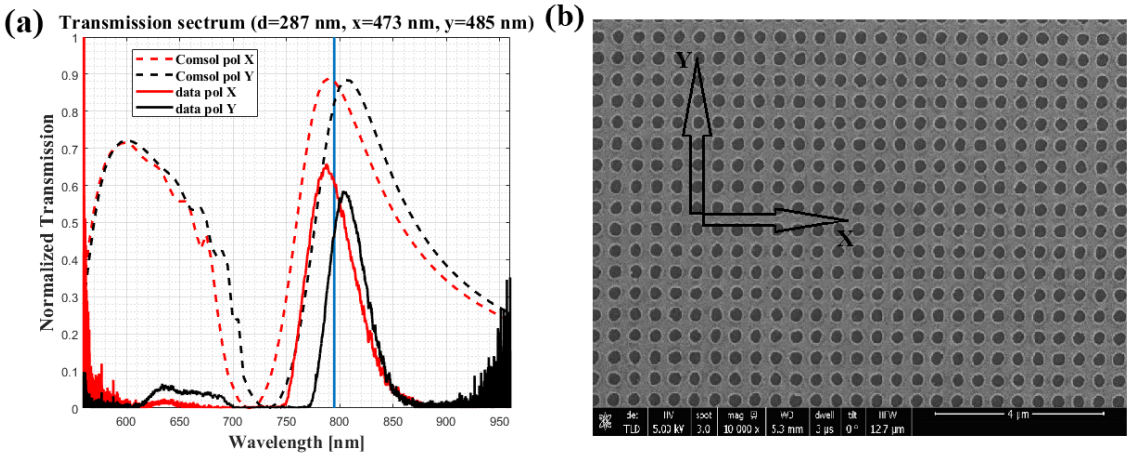


Figure 7.10: Response of fabricated plasmonic sensors:(a) Measured transmission spectra (solid curves) for fabricated arrays compared with numerical calculations (dashed curves) from COMSOL, for parameter values measured from the (b) SEM image of the corresponding sensor with nanohole diameter of: 287 nm, and periodicities of 473 nm and 485 nm along the x and y axis, respectively.

The experimental transmission response of the sensor for two orthogonal linearly polarized incident fields is similar in behaviour but with lower maximum transmission than the spectra from COMSOL simulations. This difference is likely due to imperfections in the fabrication of the nanoholes or glass refractive index mismatch between actual sensor and the COMSOL model.

7.5.2 Experimental Setup

The experimental quantum sensing setup (shown in Fig. 7.11) we use with the plasmonic sensors consists of a Ti-sapphire laser, which is used both as a source of coherent light

as well as light source for the FWM process. After the FWM process, the probe and conjugate beams are first prepared with orthogonal linear polarizations. This is achieved by rotating the polarization of the probe beam by 90° using a half-wave plate, such that it becomes orthogonal to the conjugate beam. The two beams are then spatially overlapped by injecting them into the two input ports of a polarizing beam splitter (PBS). Because of their orthogonal polarizations, both beams exit the same port of the PBS, spatially overlapped while remaining polarization-distinguishable. This combined beam is subsequently used to probe the plasmonic sensor.

After transmission through the sensor, the overlapped probe and conjugate beams are separated using a second PBS, which directs the two orthogonally polarized components into different output ports. Each beam is detected by an independent photodetector, and the resulting photocurrents are electronically subtracted using a hybrid junction. The noise power spectrum of the intensity-difference signal is then measured with a spectrum analyzer.

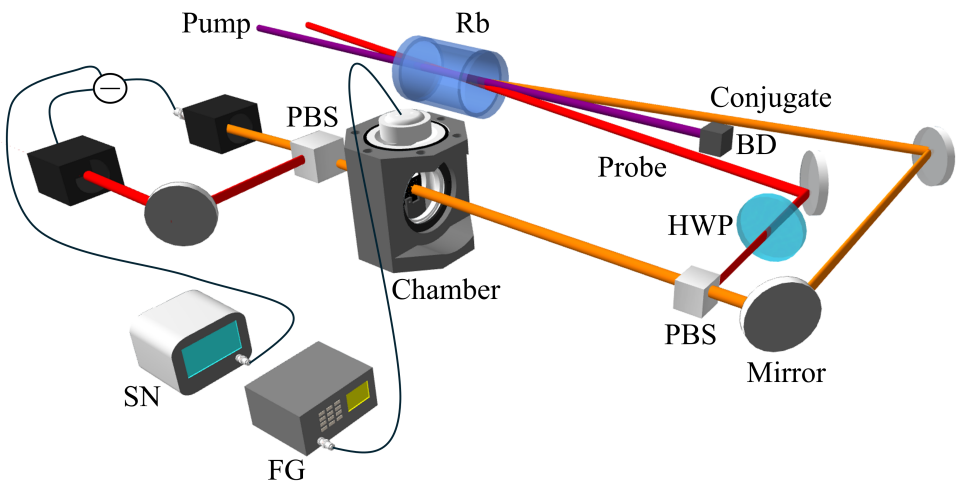


Figure 7.11: Schematic of the experimental setup. The twin beams (probe and conjugate) generated with FWM are overlapped and sent through a plasmonic sensor inside a chamber and transmitted beams are again separated for intensity difference noise measurement. The setup is used to detect small changes in the refractive index of air with a sensitivity below the shot noise limit.

To provide a direct comparison with the corresponding classical configuration, the pump beam is blocked so that no four-wave mixing occurs. In this case, only the seed beam is used to probe the plasmonic sensor, with its optical power adjusted to be equal to the combined power of the probe and conjugate beams in the quantum-enhanced measurements. A half-wave plate is used to rotate the polarization of the seed beam to 45° with respect to the sensor axes. This configuration is equivalent to probing the sensor with two classical beams of equal power and orthogonal polarizations, one aligned with each principal axis of the plasmonic structure.

After transmission through the sensor, the beam is separated into two orthogonally polarized components using a PBS, following the same detection strategy employed for the probe and conjugate beams. Each component is detected by an independent photodetector, and the resulting photocurrents are electronically subtracted. The noise power spectrum of the difference signal is then measured using a spectrum analyzer.

The modulation signal is generated by inducing controlled variations in the local refractive index of air surrounding the plasmonic sensor using pressure waves produced by an ultrasound transducer. These pressure-induced density changes lead to corresponding changes in the refractive index, which shift the plasmonic resonance condition and, consequently, modulate the optical transmission through the sensor. To ensure stable, repeatable, and well-controlled refractive-index modulations, the sensor is housed inside a custom-built airtight chamber, shown in Fig. 7.12, equipped with optical windows and a mounting interface for the ultrasound transducer. The sealed chamber suppresses the influence of ambient airflow, providing a controlled environment in which reproducible pressure waves can be generated.

When driven at a fixed frequency, the ultrasound transducer produces periodic pressure waves inside the chamber, resulting in a sinusoidal modulation of the refractive index of the air adjacent to the plasmonic structure. This modulation translates directly into a periodic shift of the plasmonic resonance, giving rise to intensity modulations in the transmitted optical signal at the same frequency. These intensity variations are subsequently detected by the photodetectors and analyzed in the frequency domain, providing a well-defined and tunable test signal for characterizing the sensor response.

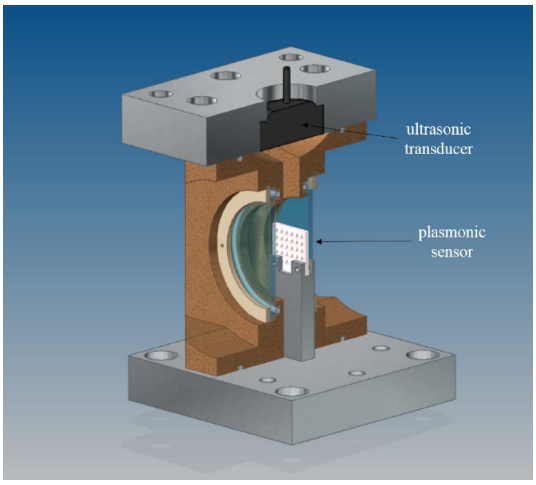


Figure 7.12: 3D rendering of a plasmonic structure inside a hermetically sealed chamber used to provide a controlled modulation of the air refractive index with an ultrasonic transducer.

With the modulation applied, the refractive-index variation produces a corresponding modulation in the sensor transmission, which appears as a well-defined signal in the detected intensity of both the probe and conjugate beams when measured individually. When the probe and conjugate simultaneously interrogate the sensor, a higher signal-to-noise ratio is expected. This improvement arises from two complementary effects. First, the residual quantum correlations between the twin beams reduce the noise floor below the shot-noise level, limited by the amount of squeezing preserved after interaction with the sensor. Second, because the transmission responses for the two orthogonal polarizations have slopes of opposite sign at the operating wavelength, the signal contributions from the probe and conjugate add constructively in the intensity-difference measurement. Together, these effects lead to an enhanced signal while

simultaneously suppressing noise, resulting in improved measurement sensitivity.

7.6 Results and Discussion

We begin by characterizing the initial level of squeezing in the twin beams in the absence of any losses, i.e., by bypassing the plasmonic sensor and directly measuring the squeezing after the Rb cell. Figure 7.13 shows noise traces, in log scale, as a function of frequency. The blue trace corresponds to the shot-noise level, while the red trace represents the measured squeezing without any additional losses. Both the traces are normalized by shot-noise, therefore the SNL trace is at zero. A maximum squeezing of approximately 6.6 dB is observed in the frequency range of 100–400 kHz.

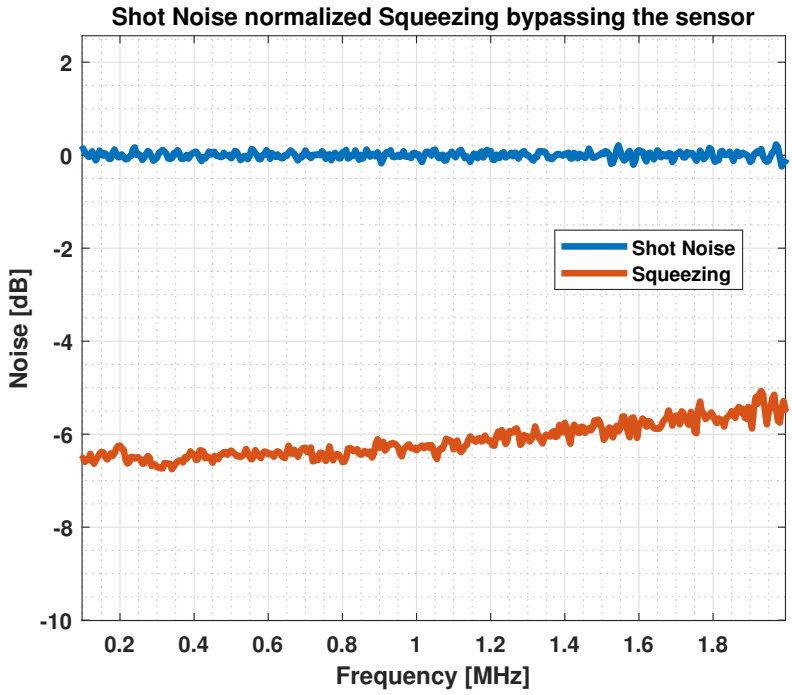


Figure 7.13: Direct squeezing measured without losses (bypassing sensor and beam splitters to overlap and separate probe and conjugate beams). The blue trace represents the shot-noise and red trace represents the squeezing. The traces are averaged 10 times with a sweep time of 3 seconds.

Since the maximum squeezing is observed at lower frequencies, and the ultrasonic transducer operates at 200 kHz, the noise traces were measured and optimized at 200 kHz in zero-span mode. Figure. 7.14 shows measured squeezing results with the plasmonic sensors. When both the probe and conjugate beams overlapped, passed through the chamber (bypassing the sensor), were separated again by a beam splitter, and detected with their respective photodiodes, the measured squeezing was 5.4 dB,

shown as the red trace in Fig. 7.14. The blue trace corresponds to the SNL, while the yellow trace shows the squeezing when both beams passed through the sensor without modulation.

In this configuration, the conjugate beam polarization was aligned along the sensor's x-axis, while the probe polarization was oriented perpendicular to it. This choice was motivated by the polarization-dependent transmission of the plasmonic sensor, for which the x-axis polarization exhibits a slightly higher transmission than the orthogonal y-axis polarization. Because the FWM process is seeded with the probe beam, the amplified probe typically has a slightly higher optical power than the conjugate prior to interacting with the sensor. Aligning the probe polarization with the lower-transmission axis and the conjugate with the higher-transmission axis therefore helps compensate for this initial power imbalance, minimizing the discrepancy between the transmitted probe and conjugate powers. The transmission losses introduced by the sensor were approximately 40% for the conjugate and 60% for the probe beam. As a result of these additional losses, the observed squeezing was reduced to 2.1 dB.

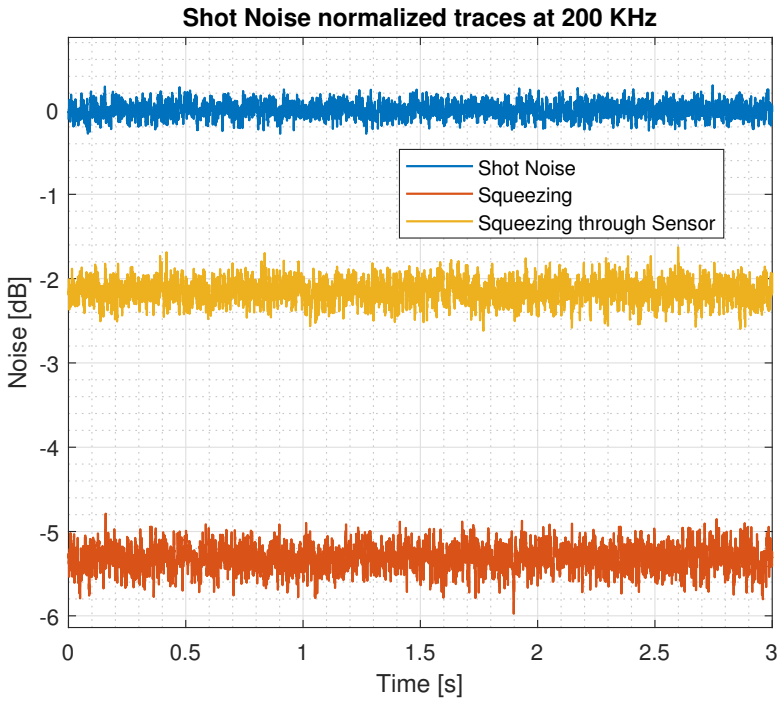


Figure 7.14: Measured squeezing with the plasmonic sensor: SNL normalized traces at 200 kHz and zero span. The blue trace represents shot noise, the red trace represents the measured squeezing when probe and conjugate go through the setup without the plasmonic structure in place and the yellow trace represents the amount of squeezing when probe and conjugate beams also pass through the plasmonic structure. The traces are for zero span and averaged 10 times over a sweep time of 3 seconds.

To demonstrate the quantum enhanced sensitivity of the system we introduce a signal through the ultrasonic transducer modulated at 200 kHz. The spectrum analyzer was set to span from 199 kHz to 201 kHz, with a 1 V amplitude drive applied to the ultrasonic transducer. The measured traces are shown in Fig. 7.15: the black trace

corresponds to the SNL, the maroon trace shows the squeezing in the twin beams bypassing the sensor, the blue trace represents the squeezing after interaction with the sensor, and the orange trace shows the response with the modulation signal applied. A distinct peak at 200 kHz is observed in the orange trace, corresponding to the refractive-index modulation induced by the ultrasonic transducer. This measurement confirms that the ultrasonic modulation produces a clearly resolvable signal at the expected frequency under the chosen spectrumanalyzer settings and drive conditions and establishes a reliable generation and detection of a well-defined refractive-index modulation.

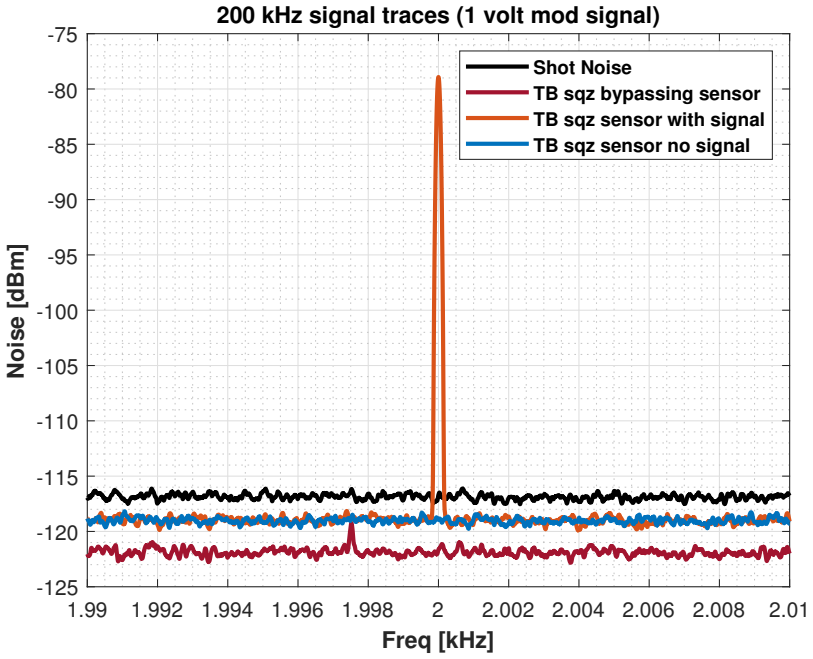


Figure 7.15: Detection of a 200 kHz modulation signal using twin-beam probing: The black trace represents the shot noise, the maroon trace represents the squeezing with both probe and conjugate bypassing only the sensor, the blue trace represents the squeezing measurement when both probe and conjugate beam pass through the sensor, and the orange trace represents the squeezing with both probe and conjugate passing through the sensor with an applied modulation at 200 kHz with 1 Volt amplitude signal input to the ultrasound transducer. All the traces corresponds to a span of frequencies from 199 kHz to 201 kHz and averaged 10 times over a sweep time of 3 seconds.

Experimentally, it is also possible to bypass one of the twin beams, either the probe or the conjugate, such that only a single beam interacts with the sensor while the other is sent directly to its detector and used as a reference. This configuration

allows the modulation signal strength to be measured for the probe and conjugate beams individually. Comparing these single-beam measurements with the case in which both beams simultaneously probe the sensor is important for isolating the advantage of the dual-probing approach. While passing both beams through the sensor introduces additional optical loss, it also allows the modulation signal to be imprinted on both beams. When combined in an intensity-difference measurement, these signal contributions add constructively, enabling more efficient use of the available quantum correlations. This comparison therefore directly illustrates the trade-off between added loss and enhanced signal transduction, and highlights the benefit of employing both beams as active sensing resources rather than using one solely as a reference.

For the configuration in which only a single beam interacts with the sensor while the other beam bypasses it, the bypassed beam would otherwise experience significantly lower optical loss. To compensate for this imbalance, an optical attenuation was introduced in the bypass arm to approximately match the transmitted power of the two beams. This step was taken to maintain comparable overall losses between the probe and conjugate channels, as large loss asymmetries can degrade intensity-difference squeezing by introducing excess noise. In principle, such balancing can also be achieved through electronic attenuation of the detector signals, which can offer improved performance; however, in the present experiment we implemented loss balancing optically using a half waveplate and a PBS to have comparable experimental conditions for both the single probing and dual probing approaches.

Figure 7.16 compiles the corresponding measurements, where the blue trace repre-

sents the SNL, and the yellow trace shows the twin-beam squeezing when neither beam interacts with the sensor. The violet, orange, and green traces correspond to when a 200 kHz modulation signal is applied to the plasmonic structure for the dual-probing configuration, probe-only probing, and conjugate-only probing, respectively.

We observe that the violet trace, corresponding to the dual-probing configuration, exhibits a stronger modulation signal than either the probe-only or conjugate-only cases. This behavior is expected as explained previously. It is also important to note that the individual probe or conjugate signals do not simply sum to reproduce the dual-probing signal amplitude. This suggests some additional contribution beyond the addition of the two individual cases. One possible explanation is a polarization-dependent effect, where the applied modulation not only imprints an intensity variation on the beams but also couples into their polarization. The polarization variations couple to intensity noise due to the PBS to separate the beams, thereby enhancing the detected signal.

An additional point to note is that the shot-noise reference measured with the modulation applied exhibits a significantly larger signal amplitude than the quantum-enhanced cases. This behavior is also likely influenced by polarization-dependent effects since the coherent reference beam is polarized at 45° with respect to the sensor axes, which is equivalent to equal projections onto the two orthogonal polarizations. So the applied modulation coupled into the polarization and enhanced the signal.

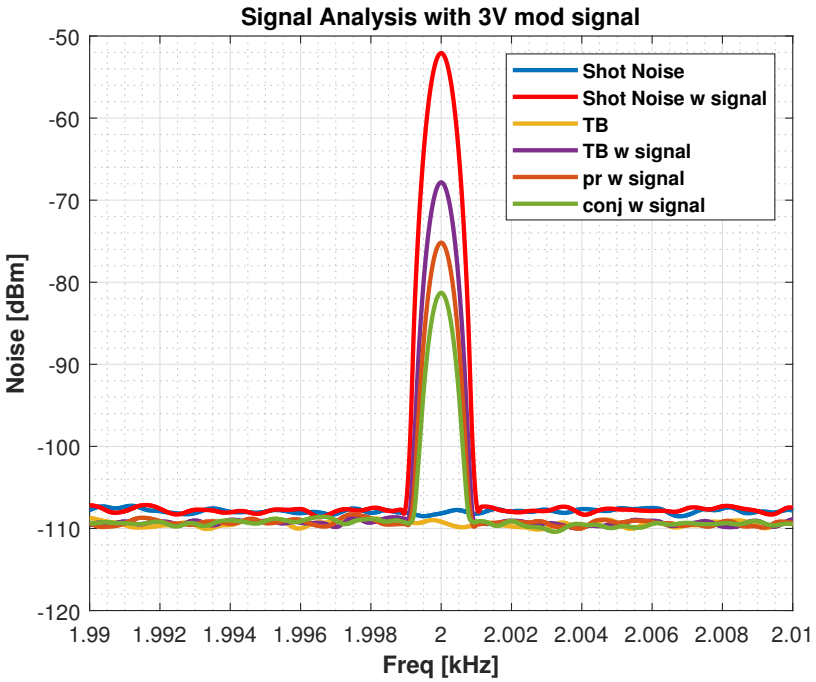


Figure 7.16: Normalized squeezing traces at 200 kHz and zero span: The blue represents the SNL, the red trace represents SNL with signal, the yellow trace represents amount of squeezing when probe and conjugate beams pass though the sensor and the purple trace represents squeezing with signal modulation. The orange (green) trace represents measured squeezing traces with probe (conjugate) pass through sensor and conjugate (probe) is used as reference. The traces are for zero span and averaged 10 times over a sweep time of 10 seconds.

These results highlight the unique advantage of the dual-probing scheme in plasmonic sensing, as it enables signal enhancement beyond what is achievable with individual probing. While some of the underlying mechanisms, such as possible polarization-dependent effects, require further investigation, the observed improvement clearly

demonstrates the potential of the dual probing approach for practical quantum-enhanced plasmonic sensors. Nevertheless, this work establishes a proof-of-principle study for combining squeezed-light resources with nanostructured materials, opening opportunities for developing highly sensitive devices for applications in chemical detection, biosensing, and other domains where plasmonic platforms already play a central role.

Chapter 8

Conclusions and Future Work

This dissertation has explored the generation and application of two-mode squeezed states of light as practical resource state for quantum-enhanced sensing. By combining theoretical foundations, experimental development of a compact squeezed-light source, and demonstrations in two distinct sensing platforms, this work advances strategies for translating quantum correlations from laboratory-scale experiments into deployable measurement tools.

8.1 Summary

The first part of this dissertation focused on the generation of twin beams via FWM in hot rubidium vapor. The underlying physical mechanisms, including the double-Λ atomic configuration, phase-matching conditions, and gain-dependent noise properties, were reviewed and experimentally characterized. Reliable calibration of the shot-noise limit and intensity-difference squeezing measurements established a robust framework for quantifying quantum noise reduction under realistic experimental conditions.

Building on this foundation, a compact, fiber-coupled twin-beam source was developed with an emphasis on low size, weight, and power (low-SWaP) operation. By optimizing beam geometry, pump power, and coupling conditions, more than 4 dB of intensity-difference squeezing was preserved after propagation through polarization-maintaining fibers. This result demonstrates that strong quantum correlations can

survive realistic optical delivery and highlights the feasibility of directly integrating squeezed-light sources into existing photonic systems.

The second part of the dissertation investigated applications of twin-beam probing for quantum-enhanced sensing. In the context of FBG sensors, twin beams were used to interrogate separate sensing elements while employing differential detection to suppress common-mode noise. This approach enabled enhanced sensitivity to localized perturbations while maintaining robustness against background fluctuations, illustrating the advantages of quantum correlations for distributed fiber-optic sensing.

A complementary application was explored using plasmonic sensors based on metallic nanostructures. A dual-probing scheme was implemented in which both beams of a two-mode squeezed state interacted with a polarization-dependent plasmonic device. By exploiting opposite spectral responses for orthogonal polarizations, this method leveraged information carried by both beams while preserving the benefits of intensity-difference detection. The results demonstrate improved sensitivity relative to single-beam probing strategies and highlight the flexibility of twinbeam techniques for nanoscale sensing platforms.

Taken together, these results show that two-mode squeezed light can be generated in compact, fiber-compatible formats and applied effectively to distinct sensing architectures. Rather than relying on a single optimized platform, this work demonstrates how quantum correlations can be adapted to diverse measurement scenarios, each with its own practical constraints and performance goals.

8.2 Broader Implications

The results presented in this dissertation contribute to the broader effort of making quantum-enhanced sensing viable outside controlled laboratory environments. The demonstration of stable squeezing in a low-SWaP, fiber-coupled configuration lowers the barrier for incorporating quantum resources into experiments where space, robustness, or accessibility are limiting factors. This is particularly relevant for sensing applications deployed in industrial, field, or distributed settings, where conventional bulk optical setups may be impractical.

More generally, the sensing demonstrations presented here illustrate how twinbeam probing can complement classical techniques by offering noise reduction, common-mode rejection, and differential measurement capabilities without requiring radical changes to existing sensor designs. By interfacing quantum light with mature photonic and plasmonic technologies, this work supports a gradual and pragmatic pathway toward quantum-enabled measurement systems.

8.3 Future Directions

Several directions for future research naturally follow from this work. On the source development side, further reductions in size and power consumption could be achieved through additional iterations employing smaller pump and probe beam sizes, which would directly reduce the required optical power while maintaining sufficient nonlinear gain. Such refinements would further advance the low-SWaP characteristics of the

source.

Further improvement of the squeezing level measured after the output optical fibers will require continued reduction of optical losses and optimization of spatial mode matching into the fibers. One significant contribution to loss in the current system arises from reflections at the uncoated fiber facets, which could be mitigated through the use of anti-reflection-coated fibers or improved fiber termination techniques. Enhancing spatial mode matching will also require optimization of the transverse modes of the generated probe and conjugate beams. This may be achieved by tailoring the spatial profile of the input seed probe or by shaping the pump beam, both of which directly influence the spatial properties of the twin beams, as demonstrated earlier in this work.

In fiber-based sensing, the twin-beam FBG scheme could be extended to larger sensor networks, enabling multiplexed or distributed measurements over long fiber links. Combining quantum noise reduction with advanced signal processing techniques may provide additional gains in sensitivity and robustness, particularly in noisy or dynamic environments. For plasmonic sensing, future work could explore alternative nanostructure designs, materials, and geometries optimized specifically for quantum-enhanced probing. Integrating squeezed-light techniques with on-chip plasmonic platforms may open opportunities for compact and highly sensitive sensors capable of operating at the nanoscale.

More broadly, the concepts demonstrated in this dissertation may be applied to other sensing modalities, including interferometric, spectroscopic, and hybrid photonic systems. As quantum light sources continue to mature, the ability to tailor quantum

correlations to specific measurement tasks will play an increasingly important role in the development of practical quantum technologies.

In conclusion, this dissertation demonstrates that two-mode squeezed light can serve as a versatile and practical resource for quantum-enhanced sensing. By bridging source development and application-driven experiments, it contributes to the ongoing effort to transform quantum correlations from laboratory curiosities into useful tools for real-world metrology.

References

[1] T. H. Maiman, "Stimulated optical radiation in ruby," *Nature*, vol. 187, pp. 493–494, 1960.

[2] J. L. Hall, "Nobel lecture: Defining and measuring optical frequencies," *Rev. Mod. Phys.*, vol. 78, pp. 1279–1295, 2006.

[3] R. J. Glauber, "The quantum theory of optical coherence," *Phys. Rev.*, vol. 130, pp. 2529–2539, 1963.

[4] D. F. Walls and G. J. Milburn, *Quantum Optics*. Springer, 1994.

[5] C. M. Caves, "Quantum-mechanical noise in an interferometer," *Phys. Rev. D*, vol. 23, pp. 1693–1708, 1981.

[6] R. E. Slusher, L. W. Hollberg, B. Yurke, J. C. Mertz, and J. F. Valley, "Observation of squeezed states generated by four-wave mixing in an optical cavity," *Phys. Rev. Lett.*, vol. 55, pp. 2409–2412, 1985.

[7] J. P. Dowling and G. J. Milburn, "Quantum technology: the second quantum revolution," *Phil. Trans. R. Soc. A*, vol. 361, pp. 1655–1674, 2003.

[8] M. A. Nielsen and I. L. Chuang, *Quantum Computation and Quantum Information*. Cambridge University Press, 2000.

[9] V. Giovannetti, S. Lloyd, and L. Maccone, "Quantum-enhanced measurements: Beating the standard quantum limit," *Science*, vol. 306, pp. 1330–1336, 2004.

[10] V. Giovannetti, S. Lloyd, and L. Maccone, "Advances in quantum metrology," *Nat. Photonics*, vol. 5, pp. 222–229, 2011.

[11] M. A. Taylor and W. P. Bowen, "Quantum metrology and its application in biology," *Phys. Rep.*, vol. 615, pp. 1–59, 2016.

[12] L. Pezzè, A. Smerzi, M. K. Oberthaler, R. Schmied, and P. Treutlein, "Quantum metrology with nonclassical states of atomic ensembles," *Rev. Mod. Phys.*, vol. 90, p. 035005, 2018.

[13] M. Planck, "On the law of distribution of energy in the normal spectrum," *Annalen der Physik*, vol. 4, pp. 553–563, 1901.

[14] A. Einstein, "On a heuristic point of view concerning the production and transformation of light," *Annalen der Physik*, vol. 17, pp. 132–148, 1905.

[15] N. Bohr, "On the constitution of atoms and molecules," *Philosophical Magazine*, vol. 26, pp. 1–25, 1913.

[16] W. Shockley, *Electrons and Holes in Semiconductors: With Applications to Transistor Electronics*. New York, NY, USA: D. Van Nostrand Company, 1950.

[17] P. C. Lauterbur, "Image formation by induced local interactions: Examples employing nuclear magnetic resonance," *Nature*, vol. 242, pp. 190–191, 1973.

[18] W. Heisenberg, "über den anschaulichen inhalt der quantentheoretischen kinematik und mechanik," *Zeitschrift für Physik*, vol. 43, pp. 172–198, 1927.

[19] D. F. Walls, "Squeezed states of light," *Nature*, vol. 306, pp. 141–146, 1983.

[20] H. J. Kimble and L. Mandel, "Photon antibunching in resonance fluorescence," *Phys. Rev. Lett.*, vol. 39, pp. 691–695, 1977.

[21] D. J. Wineland, J. J. Bollinger, W. M. Itano, and D. J. Heinzen, "Spin squeezing and reduced quantum noise in spectroscopy," *Phys. Rev. A*, vol. 46, pp. R6797–R6800, 1992.

[22] The LIGO Scientific Collaboration, J. Aasi, J. Abadie, B. P. Abbott, and R. Abbott, "Enhanced sensitivity of the ligo gravitational wave detector by using squeezed states of light," *Nature Photonics*, vol. 7, pp. 613–619, 2013.

[23] M. Tse *et al.*, "Quantum-enhanced advanced ligo detectors in the era of gravitational-wave astronomy," *Physical Review Letters*, vol. 123, p. 231107, 2019.

[24] M. Kasevich and S. Chu, "Atomic interferometry using stimulated raman transitions," *Phys. Rev. Lett.*, vol. 67, pp. 181–184, 1991.

[25] K. B. et al., "Taking atom interferometric quantum sensors from the laboratory to real-world applications," *Nat. Rev. Phys.*, vol. 1, pp. 731–739, 2019.

[26] N. Treps, U. Andersen, B. Buchler, P. K. Lam, A. Maître, H.-A. Bachor, and C. Fabre, "Surpassing the standard quantum limit for optical imaging using nonclassical multimode light," *Science*, vol. 301, pp. 940–943, 2003.

[27] S. L. Braunstein and P. van Loock, "Quantum information with continuous variables," *Rev. Mod. Phys.*, vol. 77, pp. 513–577, 2005.

[28] L.-M. Duan, G. Giedke, J. I. Cirac, and P. Zoller, "Inseparability criterion for continuous variable systems," *Phys. Rev. Lett.*, vol. 84, pp. 2722–2725, 2000.

[29] R. Loudon and P. L. Knight, "Squeezed light," *Journal of Modern Optics*, vol. 34, pp. 709–759, 1987.

[30] D. Stoler, "Equivalence classes of minimum uncertainty packets," *Phys. Rev. D*, vol. 1, pp. 3217–3219, 1970.

[31] R. W. Boyd, *Nonlinear Optics*. Academic Press, 3rd ed., 2008.

[32] D. C. Burnham and D. L. Weinberg, "Observation of simultaneity in parametric production of optical photon pairs," *Phys. Rev. Lett.*, vol. 25, pp. 84–87, 1970.

[33] Z. Y. Ou, S. F. Pereira, H. J. Kimble, and K. C. Peng, "Realization of the einstein-podolsky-rosen paradox for continuous variables," *Phys. Rev. Lett.*, vol. 68, pp. 3663–3666, 1992.

[34] C. F. McCormick, V. Boyer, E. Arimondo, and P. D. Lett, "Strong relative intensity squeezing by four-wave mixing in rubidium vapor," *Optics Letters*, vol. 32, pp. 178–180, 2007.

[35] V. Boyer, A. M. Marino, R. C. Pooser, and P. D. Lett, "Entangled images from four-wave mixing," *Science*, vol. 321, pp. 544–547, 2008.

[36] A. I. Lvovsky and M. G. Raymer, "Continuous-variable optical quantum-state tomography," *Rev. Mod. Phys.*, vol. 81, pp. 299–332, 2009.

[37] A. M. Marino, R. C. Pooser, V. Boyer, and P. D. Lett, "Tunable delay of einstein-podolsky-rosen entanglement," *Nature*, vol. 457, pp. 859–862, 2009.

[38] M. T. Turnbull, J. A. Morizur, M. Lassen, and N. Treps, "Optimisation of four-wave mixing in hot atomic vapours," *Journal of Optics*, vol. 15, p. 075201, 2013.

[39] H.-A. Bachor and T. C. Ralph, *A Guide to Experiments in Quantum Optics*. Wiley-VCH, 2004.

[40] M. I. Kolobov, *Quantum Imaging*. Springer, 1999.

[41] R. C. Pooser and B. J. Lawrie, "Ultrasensitive measurement of microcantilever displacement below the shot-noise limit," *Optica*, vol. 2, pp. 393–399, 2015.

[42] M. Dowran, A. Kumar, B. J. Lawrie, R. C. Pooser, and A. M. Marino, "Quantum-enhanced plasmonic sensing," *Optica*, vol. 5, no. 5, pp. 628–633, 2018.

[43] B. J. Lawrie, R. C. Pooser, and S. M. Marino, "Nonclassical light for enhanced measurement sensitivity," *ACS Photonics*, vol. 6, pp. 1307–1318, 2019.

[44] C. W. Helstrom, *Quantum Detection and Estimation Theory*. Academic Press, 1976.

[45] S. L. Braunstein and C. M. Caves, "Statistical distance and the geometry of quantum states," *Phys. Rev. Lett.*, vol. 72, pp. 3439–3443, 1994.

[46] A. Monras, "Phase space formalism for quantum estimation of gaussian states," *arXiv preprint arXiv:1303.3682*, 2013.

[47] D. Šafránek, "Quantum fisher information for gaussian states," *Phys. Rev. A*, vol. 95, p. 052320, 2017.

[48] U. Jain, J. Choi, C. Hull, and A. M. Marino, "Compact fiber-coupled narrowband two-mode squeezed light source," *Optics Letters*, vol. 50, pp. 5165–5168, 2025.

[49] N. V. Corzo, A. M. Marino, and P. D. Lett, "Multi-spatial-mode single-beam squeezing in four-wave mixing," *Phys. Rev. Lett.*, vol. 107, p. 183601, 2011.

[50] M. W. Holtfrerich, N. V. Corzo, A. M. Marino, and P. D. Lett, "Controlled transverse mode interactions in four-wave mixing," *Optics Letters*, vol. 41, pp. 5111–5114, 2016.

[51] P. Gupta and R. W. Speirs, "Effect of mode mismatch on squeezing measurements with multimode fields," *Optics Express*, vol. 28, pp. 194–206, 2020.

[52] K. O. Hill and G. Meltz, "Fiber bragg grating technology fundamentals and overview," *Journal of Lightwave Technology*, vol. 15, pp. 1263–1276, 1997.

[53] R. Kashyap, *Fiber Bragg Gratings*. Academic Press, 1999.

[54] A. Othonos, "Fiber bragg gratings," *Review of Scientific Instruments*, vol. 68, pp. 4309–4341, 1999.

[55] J. Homola, "Surface plasmon resonance sensors for detection of chemical and biological species," *Chemical Reviews*, vol. 108, pp. 462–493, 2008.

[56] A. D. Kersey, M. A. Davis, H. J. Patrick, M. LeBlanc, K. P. Koo, C. G. Askins, M. A. Putnam, and E. J. Friebele, "Fiber grating sensors," *Journal of Lightwave Technology*, vol. 15, pp. 1442–1463, 1997.

[57] X. Bao and L. Chen, "Recent progress in distributed fiber optic sensors," *Sensors*, vol. 12, pp. 8601–8639, 2012.

[58] Z. Yao, M. Li, G. Li, M. Xing, and N. Chen, "A high-sensitivity fiber bragg grating sensor for displacement measurement in structural health monitoring," *Review of Scientific Instruments*, vol. 94, no. 9, p. 095008, 2023.

[59] H. Li, Z. Sun, and Y. Li, "Fiber-optic sensors: A review," *Sensors*, vol. 16, pp. 1–24, 2016.

[60] K. A. Willets and R. P. V. Duyne, "Localized surface plasmon resonance spectroscopy and sensing," *Annual Review of Physical Chemistry*, vol. 58, pp. 267–297, 2007.

[61] H. Raether, *Surface Plasmons on Smooth and Rough Surfaces and on Gratings*. Springer, 1988.

[62] A. G. Brolo, "Plasmonics for future biosensors," *Nature Photonics*, vol. 6, pp. 709–713, 2012.

[63] T. W. Ebbesen, H. J. Lezec, H. F. Ghaemi, T. Thio, and P. A. Wolff, "Extraordinary optical transmission through sub-wavelength hole arrays," *Nature*, vol. 391, pp. 667–669, 1998.

[64] L. Martín-Moreno, F. J. García-Vidal, H. J. Lezec, K. M. Pellerin, T. Thio, J. B. Pendry, and T. W. Ebbesen, "Theory of extraordinary optical transmission through subwavelength hole arrays," *Physical Review Letters*, vol. 86, pp. 1114–1117, 2001.

[65] R. Gordon, A. G. Brolo, A. McKinnon, A. Rajora, B. Leathem, and K. L. Kavanagh, "Strong polarization in the optical transmission through elliptical nanohole arrays," *Physical Review Letters*, vol. 92, p. 037401, 2004.

[66] B. Auguié and W. L. Barnes, "Collective resonances in gold nanoparticle arrays," *Physical Review Letters*, vol. 101, p. 143902, 2008.

[67] T. Woodworth, M. Dowran, and S. M. Marino, "Quantum limits to optical transmission measurements with correlated photons," *Physical Review A*, vol. 102, p. 033704, 2020.

[68] COMSOL AB, Stockholm, Sweden, *COMSOL Multiphysics, Version 6.1*, 2023. RF Module and Wave Optics Module.

[69] C. Genet and T. W. Ebbesen, "Light in tiny holes," *Nature*, vol. 445, pp. 39–46, 2007.

[70] J.-P. Berenger, "A perfectly matched layer for the absorption of electromagnetic waves," *Journal of Computational Physics*, vol. 114, pp. 185–200, 1994.

[71] J. W. Goodman, *Introduction to Fourier Optics*. Roberts and Company, 3 ed., 2005.